ROBUST FEEDBACK CONTROL OF FLOW INDUCED STRUCTURAL RADIATION OF SOUND

ROBUST FEEDBACK CONTROL OF FLOW INDUCED
STRUCTURAL RADIATION OF SOUND

Sponsored by a
NASA Fellowship

HL 97-7 Report #0278-1

Submitted by: Craig M. Heatwole, Graduate Research Assistant
Robert J. Bernhard, Co-Principal Investigator
Matthew A. Franchek, Co-Principal Investigator

Approved by: Robert J. Bernhard, Director
Ray W. Herrick Laboratories

February 1997

TABLE OF CONTENTS

Page

LIST OF TABLES

LIST OF FIGURES

Figure Page

Figure Page

Figure Page

NOMENCLATURE

$\{\}$	Denotes a vector
$[]$	Denotes a matrix
$\|\|$	Denotes the Magnitude
$\|\|\|\|_\infty$	H_∞ Norm
$[]^{-1}$	Inverse Operator
$[]^*$	Complex Conjugate
$[]^H$	Hermitian Transpose
$[]^T$	Transpose
A	Longitudinal Decay Function in S_{ff}
a	Longitudinal Extent of the Plate
B	Lateral Decay Function in S_{ff}
b	Lateral Extent of the Plate
c	Viscous Damping Coefficient
D	Weighting Matrix for μ Synthesis
D_o	Flexural Rigidity
f	Excitation Pressure
F_q	Qth Actuator Modal Participation Coefficient
$\mathcal{F}_l$	Linear Fractional Transform
G_C	Controller Transfer Function
G_D	Transfer Function for the Turbulent Boundary Layer Excitation
G_R	Transfer Function for the Sound Pressure Level
G_U	Transfer Function for the Plate Dynamics
$\hat{G}_U$	Estimate of the Plant Transfer Function

k	Acoustic Wavenumber
K	Controller for μ Synthesis
H	Equivalent Feedforward Controller
H_q	Qth Sensor Modal Participation Coefficients
$\hat{L}$	Stability Transfer Function for an Adaptive Feedback Controller
L_k	Kth Open Loop Transfer Function
m	Mass Per Unit Area
N_x	In-plane force in the x direction
N_y	In-plane force in the y direction
N_{xy}	In-plane shear force
O	Function to be Minimized in Actuator and Sensor Optimization
P_{des}	Desired Sound Pressure Level
p	Sound Pressure
$\mathcal{P}_k$	kth Loop Uncertainty Correction Factor
q_r	Generalized Rth Modal Force
Q_r	Fourier Transform of the rth Modal Generalized Force
Q	Linear Fractional Transform of the Controller and Plant
R	Position Vector of the Point to be Controlled
Re_a	Reynolds Number
r	Rth mode Corresponding to p q Indices
r_s	Position Vector to the Surface Element
S_{ff}	Cross-Spectral Density of the Wall Pressure
S_{pp}	Power Spectral Density of the Wall Pressure
S_{qq_r}	Power Spectral Density of the Generalized Force for the rth Mode
$S_{qq_{rs}}$	Cross-Spectral Density of the Generalized Force
S_{uu}	Power Spectral Density of the Plate Displacement
T_c	Closed Loop Transfer Function of The Control Effort
T_r	Closed Loop Transfer Function for the Rth Modal Acceleration
U_c	Convective Velocity

U_∞	Free Stream Velocity
u	Normal Plate Displacement
$\dot{u}$	Normal Plate Velocity
$\bar{x}$	Plate Coordinate (x, y)
∇^2	Laplacian Operator
α	Unknown System Parameters
α_o	Nominal System Parameters
δ^*	Boundary Layer Displacement Thickness
Δ	System Perturbation Matrix
η	Lateral Separation of Flow Field Points
η_r	Rth Modal Displacement
$\dot{\eta}_r$	Rth Modal Velocity
$\ddot{\eta}_r$	Rth Modal Acceleration
γ_1	Decay in the Longitudinal Direction
γ_3	Decay in the Lateral Direction
λ	Constant Associated with Fluid Type in S_{pp}
κ	Maximum Control Effort
ω_r	Natural Frequency of the Rth mode
ϕ	Angle in the Spherical Coordinate System
Ψ_r	Eigenfunction of the Rth Mode
ρ_o	Density of the Fluid
θ	Angle in the Spherical Coordinate System
ξ	Longitudinal Separation of Flow Field Points
ξ_r	H_∞ Weighting for Modal Accelerations
ξ_c	H_∞ Weighting for Control Effort
ζ	Damping Ratio of the Plate

ABSTRACT

Heatwole, Craig M. PhD., Purdue University, May 1997. Robust Feedback Control of Flow Induced Structural Radiation of Sound. Major Professors: Dr. Robert J.Bernhard and Dr. Matthew A. Franchek, School of Mechanical Engineering.

A significant component of the interior noise of aircraft and automobiles is a result of turbulent boundary layer excitation of the vehicular structure. In this work, active robust feedback control of the noise due to this non-predictable excitation is investigated.

Both an analytical model and experimental investigations are used to determine the characteristics of the flow induced structural sound radiation problem. The problem is shown to be broadband in nature with large system uncertainties associated with the various operating conditions. Furthermore the delay associated with sound propagation is shown to restrict the use of microphone feedback. The state of the art control methodologies, μ synthesis and adaptive feedback control, are evaluated and shown to have limited success for solving this problem.

A robust frequency domain controller design methodology is developed for the problem of sound radiated from turbulent flow driven plates. The control design methodology uses frequency domain sequential loop shaping techniques. System uncertainty, sound pressure level reduction performance, and actuator constraints are included in the design process. Using this design method, phase lag was added using non-minimum phase zeros such that the beneficial plant dynamics could be used. This general control approach has application to lightly damped vibration and sound radiation problems where there are high bandwidth control objectives requiring a low controller DC gain and controller order.

The controller design methodology developed in this work was verified experimentally. A multiple-input-multiple-output controller using accelerometer feedback and shaker control was able to achieve robust control up to 1000 Hz. Sound pressure level reductions of as much as 15 dB were achieved at multiple microphone locations. Overall reductions over the 100-1000 Hz band were approximately 5 dB. The controller was found to be robust to large changes in the system parameters due to speed variations from 35.8 m/s to 51.5 m/s and changes in the plate mass up to 40 percent.

CHAPTER 1. INTRODUCTION

The structural radiation of sound resulting from a turbulent boundary layer is a major consideration in a variety of engineering applications. This phenomenon has been investigated by sonar, aircraft, and automobile designers. The turbulent flow pressure fluctuations from the propulsion of ships drive the sonar dome and induce structural radiation of sound which interferes with the sonar receiver. As a result, the background noise is increased which limits sonar performance. Sound radiated into an aircraft interior is a result of skin panel vibration which is excited by such sources as the unsteady boundary layer flow over the fuselage, jet and propeller noise, compressor whine, and thrust reversal noise. These skin vibrations act as a transducer to radiate sound into the interior. With the reduction of aircraft engine and turbine noise, turbulent boundary layer noise has become a significant contributor to the interior sound field. Similarly, automotive engineers are increasingly concerned with the occupied environment for passengers. Major advances have been made to reduce the sound transmitted to the interior from the engine, transmission, and tires. As a result, reduction of aeroacoustic noise has become a priority.

Until recently, the only methods for controlling sound radiation were passive techniques. For control of sound radiated to an interior space, sound absorptive material, such as fiber linings, has been utilized. These treatments are reasonably effective for frequencies above 500 Hz. However, passive techniques are often ineffective for frequencies below 200 Hz. This is because fiber linings are most effective when applied using a thickness approaching 1/4 of the wavelength of the sound to be controlled. Since the wavelength at 200 Hz is large, control of noise at these frequencies by passive techniques requires a large amount of material which increases weight and reduces

interior space. Consequently, passive sound absorpt ve material has not been utilized for control of sound in this frequency range.

Additional methods of controlling sound radiation have involved modifying the vibrational characteristics of the structure radiating sound. Passive methods such as composite layers to increase damping, vibration isolators, and tuned vibration absorbers have been utilized with some success. However, these devices increase the weight of the structure and are often limited to control of a narrow frequency range.

With the development of high speed microprocessors chips, active noise control has now become a potential solution for the control of structural radiation of sound problems. With active control one or more secondary sources are utilized to change the dynamics of the structure such that the radiation of sound is reduced.

Recently, adaptive feedforward control schemes have been utilized to control noise problems. These methods require a deterministic excitation or a reference transducer. Furthermore, the disturbance information from the reference must be provided to the controller prior to the impact of the disturbance on the system. For turbulent flow excitation, the excitation is broadband in nature and a suitable reference source is not available. Thus, adaptive feedforward control is not a viable solution for this problem.

The only active control study of the turbulence induced structural radiation of sound to date addressed the problem using optimal feedback control. However, optimal control is not practical for this problem since it requires full state information. It is unlikely that the state information associated with the turbulent boundary layer or the sound radiation could be obtained through measurement or accurately modeled. Furthermore an optimal controller does not allow for uncertainty such as unmodeled modes and plant variations. For this reason, implementation of optimal control is rarely attempted.

As adaptive feedforward control and optimal control are not solutions to this problem, robust feedback control is studied in this investigation. Robust feedback control has not been widely applied to noise control problems. As a result, many associated

problems have not been fully addressed. In this investigation robust feedback control methodologies are utilized to identify and resolve these problems.

In this investigation a Multiple-Input-Multiple-Output (MIMO) robust feedback control methodology is investigated. The method is based on loop shaping the controller according to frequency domain design criteria. Using this approach, the controller is designed to be stable for all operating conditions while achieving prespecified sound pressure level reductions without saturating the control actuator. With this method, the sound pressure level of error microphones are specified as the performance parameter while plate acceleration feedback is used. In this work, appropriate modifications are made to the approach such that this method can be applied to lightly damped structural radiation of sound problems.

This work is organized as follows. Chapter 2 is a summary of the work related to the modeling and control of the flow induced structural radiation of sound problem. In Chapter 3, the analytical model of this problem is developed and evaluated experimentally. In Chapter 4, μ synthesis and adaptive feedback control methodologies are evaluated. In Chapter 5, robust frequency domain control is developed and evaluated for the flow induced structural radiation of sound problem. Conclusions and proposed future work are presented in Chapter 6.

CHAPTER 2. LITERATURE REVIEW

In this chapter, two areas of research pertaining to active control of flow induced structural radiation of sound are reviewed. Work related to modeling this problem is reviewed in the first section. In the second section, related active control investigations are discussed. The active control section is divided into active structural acoustic control, control of the sound radiated due to a turbulent boundary layer, and robust feedback vibration control.

2.1 Turbulent Flow Structural Excitation and Sound Radiation

The most common analytical solutions to aeroacoustic noise problems utilize the methods related to the Lighthill Analogy [1]. Such methods have been developed to model turbulent flow noise. One such method is given by Ffowcs Williams [2] who extended the Lighthill-Curle theory of aerodynamic sound to include convective motion of coherent structures. Turbulent eddies are shown to be equivalent to a quadrupole source which is coherent within spatial and temporal scales corresponding to the correlating length and lifetime of the turbulent eddy. For flow over one side of a plate, the Ffowcs Williams equation is useful only for sound radiated into the turbulent flow field. For the interior noise problem, there is not a direct path between the turbulent boundary layer and the interior acoustic field. Rather, the sound is generated from structural radiation through vibration induced by the turbulent flow. Thus, the Lighthill Analogy methods can not be used for the interior noise problem.

Researchers have separated the problem of the structural radiation of sound from turbulent flow into the three parts shown in Figure 2.1. The first part is a model of

the pressure field of the turbulent boundary layer impinging on the plate. The second part is a model of the structural response due to the turbulent pressure field. The final part is a model for the structural radiation of sound into an interior space. In an effort to keep the model as simple as possible, researchers have generally considered the structure to be a simply supported plate. Furthermore, the influence of the interior space is neglected by assuming the plate radiates into free space. Finally, the effect of the acoustic loading on the plate and the influence of the structural vibrations on the flow field are generally neglected.

2.1.1 Modeling the Turbulent Flow Field

An accurate model of the turbulent flow field has not been found. Despite many years of research and a large body of literature devoted to the fluid dynamics of turbulent flow, this phenomenon is poorly understood. The current state of turbulent boundary layer knowledge is given in a literature review by Robinson [3]. He states that many controversial issues exist in boundary layer theory such as the near-wall streak formation, the bursting process, mass and momentum transfer to and from the inner and outer fluid layers, the appropriate scaling variables for near-wall turbulence production events, and the existence and role of hairpin, horseshoe, and ring vortices.

2.1.1.1 Numerical Techniques for Modeling the Turbulent Flow Field

Although there is a lack of understanding of turbulent flow, many attempts have been made to calculate the flow quantities. Recent attempts have involved numerical simulations. Two popular techniques are the large-eddy simulation (LES) and the direct numerical simulation (DNS). In the LES model, the smallest scales of the flow are modeled while the remaining scales are computed directly from first principles using the Navier-Stokes equations. This is based on the observation that small scales in a turbulent flow are nearly universal while the larger scales are strong functions of the flow geometry and gross flow parameters. Unlike the LES, the DNS attempts

to resolve the turbulent motions at all relevant scales. Due to the intensive computational requirements of the DNS and LES, they have been limited to low Reynolds number flows. As a result, they are currently unusable for describing the fully developed outer layer of turbulent flow. Since the pressure signal felt in the wall region originates in the outer layer, the studies can not yet be used to accurately model the pressure at the wall. Thus, direct numerical methods are not useful for the structural excitation model being developed.

Various researchers have sought to reduce the computation time by using simple models based on observed turbulent flow characteristics. One such characteristic is the burst phenomenon. The burst is a localized ejection of fluid from the wall caused by the passage of one or more tilted quasi-stream-wise vortices which persist for longer time scales than do the observed ejection motions [3]. Breuer attempted to model the burst events as initial disturbances produced by a pair of counter-rotating eddies [4]. The mean flow profile was a Blasius velocity profile. The author states that the linear term in the Poisson equation dominates for large-scale fluctuations. Using the linear Poisson term ($\frac{\partial U}{\partial y}\frac{\partial u}{\partial x}$) and assuming inviscid equations, Breuer developed a system of equations which were solved numerically using a Crank-Nicholson scheme. The theoretical results for a single burst as it is convected downstream were compared qualitatively to experimental results. The model is said to differ from experimental results because of its neglect of viscous and nonlinear terms.

Another flow characteristic which has been studied using simplified numerical models is the hairpin vortices. The turbulence produced in the near-wall region is intermittent in space and time. A dominant model for this characteristic is the hairpin shaped vortex described by Smith [5]. The vortices are oriented in the stream-wise direction at an angle of 45 degrees to the wall. The legs of the hairpin are said to be counter rotating vortices that pump fluid.

Using the idea of the hairpin vortex, Bandyopadhyay attempted to numerically calculate the wall pressure fluctuation for a turbulent boundary layer [6]. He used an elliptic vortex inclined at a 45 degree angle as a model of a hairpin vortices.

As in the Breuer approximation, a Blasius mean velocity profile was used. The Navier-Stokes equations were solved numerically and the model was compared to experimentally obtained results. Comparisons were made to experimental data for the correlation coefficient between the wall pressure and the stream-wise velocity and the wall pressure and the surface normal velocity. The data obtained from the theoretical model is significantly different than that obtained experimentally. Furthermore, the theoretical model was found to be strongly influenced by the circulation chosen for the vortex. Although the experimental data did not confirm the theoretical model, it was deemed to be encouraging by the author.

2.1.1.2 Statistical Methods for Modeling the Turbulent Flow Field

Statistical models of the turbulent wall pressure levels have been utilized since the early 1960's. These methods are based on empirically obtained data. Unlike the recent numerical attempts, these models are able to characterize the pressure field on a plate for a fully developed turbulent flow. Furthermore, they have been shown to be accurate for a wide range of turbulent flow problems.

A well documented characteristic of a turbulent flow field is that coherent motions, with different structural characteristics, exist in the sublayer, buffer region, and outer region of the flow field [3]. Furthermore, the most common near-wall coherent motions (quasi-stream-wise vortices, shear layers, and velocity peaks) travel a significant distance downstream during their lifetimes. Willmarth reports that coherent motions can exist for distances on the order of 9 times the momentum thickness and have a stream-wise extent of 0.5 times the momentum thickness [7]. Various researchers have attempted to quantify the wall pressure fluctuations related to these coherent structures.

Astolfi performed an experimental study to find the relationship between the turbulent wall pressure fluctuations and the turbulent internal shear layer structures [8]. A velocity gradient probe, two wall pressure transducers in the stream-wise direction,

and three wall pressure transducers in the spanwise direction were used. The instantaneous velocity gradient, wall pressure fluctuations, and the stream-wise and normal velocities were measured simultaneously. Data acquisition was triggered when the normal gradient of the stream-wise velocity fluctuation ($\frac{\partial u'}{\partial y}$) exceeded its RMS value by a specified amount. A typical result is shown in Figure 2.2. The large normal gradient of the stream-wise velocity which triggered the measurement is shown in the top trace. The signals from two wall pressure transducers are shown in the bottom two traces. The wall pressure "foot-print" is a positive peak pressure at the wall with two negative pressure regions on each side. The pressure pattern is convected downstream from p_1 to p_2 in a time of Δt.

The periodic convection of these pressure footprints is the primary contributer to the wall pressure level. Schewe determined that the wall-pressure fluctuations are a very intermittent process where short time segments with large fluctuations follow long time segments with small fluctuations [9]. He suggests that the large fluctuations occur only 1% of the time but contribute approximately 40% to the RMS pressure.

In 1962, Willmarth *et al.* made measurements of the statistical properties of the wall pressure [10]. The correlation coefficient was calculated as a function of the dimensionless stream-wise separation and temporal parameters. The results are shown in Figure 2.3. The largest correlation is along the ridge in the first quadrant. This indicates that the coherent pressure producing eddies are carried downstream at a convection speed equal to the slope of this line in the space-time plane. The fact that the eddies gradually lose their correlation as they are transmitted downstream is seen by the decreasing amplitude of the ridge. An interesting note is that the ridge curves slightly towards the spatial axis. This is because the large pressure disturbances remain correlated for a longer time than smaller disturbances. Since these large disturbances extend further into the flow where the mean velocity is greater, they are pulled along by the higher mean velocity. Thus, their convective velocity is larger than smaller disturbances. Willmarth *et al.* reports that these large disturbances are

responsible for the majority of the low-frequency contributions to the the correlation coefficient.

A breakthrough in the statistical modeling of the wall pressure field was made by Corcos in 1963 [11]. Corcos was investigating the limitations of finite sized pressure transducers in turbulent flows. The spatial resolution of the wall pressure causes errors in the measurements of turbulent pressure fields. Corcos developed a correction method for these spatial errors. In his derivation, he considered the flow field to be stationary and homogeneous. Thus, the wall pressure cross-correlation is considered to be a function only of the spatial and temporal separation and not absolute position. This assumption is valid if the turbulent boundary layer thickness is constant and the mean pressure gradient is small [12]. With this assumption, Corcos postulated that the cross-spectral density of the wall pressure can be represented as

$$S_{ff}(\omega, \xi, \eta) = S_{pp}(w) A(\omega\xi/U_c) B(\omega\eta/U_c) exp(-i\omega\xi/U_c) \tag{2.1}$$

where U_c is the convective speed, ξ is the longitudinal separation, η is the lateral separation, and $S_{pp}(w)$ is the ordinary power spectrum. Although the Corcos model is simplistic, it is widely used in aeroacoustic models today. Modern texts, such as Blake, continue to use this method in the evaluation of the wall pressure for a turbulent boundary layer [13].

Various researchers have fit the A and B functions to empirical data. Originally, Corcos used empirical data from Willmarth and Wooldridge [10] to determine these functions. In 1967, Corcos compared his model to different sets of data [14]. Using data from Bull [15] and Priestly [16], Corcos was able to show that his form of the pressure cross-spectra was valid. Additionally, Strawderman utilized exponential decays to fit A and B [17]. Willmarth suggested the stream-wise decay is more rapid in adverse pressure gradients and less rapid in favorable pressure gradients [7].

Various values for the convection velocity have been suggested. Willmarth reports that the very small scale pressure fluctuations can travel as slow as 0.39 times the free stream velocity while large fluctuations can have a convective velocity of 0.8 times

the free stream velocity [7]. Strawderman [17] suggests using a constant convective velocity of $U_c = 0.65U_\infty$ while Schewe [9] suggests a convection velocity of $U_c = 0.53U_\infty$.

Bhat [18] measured the exterior pressure fluctuations on a Boeing model 737 airplane using an array of microphones. The measurements were performed at 7624 meters (25,000 ft) and Mach numbers of 0.45 and 0.78. The decay rate of the pressure cross-spectra was found to be slightly larger than that measured in laboratory tests. This was attributed to the angle of attack, wall roughness, and fuselage curvature. However, Bhat found that the spectrum, convection velocity, and space-time correlation measured in flight were comparable to the laboratory measurements of the turbulent boundary pressure fluctuations on a flat plate.

A crude model for the power spectrum of the wall pressure was suggested by Skudrzyk and Haddle [19] and more recently, by Schewe [9]. Both models assume that the power spectra of the turbulent boundary layer is approximately constant at low frequencies.

Other more complicated statistical models for the wall pressure field have been developed. Maestrello [20] developed a model of the cross correlation of pressure in which the A and B terms are exponential decay functions of the Reynolds number and the boundary layer thickness as well as the separation distance. Efimtsov [21] used a function of the Strouhal number and three empirical constants to describe each of the decay terms. At high frequencies Efimtsov's decay terms correspond to constant exponential decays.

The Corcos, Maestrello, and Efimtsov models have been compared by Tang *et al.* [22]. The Corcos model was found to estimate a slightly higher excitation at low frequencies. However, at frequencies greater than 500 Hz, each of the models provided similar results. The authors concluded that there is little significant differences among the results given by these models.

2.1.2 The Structural Response

An accurate model of the structural response is important for the stability of an active feedback controller design. However, in practice an exact model will never be obtained. Slight differences in the boundary conditions and unmodeled modes of a structure will cause variations in the structural response. Significant uncertainty is caused by variability in the manufacturing process as has been observed for new same model automobiles by Kompella and Bernhard [23]. Uncertainty is also caused by fatigue and aging of the structure. Finally, environmental changes significantly affect the structural response. For example, changes in aircraft altitude alter the response of the aircraft structure. The controller design must account for the uncertainty associated with a given model.

Prior to the development of the Corcos model, researchers had determined how to calculate the structural response of a plate to an external pressure field. In 1957, Eringen published such a method [24]. Eringen utilized generalized Fourier analysis techniques and a modal solution to determine the vibration of bars and plates under stochastic loads. The cross-power spectra of the force was written as a function of the cross-power spectra of the pressure field. The modal analysis technique he described is commonly used in today's research.

Dyer [25] was one of the first to attempt to find the excitation of a plate by a turbulent pressure field. The thin plate equation for a simply supported plate model was solved using a modal solution similar to that of Eringen. Dyer assumed the pressure from a turbulent flow field is random having a correlation which decays with time, has a spatial extent that is vanishingly small, and is convected along the surface of the plate. The approximation of the pressure field is less accurate than that of the Corcos model because it assumes the flow is fully correlated over a finite correlation area and uncorrelated outside this area. For short correlation lifetimes, Dyer's flow field model describes a non-convecting purely random pressure field.

In 1968, Strawderman [17] used a modal solution, similar to that of Eringen, to find the plate velocity of a turbulent flow excited, simply supported, rectangular flat plate. The boundary layer pressure model was that suggested by Corcos [11]. The convection velocity was taken to be a constant ($U_c = 0.65U_\infty$) and the Skudrzyk and Haddle [19] approximation for the pressure power spectrum was employed. The pressure on the plate due to the radiation of sound was considered negligible compared to the turbulent boundary layer pressure fluctuations. Thus, the boundary layer provided the only excitation in the model. This approximation is valid when the fluid is air. Strawderman found that the modal frequencies in his predictions varied slightly from experimental data. He attributed these errors to differences between the analytical and experimental boundary conditions. Despite the difference in the modal frequencies, the vibration amplitudes were found to be similar to predicted results.

In 1968, Strawderman [12] compared the results he obtained for his modal solution to results obtained using a wavenumber transform solution. Although useful estimates were obtained, he stated that neither model produces results that fully agree with experimental results.

2.1.3 The Radiation of Sound

The radiation of sound is the final part of the turbulent flow induced structural sound radiation model. There have been numerous methods developed to calculate the sound pressure and sound power radiated by a panel. White used a joint acceptance method to calculate the sound power radiated from a plate excited by turbulent flow [26]. Each joint acceptance is a function of the cross-correlation functions of the pressure on the plate and the mode shapes of the plate. The joint acceptances for each mode are multiplied together and the average is taken for a frequency band around the modal frequency.

Using his method of joint acceptances and the Corcos model of the flow excitation, White estimated the sound power radiated from a plate due to a turbulent boundary layer [26]. In order to simplify the complicated computation of the average joint acceptance, White assumed the correlation length of the turbulence was less than the panel dimension. In this manner, the exponential terms in the Corcos model were neglected. The resulting integral for the average joint acceptance was evaluated numerically. The White model was not found to accurately predict experimental results. The author suggests a better knowledge of the boundary layer constants and a more accurate knowledge of the plate radiation resistance would have improved the model.

Maestrello [27] obtained good results for his prediction of the sound power radiated from a simply supported plate under turbulent pressure fluctuations. He used a model similar to that of Corcos to represent the space-time correlation of the wall pressure fluctuation. However, Maestrello used a larger convective velocity for lower frequency wave numbers and a smaller convective velocity for higher frequency wave numbers. A modal approach, where both acoustic and structural damping were considered, was used to determine the cross-power spectra of the panel displacement. Due to limited computer resources, the numerical integration was too time intensive. As a result, the structural cross-modal coupling was neglected. With this assumption the sound power level was estimated by a modal volume displacement method. With this method, the sound radiation of the panel is related to the volume velocity of each mode. The theory and experiment were shown to be in good agreement for various experimental configurations.

2.2 Active Control Related to the Flow Induced Structural Radiation of Sound

Practical solutions to the problem of active control of flow induced structural sound radiation have not been published. This problem includes many characteristics

which make it a challenging system to control. Turbulent flow excitation is broadband in nature with no suitable reference signal available. Therefore, feedforward control algorithms cannot be used for this problem. Furthermore, the states associated with turbulent flow excitation and sound radiation are unmeasurable and an accurate model is not available. Thus, state space based control schemes are also ineffective for practical implementation. Since pressure levels are significant over a large frequency range and the frequency response of the lightly damped structures does not roll off significantly, a large controller bandwidth is a requirement for this problem. The system delay is also a significant characteristic of this problem. Not accounting for this delay leads to poor system performance or system instability. Non-linearities and unmodeled system dynamics must also be considered. Furthermore, since the plant dynamics exhibit large system uncertainty, robustness must be addressed.

In the first part of the following section, recent active structural acoustic control schemes are summarized. Next, several active control schemes for reducing the flow induced structural radiation of sound are described and problems associated with the implementation of these schemes are identified. In the concluding section, the limited application of robust feedback control to both vibration and sound radiation problems is described.

2.2.1 Active Structural Acoustic Control

Significant work in Active Structural Acoustic Control (ASAC) has been performed using feedforward control techniques. Such methods require either a deterministic excitation or a reference transducer which provides highly coherent disturbance information. The disturbance information from the reference must be provided to the controller prior to the excitation of the system by the disturbance. Since the boundary layer excitation has limited correlation in space and time, a highly coherent

reference source is not available. Therefore, feedforward control schemes are ineffective. Although the feedforward control schemes are not an effective solution for the flow induced structural radiation problem, specific case studies have led to an understanding of the active control of the structural radiation problem. Therefore, the relevant portion of the feedforward ASAC literature is reviewed. Simple feedback and optimal control ASAC schemes are also reviewed.

Guigou *et al.* [28, 29] utilized a Filtered-X feedforward controller to reduce the sound from a clamped edge semi-infinite vibrating beam. Shakers mounted near the clamped edge were used as control actuators and microphones were used as error sensors. The disturbance was a harmonic point force excitation of the beam. This excitation signal was also supplied to the feedforward controller as a reference input. Two key results were reported. Through experimentation Guigou *et al.* showed that the attenuation of the radiated acoustic field may not correspond to a decrease in amplitude of the global vibration response of the system. Thus, vibration control may not provide the best acoustic control. Secondly, it was shown that control of the pressure level at one point in the acoustic field also provided acoustic far-field sound radiation attenuation. Therefore, it is possible to achieve global sound pressure level reduction by considering control of the sound pressure at one or more discrete locations.

A feedforward filtered-X controller was also used by Clark *et al.* [30] to control the sound radiated from a vibrating, simply supported rectangular plate. The plate was driven by a harmonic excitation from a shaker. As in the work of Guigou *et al.*, it was shown that the modal response of the plate increased while the acoustic response was reduced. Additionally, piezoelectric film was shown to be as effective an error sensor as a microphone. Thus, measurement of the sound pressure was not required to achieve sound pressure level reductions.

In addition to feedforward controllers, simple feedback ASAC schemes have been used with a varying degree of success. The simple feedback schemes feed an error signal directly into a control actuator. Little or no controller dynamics are included.

Thus, the open loop transfer function is completely based on the system dynamics. Since controller dynamics are not used to ensure stability margins or to roll off the controller response at high frequencies, the simple feedback schemes can result in closed loop unstable systems.

Akishita and Mitani [31] considered active control of the vibration of a panel for acoustic purposes. An acoustic disturbance was applied to one side of the panel using a loudspeaker. Piezoelectric devices were used both as controller actuators and sensors. The feedback controller was a proportional-derivative scheme. Numerical simulations showed 20-30 dB reductions in the sound pressure level. However, upon implementation, the controller was found to be unstable at high frequencies. Although the authors attribute the instability to nonlinearities in the actuators, the actual cause of the instability is unmodeled higher frequency plant modes.

Another simple feedback scheme was proposed by Hong *et al.* [32]. This work investigated the active control of an automobile fuel tank for acoustic purposes. Piezoelectric discs were used both as actuators and sensors. Control was achieved with constant gain velocity feedback and a phase shifter. The gain and phase were adjusted manually to provide the best noise reduction. Unlike Akishita and Mitani, a low pass filter was also included in the controller. The low pass filter rolled off the controller response such that the higher modal resonances would not be driven to instability. Parametric system uncertainty, the key justification for feedback control, was not considered in their work. Therefore differing levels of fuel in the tank required different controller phase and gain settings. For properly adjusted controller settings, the first mode was controlled by 25 dB and the second and third modes were controlled by 18 dB and 14 dB respectively.

Falangeas *et al.* [33] considered active damping of a plate using rate feedback control. Accelerometers were used for feedback and piezoelectric actuators were used for control. The disturbance was a random shaker excitation of the plate. To obtain rate information the accelerometer signals were integrated. The integrated signals were amplified and used to drive the control actuator. The gain was experimentally

tuned until the system became unstable. Instability was observed at high frequencies because of phase lag in the actuators and computational delay. One problem with rate feedback is that all the modes are controlled even when control is not necessary. To reduce the control effort at higher frequencies, roll-off filters were tested. However the additional phase lag of these filters was not considered and the controller became unstable.

The popular full state feedback methodology has also been investigated for ASAC. Full state feedback controllers require an accurate model of the system and measurable system states. For some ASAC problems, these states do not correspond to measurable quantities. Doyle has shown that if an observer is used to estimate the unmeasurable states, the gain margins may be arbitrarily small [34]. Furthermore, since parametric and unstructured system uncertainty are not included in the model, the controller is not robust. For these reasons full state feedback control is not often implementable.

Meirovitch and Thangjitham [35, 36] investigated active control of sound radiated from a plate using a state space model of the plate vibration. Uniform single frequency plate disturbances were considered and ideal modal sensing was assumed. The control actuators were multiple point force inputs. LQR theory was used to design the optimal controller. However, the selection of the terms of the Q and R weighting matrices was not discussed. The Rayleigh integral was used to calculate the sound pressure level at various locations. Numerical simulations were used to determine the effect of various excitation frequencies, differing number of controller actuators, and two different actuator arrangements. It was shown that considerably more controller actuators were necessary to control high frequency excitation than low frequency excitation. Furthermore, the choice of which modes to control influenced the results more than the actuator arrangement. The best results were obtained by controlling the modes having frequencies near the excitation frequency. State measurement, unmodeled dynamics, non-linearities, system delay, and system uncertainty were not considered. These are significant factors associated with control of flow induced structural radiation

of sound. Thus, this work has not shown that state space control schemes can be successfully used for this problem.

From feedforward ASAC studies, it was shown that vibration control does not guarantee the lowest sound pressure level reductions. For this reason, several researchers have developed state space models that can be used to weight modal accelerations to improve ASAC. Such methods are useful when the acoustic field cannot be directly measured. This is often the case for feedback control where the delay associated with the propagation of sound severely limits controller performance.

Baumann *et al.* [37] have developed one method of designing state space based feedback controllers to attenuate sound radiation without directly measuring sound pressure levels. The acoustic dynamics associated with the radiated power are contained within the plant model. A radiation resistance matrix $M(s)$ is derived using the Rayleigh integral equation. Off-diagonal terms correspond to the mutual radiation efficiencies while the diagonal entries represent the self-radiation efficiencies. The off-diagonal terms represent the radiated power due to one structural mode as influenced by the amplitudes of the other structural modes. A spectral factorization of $M(s)$ is performed which results in a matrix of causal radiation filter transfer functions which give the time histories of each radiation mode from the time histories of the structural vibration modes. The 2 norm of the output from these radiation filters is the power radiated from the structure. In practice it is difficult to perform the spectral factorization on $M(s)$. The radiation filters are placed in state space form which allows their use in designing a controller to minimize radiated power.

More recently, Elliott and Johnson [38] have developed expressions for the total acoustic power output in terms of the velocities of an array of elemental radiators. Their method is equivalent to that suggested by Baumann *et al.* [37]. The elemental radiators are used such that the amplitudes of the radiation modes are defined without reference to structural mode amplitudes. In this way, the amplitudes of the structural modes do not have to be calculated. Rather, an array of point vibration

sensors could be measured and weighted to achieve sound power reduction. Alternatively, distributed sensors could be shaped to respond to the structural excitation corresponding to a radiation mode.

Several studies have used the method of Baumann *et al.* [37] to design optimal feedback controllers for ASAC. One such study by Baumann *et al.* [39] considered control of the sound radiation from a baffled clamped-clamped beam. The disturbance was a bandpassed white noise point force input. The controller actuation was also a point force input to the beam. The beam was modeled using the first three modes and ideal sensing was assumed. The dynamics associated with the radiated power were 12th order. A LQG controller was designed with minimal weighting on the control effort. This control was compared to that from a LQG controller designed to attenuate the modal vibration. Numerical simulations showed that the acoustic controller attenuates the sound power by 10 dB more than the vibration controller. System uncertainty and the implementation of full state feedback were not discussed.

2.2.2 Active Control of the Flow Induced Structural Radiation of Sound

Only a handful of studies have addressed active control of flow induced structural radiation of sound. Parker *et al.* [40, 41] purport to have studied the reduction of flow-induced vibration in aircraft panels using active control. They reported using an adaptive nonlinear infinite impulse response (IIR) polynomial neural network based feedback controller. A two mode clamped beam model was considered. The covariance structure of the turbulent flow field was described using the Maestrello turbulent flow model [42] and used to generate time history inputs to each mode. The controller was designed with the assumption that individual modes can be measured and controlled. A third order IIR feedback controller filter fit was developed off line using a guided random search on 1000 0.25 second white noise input sequences. No measurement error or uncertainty was considered. With this filter, the average modal

vibration energy was reduced by 31 dB. However, the sound radiation from the beam was not considered.

Peterson *et al.* [43] implemented a multichannel active control approach which was motivated by the broadband random noise in aircraft cabins. The authors approached this problem as a sound transmission problem rather than a structural sound radiation problem. The turbulent boundary layer was said to be a sound source rather than a excitation source. As a simple case of this problem, sound transmission through a rectangular panel mounted in a transmission loss test facility was investigated. Broadband pseudo-random noise was generated by a loudspeaker in the source room. A feedforward control scheme was implemented. Feedforward control was made possible in their investigation by utilizing a microphone placed directly in front of the loudspeaker as a reference transducer. No other study of flow induced structural radiation of sound has assumed a reference transducer is available. The control actuators were eight piezoceramic actuators bonded to the panel. The controller filters were chosen to minimize the sound pressure radiated at seven error microphone locations. Although the transmission loss was increased by 5-10 dB at the error microphone locations, it was decreased up to 8 dB at other microphone locations. These poor results were attributed to overdriving the control actuators. The results were improved by shortening the periodicity of the excitation source. This suggests that the controller was adapting to the deterministic pseudo-random patterns of the source rather than controlling a broadband excitation. Furthermore, the authors acknowledged that an appropriate sensor for measuring the turbulent induced noise source will have to be found in order to utilize their controller. However, no suggestions as to what such a sensor would be were given.

Thomas and Nelson [44] performed a simplified experimental investigation of feedback control to reduce the sound transmission of turbulent boundary layer noise. A double walled panel was driven using broadband structural excitation to emulate the turbulent flow excitation of an aircraft panel. The acceleration of the center of the second panel was used as feedback and a loudspeaker mounted between the panels

was used as the control actuator. Since the panels were mounted on flexible gaskets, the radiated sound of the second panel was dominated by the rigid body mode. For this configuration, a reduction in the velocity of the center of the panel yielded a significant reduction in the radiated sound. Assuming rigid panels, a first principles state space model of the plate dynamics was developed. Fourth order lowpass anti-aliasing and reconstruction filters were also included in the model. A LQR controller was designed and implemented digitally as an IIR filter. The experimental results did not match the predicted results. Although sound pressure level reductions at 105 Hz were predicted to be 19 dB, only 8 dB of reduction was achieved. Additionally, significant control was achieved only for frequencies below 100 Hz. The results were disappointing and the authors suggest improvements could be made by using a system identification based model of the plant. However, the delay associated with the loudspeaker actuator was not included and was a potential factor limiting the controller performance.

Thomas and Nelson [45, 46] improved on their previous double panel investigations by utilizing a discrete time feedback controller. By assuming the plant dynamics are known through measurement, the feedback problem was formulated as a feedforward problem. In this way a SISO feedback LQG controller was designed by solving the Weiner-Hopf equation. The causal part of Weiner-Hopf filter was extracted using the Diophantine equation. The plant transfer function used in the controller design was estimated using a 15th order ARX model. The controller was implemented on the same two-panel system described previously. The controller was designed to minimize a cost function based on control effort and the acceleration of the center of the second panel. Between 5 and 15 dB of reduction were obtained over the 50-150 Hz region. The sound pressure levels were increased at higher frequencies. This increase was attributed to the dynamics of the panel.

Recently, Thomas *et al.* [47, 48, 49, 50] performed an extensive evaluation of the active control of sound radiation from a simply supported panel excited by a turbulent boundary layer. To evaluate active control, a numerical model of the system was

developed. The Corcos statistical description was utilized to represent the effects of the turbulent flow. One assumption was that the vibration of the plate does not couple with the turbulent boundary layer. Furthermore, the cross-terms in the power spectral density of the velocity of the plate were neglected. This assumption is valid only if the correlation lengths in both the longitudinal and lateral directions are significantly smaller than the dimensions of the plate. Although this condition was not satisfied, it was anticipated that the results will be valid near the resonances of the various modes when the modal density and structural damping are low. By neglecting the cross-terms, the power spectral density of the boundary layer pressure was written as a sum of modal forces excited by the turbulent boundary layer. In this manner, the integral solution for the spectral density of the generalized force exciting the nth mode was analytically evaluated. A state equation representation of the force due to the boundary layer excitation was developed using a spectral factorization of the generalized force. For this study a seven mode model of the plate dynamics was utilized. The proposed method of Baumann *et al.* [37] was used to develop the transfer function from the modal acceleration to sound power.

With this model Thomas *et al.* used numerical simulations to evaluate optimal feedback control. Controllers having both one and two point force actuators were evaluated. The two channel controller was able to achieve significant reductions at all frequencies while the single control actuator case could not control the radiated sound power between the modal peaks. Sound power reductions of 30 dB at the first mode and approximately 10 dB at the other 6 modeled modes were found. The authors state that full state feedback, as used in this simulation, is impractical. Furthermore, an accurate model of the dynamics of the excitation, structural response, and sound radiation is unrealistic. Finally, delays, unmodeled dynamics, nonlinearities, and other uncertainties are not incorporated in the analysis. These characteristics of the flow induced structural sound radiation problem will reduced the performance

of an actual implementation. Despite the apparent success of this state space optimal control simulation, the problems with implementation of the method make this solution inappropriate for this problem.

2.2.3 Robust Feedback Vibration Control

Because feedforward and optimal full state feedback control techniques are not well suited for the active control of the structural radiation of sound due to a turbulent boundary layer, other control methods must be considered. Robust feedback control methods such as H_∞, μ synthesis, and QFT offer the most promise. Vibration control of lightly damped modal systems and a few ASAC studies have utilized robust feedback control. These studies are reviewed here.

Banks *et al.* [51] performed an analytic study of active control of structural sound radiation. They considered control of sound inside a concrete cylinder with a thin circular flexible plate at one end. A two dimensional model was developed using a Galerkin discretization scheme. A piezoceramic strain model was used for both control actuation and feedback information. The excitation of the plate was harmonic in nature and supplied via an exterior noise field. The H_∞ control methodology was utilized to design a controller based on the plant output. Three displacement sensors, three velocity sensors, and 5 microphones were used for feedback. The results of this controller were compared to those of an LQR controller for the same system. The LQR controller development is described in an earlier publication by Banks *et al.* [52]. Although the LQR controller performed better than the H_∞ controller, the H_∞ controller was reported to perform satisfactorily. In general 12-15 dB of reduction was predicted at a microphone location. At off resonant excitation, the H_∞ controller increased the sound pressure level of higher frequencies. The initial conditions were found to substantially effect the H_∞ controller results. Furthermore, the location and number of microphones used as feedback influenced the conditioning of the Riccati

solution. Solutions where the condition number was poor resulted in unbounded sound pressure levels. These configurations were said to be poor.

Falangeas *et al.* [33] considered H_∞ control for the active damping of a plate. Accelerometers were used for feedback and piezoelectric actuators were used for control. A random shaker excitation of the plate served as the disturbance. A two mode state model was used to describe the system. Neither the uncertainty of the plant model nor the time delay were included in the model. To prevent the unmodeled modes from causing closed loop instabilities, the high frequency modes were filtered using a low pass filter. In addition, a high pass filter ensured a low gain at DC such that a constant deflection did not occur. The first H_∞ design resulted in system instability. Consequently the plant was augmented with the additional dynamics of a notch filter so that the controller gain would be attenuated at the frequencies causing instability. The redesigned controller was a 15 order three-input three-output controller. The first and second mode of vibration were reduced by 10 dB and 7 dB respectively.

Smith *et al.* [53] utilized H_∞ synthesis to design controllers for vibration control of a lightly damped flexible truss. The feedback sensors were three accelerometers mounted at the end of the truss. The control actuators were three adjustable truss members. The importance of the uncertainty classification was illustrated by designing controllers based on two different uncertainty structures. In the first structure, both additive and multiplicative uncertainty were included on the output. Implementation of the controller resulted in unstable closed loop systems. The authors concluded that the uncertainty did not adequately characterize the errors in the system model. The second uncertainty structure included additional additive and multiplicative uncertainty on the output and multiplicative uncertainty on the input. The revised uncertainty structure resulted in a stable closed loop system. The authors suggest design iterations based on experimental investigations in order to improve stability and performance since it is difficult to pick the appropriate uncertainty structure *apriori*.

Balas and Doyle [54] utilized μ synthesis to control the vibration of a lightly damped, modal structure. The disturbance was air blowing over the surface of the structure. The structure was empirically modeled by fitting transfer functions to experimental data. Additive uncertainty was used to represent the unmodeled high frequency dynamics in order to avoid instability in the closed-loop system. The additive uncertainty was such that at higher frequencies the controller gain rolled-off and the higher frequency modes were not destabilized. Frequency domain weights were also included to limit the actuator responses. The performance weight for vibration attenuation was a constant scaling on each sensor output. Controllers were designed using various levels of additive uncertainty. A D-K iteration procedure approximating μ synthesis was employed to design the controllers. A three-input three-output, 90th order controller was developed. Experimental results indicated significant attenuation of the first two modes. As with the Smith investigation, the key step in the controller design procedure was to accurately capture the amount of uncertainty. Underestimating the system uncertainty either destabilized higher frequency modes or led to severe performance degradation. However, over estimating the uncertainty restricted controller performance.

Yang *et al.* [55, 56] utilized an H_∞ feedback control for sound pressure reductions inside an enclosure. Their work is unique in that sound pressure measured by a microphone was used directly as feedback. Sound pressure feedback was possible for this case due to the size of the enclosure (1.0 x.75 x 0.45 m) which limited the delay associated with the propagation of sound. Two loudspeakers were used, one as the control actuator and one as the disturbance. The disturbance transfer function was modeled as a 31 state system and the plant was modeled with 28 states. Since the H_∞ controller has the same number of states as the system model, the model order had to be reduced. For this reason the plant model was simplified leading to a reduced controller order of 12 states. Additive uncertainty was used to account for unmodeled dynamics. The additive uncertainty was a transfer function that bounded the magnitude difference between the frequency response derived from experimental data

and the frequency response of the reduced-order model. The closed loop sensitivity was weighted to ensure a 16 dB reduction of the first acoustic mode. To account for sensor noise and actuator output limitations, the complementary sensitivity was also weighted. The 20th order controller was implemented on a DSP board. With this controller the resonant peak was suppressed by 16 dB.

Chait *et al.* [57, 58] have utilized a combination of QFT and H_∞ to control noise in a duct. Since a reference sensor is available for duct applications, feedforward control is possible. However, feedback control is useful for dealing with system uncertainty. For this reason, the authors implemented a combination feedforward and feedback controller. The authors state that their fixed filter design guarantees performance and does not have the stability problems associated with adaptive control schemes. The controller inputs were a detection microphone and an error microphone. The controller actuator was a speaker. H_∞ synthesis was utilized to design an initial controller. QFT was then utilized to reduce the conservativeness in the controller design thereby increasing the controller performance. Due to the acoustic feedback path, the two control loops could not be designed sequentially. Therefore, in the QFT design process the feedback portion of the controller was fixed while the feedforward portion was designed. Next, the feedforward portion was fixed while the feedback portion was designed. The controllers were 50th order and were implemented on a DSP system. Reductions of 10-20 dB were achieved over the 100-500 Hz band. The authors suggest further research is necessary in the area of robust design for environmental and geometric variations in the duct.

Fluder and Kashani [59] investigated robust control of structure-borne noise using a μ synthesis design technique. Although vibration feedback was used, emphasis was placed on those modes which most efficiently radiate sound. A simply-supported rectangular plate with a broadband point force disturbance excitation was considered. A five mode model of the plate dynamics was developed. Co-located point force actuators and point acceleration sensors were used. A model of the radiation of sound from the plate was not used as it would have added many additional states. To

account for the sound radiation, each modal acceleration was weighted by its sound radiation efficiency. To prevent actuator saturation, a weight was also developed to limit controller effort. Structured uncertainty was included for a one percent variation in the natural frequencies and five percent variation in the damping ratio. Unstructured uncertainty, introduced as additive uncertainty, was used to account for the unmodeled modes. A second order transfer function was used to bound the difference between the 5 mode model and a more accurate model of the system. A D-K iteration procedure was used to determine the μ controller. Constant D-scales were used such that no additional states were added to the model. The synthesized controller was 14th order. Although robust performance was not guaranteed, robust stability was guaranteed. Numerical simulations showed that approximately 20 dB of attenuation of the SPL associated with the first mode was achieved. Furthermore there was no control spillover to higher modes.

2.3 Conclusions

The problem of modeling the flow induced structural radiation of sound has been approached in three steps, the model of the turbulence induced pressure field on a panel, the model of the structural response of the panel, and the model of the structural radiation of sound. Various modeling methods have been described for each of these steps. The structural response of the panel to a pressure field and the radiation of sound from the panel are relatively well understood. However, there is a lack of accurate models of the turbulence induced pressure field on the panel. Consequently statistical based models, such as that proposed by Corcos, have been utilized. These methods are apparently the state of the art and will be used for this investigation.

Active structural acoustic control has been implemented primarily with feedforward control methods. These studies illustrate the principles of structural acoustic

radiation and are useful for understanding how active controllers should be configured. However, the reference input required for a feedforward controller is not available for the turbulent flow excitation problem. For this reason, feedback control is considered in this study.

Currently the active control of flow induced structural radiation of sound has not been effectively addressed. A realistic experimental controller implementation has not been performed. Furthermore, the controller design techniques have not considered robustness to plant variations and other practical implementation challenges.

In the only significant study of sound radiation from a plate excited by a turbulent boundary layer, Thomas and Nelson used an optimal full state feedback controller. Optimal control is not practical for implementation as it is difficult or impossible to measure the state information required by the controller. Furthermore, the effects of delays, nonlinearities, unmodeled modes, and other uncertainties cannot be included in optimal control design techniques.

Various robust control strategies have been successfully applied to vibration control problems. Furthermore, a few researchers have used robust feedback control for noise reduction applications. Robust feedback control methodologies offer the best prospects for the active control of the structural radiation of sound due to a turbulent boundary layer. In this investigation robust feedback control will be investigated for active control of the flow induced structural radiation of sound problem. A robust frequency domain approach will be developed which considers system uncertainty, utilizes favorable plant characteristics, and achieves desired sound attenuation subject to an actuator output constraint.

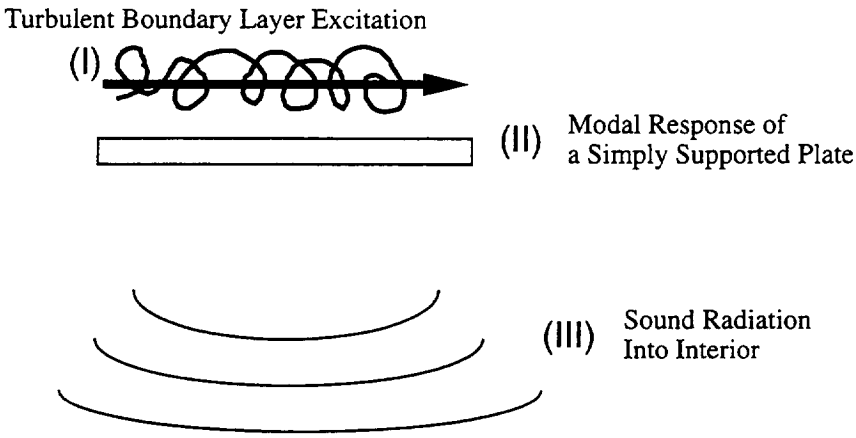

Figure 2.1 Diagram of Analytical Model

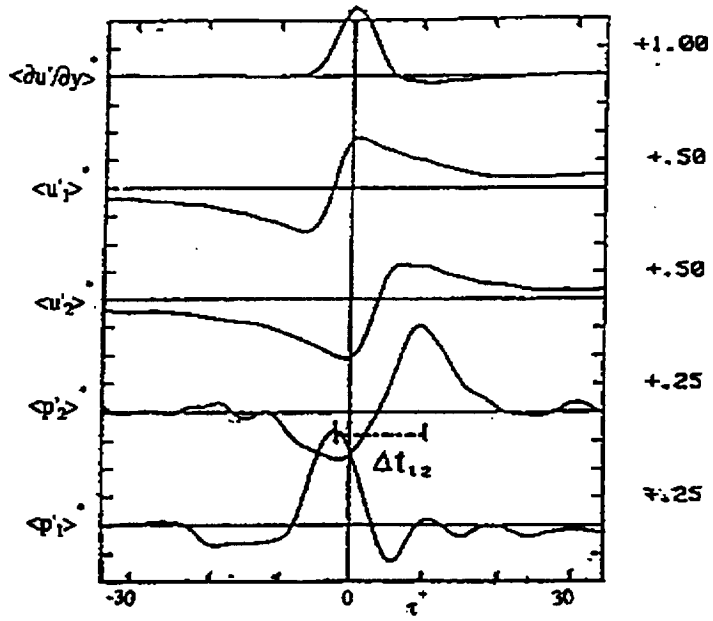

Figure 2.2 Pressure "foot-print" for a Large Velocity Fluctuation (Astolfi, 1993)

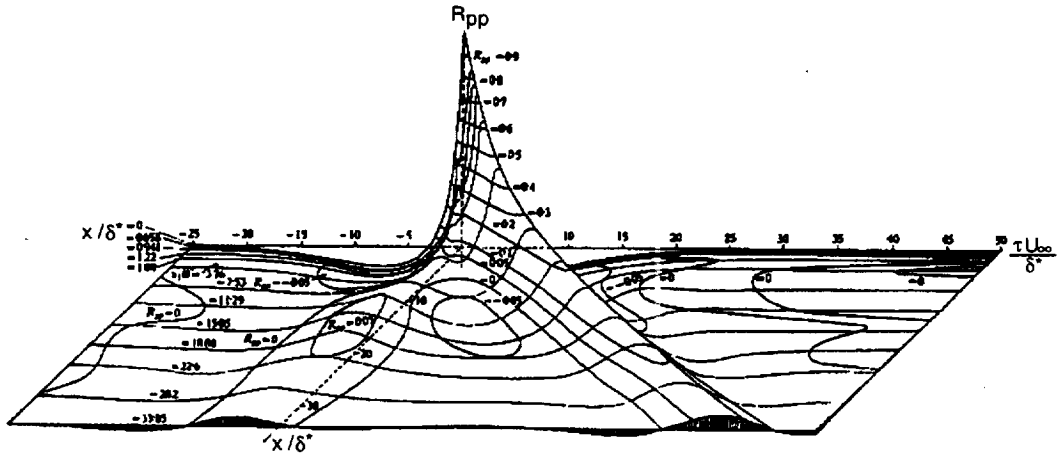

Figure 2.3 Space-Time Correlation Coefficient of Wall Pressure (Willmarth, 1962)

CHAPTER 3. ANALYTICAL MODEL DEVELOPMENT AND EVALUATION

In this chapter an analytical model is developed for the problem of structural radiation of sound from a simply supported panel excited by a turbulent boundary layer. Using this model, the predicted sound pressure level is compared to experimental data. A description of the experimental apparatus used to perform the investigation is also included.

The analytical model is necessary to estimate the sound pressure resulting from the structural response of a simply supported panel to a turbulent boundary layer. The model is used to evaluate H_∞ and μ synthesis controller design techniques for this problem. It is also used to develop the frequency domain design technique for the turbulent flow structural sound radiation problem. In addition, the analytical model is used in the optimization of the controller actuator and sensor locations.

The model is composed of three sets of transfer functions as shown in Figure 3.1. The first set ($G_D(s)$) is the generalized modal forces which capture the modal excitation of the plate due to the turbulent boundary layer. For a disturbance due to a point force excitation, these transfer functions are constants. However, for the turbulent boundary layer excitation they are shaping filters that give the appropriate modal force assuming a white noise input. The second transfer function set ($G_U(s)$) represents the modal response of the plate. The third transfer function set ($G_R(s)$) models the relationship between the modal amplitudes of the plate and the sound pressure level at a specified location. The complete analytical model uses 50 modes.

3.1 Structural Response Model

The structural response of the plate is obtained from the classical equation of motion for a thin damped flexible structure

$$D_o \nabla^4 u + c\frac{\partial u}{\partial t} + m\frac{\partial^2 u}{\partial t^2} = f(x, y, t). \tag{3.1}$$

where u is the normal displacement of the plate, D_o is the flexural rigidity, c is the viscous damping coefficient, m is the mass per unit area of the plate, $f(x, y, t) = f(x, y)s(t)$ is the excitation pressure of the plate, and ∇^4 is given by

$$\nabla^4 = \frac{\partial^4}{\partial x^4} + 2\frac{\partial^2}{\partial x^2 \partial y^2} + \frac{\partial^4}{\partial y^4}. \tag{3.2}$$

Using the modal analysis method and assuming simply supported boundary conditions, Equation (3.1) can be transformed into a set of algebraic equations. The assumed solution is given by

$$u = \sum_{r=1}^{\infty} \eta_r \Psi_r(x, y) \tag{3.3}$$

where η_r is the modal displacement associated with the rth mode and Ψ_r is the corresponding mode shape of the plate. For simply supported boundary conditions Ψ_r is given by

$$\Psi_r(x, y) = \frac{2}{(ab)^{1/2}} \sin(\frac{p\pi x}{a}) \sin(\frac{q\pi y}{b}). \tag{3.4}$$

where a, b are the x and y dimensions of the plate and p and q are the rth modal indices. The modal equation can be written as

$$\ddot{\eta}_r + 2\zeta\omega_r\dot{\eta}_r + \omega_r^2\eta_r = q_r \tag{3.5}$$

where ζ is the damping ratio ($c = 2\zeta m\omega_r$), q_r is the generalized modal force given by

$$q_r = \frac{1}{m}\int_S \Psi_r(x, y) f(x, y, t) dS, \tag{3.6}$$

and ω_r is the natural frequency of the rth mode given by

$$\omega_r = \sqrt{\frac{D_o}{m}} \left[\left(\frac{p\pi}{a} \right)^2 + \left(\frac{q\pi}{b} \right)^2 \right]. \tag{3.7}$$

For a point excitation of the plate, the generalized modal forces are given as

$$q_r = \frac{f}{m} \sin\left(\frac{p\pi x_o}{a} \right) \sin\left(\frac{q\pi y_o}{b} \right) s(t) \tag{3.8}$$

where x_o, y_o are the coordinates of the excitation. For the turbulent boundary layer excitation, the output of the spectral factorization shaping filters ($G_D(s)$) are the generalized modal forces.

3.2 Turbulent Flow Model

As shown in the literature review, accurate models of turbulent flow fields do not exist. The fluid dynamics of the turbulent flow phenomenon remain an area of fundamental research. Fortunately, stability of the robust feedback regulator problem does not require an accurate disturbance model. In this section, an empirically based turbulent flow disturbance model is developed for use in the controller design process.

3.2.1 Turbulent Flow Power Spectra

The most commonly used models of a turbulent flow field are statistically based. Statistical models of the turbulent wall pressure levels have been utilized since the early 1960's and are based on empirically obtained data. These models are used to characterize the pressure field on a plate for a fully developed turbulent flow. Furthermore, these models have been shown to be accurate for a wide range of turbulent flow problems.

The pioneering work by Corcus described in Chapter 2 led to a statistical model of the wall pressure cross-spectral density (Equation 2.1) which is used in this work. The

A and B functions are those suggested by Strawde man for a zero pressure gradient flow

$$\begin{aligned} A(\omega\xi/U_c) &= e^{-\gamma_1|\omega\xi/U_c|} \\ B(\omega\eta/U_c) &= e^{-\gamma_3|\omega\eta/U_c|} \end{aligned} \tag{3.9}$$

where $\gamma_1 = 0.115$ and $\gamma_3 = 0.7$ [17]. The convective velocity (U_c) is assumed to be a constant given by $U_c = 0.65\ U_\infty$ where U_∞ is the free stream velocity. The model for the power spectral density of the wall pressure suggested by Skudrzyk and Haddle is used [19]. At the low normalized frequencies, which are of concern here, the power spectral density of the pressure field is approximately the constant

$$S_{pp} = 7.5 \times 10^{-5} \lambda^2 \rho_o^2 U_\infty^3 \delta^* \tag{3.10}$$

where $\lambda = 3$ for air, ρ_o is the density of the fluid, and δ^* is the boundary layer displacement thickness. This approximation is reported to be valid up to a frequency of

$$\frac{2\pi U_\infty}{5\delta^*}. \tag{3.11}$$

For this investigation δ^* is assumed to be constant across the plate and is chosen to be the displacement thickness at the trailing edge of the plate. The boundary layer is assumed to begin at the leading edge of the plate. With these assumptions the displacement thickness given by White for turbulent flow [60] is used

$$\delta^* \approx \frac{0.16a}{8Re_a^{1/7}} \tag{3.12}$$

where Re_a is the Reynolds number.

3.2.2 Power Spectra of the Generalized Force

In order to incorporate the wall pressure power spectra into the model of the force on the plate, the generalized force spectral density for the rth mode (Q_r) must be found. A similar derivation to that used by Eringen [24] and Richards and Mead [61] is used. The second order differential modal equation (Equation 3.5) is solved using the Fourier transform pair given by

$$X(f) = \frac{1}{2\pi} \int_{-\infty}^{\infty} x(t) e^{-j\omega t} dt \tag{3.13}$$

and

$$x(t) = \int_{-\infty}^{\infty} X(f) e^{j\omega t} d\omega. \tag{3.14}$$

The Fourier transform of each η_r is expressed as a function of the Fourier transform of the rth generalized modal force (Q_r). The result is substituted into Equation (3.3) to give the Fourier transform of the normal displacement of the plate as

$$U(\bar{x}, \omega) = \sum_{r=1}^{\infty} \frac{Q_r(\bar{x}, \omega) \Psi_r(\bar{x})}{Z_r(\omega)} \tag{3.15}$$

where

$$Z_r(\omega) = \omega_r^2 - \omega^2 + i2\zeta\omega\omega_r \tag{3.16}$$

and $\bar{x} = (x, y)$. Using the definition of the power spectral density

$$S_{xx} = \lim_{t_o \to \infty} \frac{\pi}{t_o} X^*(\omega) X(\omega) \tag{3.17}$$

where $*$ represents the complex conjugate operator, the power spectral density of the displacement is written as

$$S_{uu} = \lim_{t_o \to \infty} \frac{\pi}{t_o} \sum_{r=1}^{\infty} \frac{Q_r^*(\bar{x}, \omega) \Psi_r(\bar{x})}{Z_r^*(\omega)} \sum_{s=1}^{\infty} \frac{Q_s(\bar{x}, \omega) \Psi_s(\bar{x})}{Z_s(\omega)}. \tag{3.18}$$

Expanding Equation (3.18) gives

$$S_{uu} = \sum_{r=1}^{\infty} \frac{\Psi_r^2(\bar{x})}{|Z_r(\omega)|^2} S_{qq_r}(\bar{x}_1, \bar{x}_2\ \omega) + \sum_{r=1}^{\infty}\sum_{s=1}^{\infty} \frac{\Psi_r(\bar{x})\Psi_s(\bar{x})}{Z_r^*(\omega)Z_s(\omega)} S_{qq_{rs}}(\bar{x}_1, \bar{x}_2, \omega) \quad r \neq s \tag{3.19}$$

where S_{qq_r} is the power spectral density function of the generalized force for the rth mode and $S_{qq_{rs}}$ is the cross-spectral density between two different modes. The first series gives the sum of the individual modal spectra. The double series contains cross terms which correct for the correlations between the responses in different modes. For this investigation, the cross terms are neglected. Thomas and Nelson state that the cross terms are negligible when the main concern is the response at resonance and the system is of low modal density [50].

The derivation of the equation of the power spectral density of the generalized force of the rth mode is found by taking the Fourier transform of the rth modal generalized force Equation (3.6)

$$Q_r(\bar{x}, \omega) = \lim_{t_o \to \infty} \frac{1}{2\pi m} \int_{-t_o}^{t_o} \int_S \Psi(\bar{x})_J(\bar{x}, t) e^{-j\omega t} dS dt. \tag{3.20}$$

The power spectral density of the rth mode generalized force is

$$S_{qq_r} = \lim_{t_o \to \infty} \frac{1}{t_o} \frac{1}{4\pi m^2} \int_{S_2} \int_{S_1} \Psi_r(\bar{x}_1)\Psi_r(\bar{x}_2) \int_{-t_o}^{t_o} \int_{-t_o}^{t_o} f(\bar{x}_1, t_1) f(\bar{x}_2, t_2) e^{i\omega(t_1 - t_2)} dt_1 dt_2 dS_1 dS_2 \tag{3.21}$$

Making the change of variable $t_2 = t_1 + \tau$ and using the definition of the cross-correlation function

$$R_{ff}(\bar{x}_1, \bar{x}_2, \tau) = \lim_{t_o \to \infty} \frac{1}{2t_o} \int_{-t_o}^{t_o} f(\bar{x}_1, t_1) f(\bar{x}_2, t_1 + \tau) dt_1 \tag{3.22}$$

and the cross-spectral density

$$S_{ff}(\bar{x}_1, \bar{x}_2, t) = \frac{1}{2\pi} \int_{-\infty}^{\infty} R_{ff}(\bar{x}_1, \bar{x}_2, \tau) e^{-i\omega\tau} d\tau \tag{3.23}$$

allows the power spectral density of the rth modal generalized force to be written as

$$S_{qq_r}(\omega) = \frac{1}{m^2} \int_{S_2} \int_{S_1} \Psi_r(\bar{x}_1) \Psi_r(\bar{x}_2) S_{ff}(\bar{x}_1, \bar{x}_2, \omega) dS_1 dS_2 \tag{3.24}$$

Since the flow field is assumed to be stationary and homogeneous,

$$S_{ff}(\bar{x}_1, \bar{x}_2, \omega) = S_{ff}(\xi, \eta, \omega) \tag{3.25}$$

when $\xi = x_2 - x_1$ and $\eta = y_2 - y_1$. By utilizing the Corcus model (Equation 2.1), the empirically fit exponential decays suggested by Strawderman (Equation 3.9), and the power spectral density of the pressure field given by Skudrzyk and Haddle (Equation 3.10), the cross-spectral density in (Equation 3.24) is integrated giving

$$S_{qq_r}(\omega) = \frac{4S_{pp}(\omega)}{abm^2} A(B1 + B2 + B3 + B4) \tag{3.26}$$

where

$$A = \frac{\frac{\gamma_3 \omega b}{U_c}}{[(\frac{\gamma_3 \omega}{U_c})^2 + (\frac{q\pi}{b})^2]} + \frac{2(\frac{q\pi}{b})^2 (1 - \cos(q\pi) \exp^{(\frac{-\gamma_3 \omega b}{U_c})})}{[(\frac{\gamma_3 \omega}{U_c})^2 + (\frac{q\pi}{b})^2]^2},$$

$$B1 = \frac{\frac{\omega a(\gamma_1 + i)}{2U_c}}{(\frac{\omega(\gamma_1 + i)}{U_c})^2 + (\frac{p\pi}{a})^2},$$

$$B2 = \frac{\frac{\omega a(\gamma_1 - i)}{2U_c}}{(\frac{\omega(\gamma_1 - i)}{U_c})^2 + (\frac{p\pi}{a})^2},$$

$$B3 = \frac{(\frac{p\pi}{a})^2 (1 - \cos(p\pi) \exp^{(\frac{-\omega a(\gamma_1 + i)}{U_c})})}{[(\frac{\omega(\gamma_1 + i)}{U_c})^2 + (\frac{p\pi}{a})^2]^2},$$

and

$$B4 = \frac{(\frac{p\pi}{a})^2 (1 - \cos(p\pi) \exp^{(\frac{-\omega a(\gamma_1 - i)}{U_c})})}{[(\frac{\omega(\gamma_1 - i)}{U_c})^2 + (\frac{p\pi}{a})^2]^2}.$$

3.2.3 Spectral Factorization

To determine a state space representation of the turbulent flow excitation, transfer functions between the assumed white noise input and the generalized forces must be found from the power spectra of the generalized forces derived in Equation (3.26). The transfer functions are found using a spectral factorization of the power spectra (Thomas and Nelson [50]). A transfer function having ten numerator and denominator coefficients is fit to the frequency information of the power spectra using a least squares procedure. A least squares fitting routine for a Z domain transfer function given by Parks and Burrus has been adapted for the S domain transfer function fit [62]. The equations for the least squares fit are developed using

$$C_{act}(\omega) \approx C_{fit}(s)|_{s=j\omega} \tag{3.27}$$

where C_{act} is the actual transfer function and C_{fit} is the transfer function to be fit. Using an IIR filter for C_{fit}, Equation 3.27 can be written as

$$C_{act}(f) \approx \left. \frac{b_0 + b_1 s^1 + \cdots + b_{n_b} s^{n_b}}{1 + a_1 s^1 + a_2 s^2 + \cdots + a_{n_a} s^{n_a}} \right|_{s=i\omega}. \tag{3.28}$$

Using Equation (3.28), an equation can be written for each of the N frequencies. These equations can be put into matrix form as

$$\{y\} = [X]\{\Theta\} + \{e\} \tag{3.29}$$

where

$$\{y\} = \{C_{act}(\omega_1), C_{act}(\omega_2), \cdots, C_{act}(\omega_N)\}^T$$

$$[X] = [[X_a] \;\; [X_b]]$$

$$[X_a] = \begin{bmatrix} -C_{act}(\omega_1)(i\omega_1)^1 & -C_{act}(\omega_1)(i\omega_1)^2 & \cdots & -C_{act}(i\omega_1)^{n_a} \\ -C_{act}(\omega_2)(i\omega_2)^1 & -C_{act}(\omega_2)(i\omega_2)^2 & \cdots & -C_{act}(i\omega_2)^{n_a} \\ & & \vdots & \\ -C_{act}(\omega_N)(i\omega_N)^1 & -C_{act}(\omega_N)(i\omega_N)^2 & \cdots & -C_{act}(i\omega_N)^{n_a} \end{bmatrix}$$

$$[X_b] = \begin{bmatrix} 1 & (i\omega_1)^1 & (i\omega_1)^2 & \cdots & (i\omega_1)^{n_b} \\ 1 & (i\omega_2)^1 & (i\omega_2)^2 & \cdots & (i\omega_2)^{n_b} \\ & & & \vdots & \\ 1 & (i\omega_N)^1 & (i\omega_N)^2 & \cdots & (i\omega_N)^{n_b} \end{bmatrix}$$

$$\{\Theta\} = \{a_1, \cdots, a_{n_a}, b_0, \cdots, b_{n_b}\}^T$$

$$\{e\} = \{e(f_1), e(f_2), \cdots, e(f_N)\}^T. \tag{3.30}$$

The error (e) is the difference between the actual frequency response and the fitted frequency response. The error is minimized using a complex version of a least squares minimization routine [62].

Since the power spectra is real, even, and positive, the odd ordered terms of the fitted transfer function are zero. Furthermore, the transfer function poles and zeros are symmetric about the real and imaginary ($j\omega$) axes. Thus, the modal excitation filter is obtained by taking the left half plane poles and zeros of the fitted transfer function. In this way, a transfer function of fifth order is sufficient to model each generalized force. Finally, the modal excitation filter is converted from a transfer function representation to an observable canonical state space representation. A total of 250 states were used to describe the 50 modal excitation filters. The input to the modal excitation filters is normally distributed broadband noise.

The power spectra calculated from Equation (3.24) for the first mode is shown in Figure 3.2 as a solid line. The power spectra given by the spectral decomposition is shown as the dashed line in Figure 3.2. The fit is within two dB over the frequency range from 10 to 10000 rad/s. As a result of the limited number of coefficients, more complicated excitation filters were not as accurately fit. For example, the fit for the fourteenth mode is shown in Figure 3.3. Although the exact dynamics associated with the 14th mode were not captured with the spectral decomposition, the general

shape was. The spectral decomposition process resulted in transfer functions that fit the 50 modal excitation filters within 5 dB over the frequency range of 10 to 10000 rad/s.

3.3 Sound Pressure Model

The third part of the analytical model is used to predict the sound pressure level at a specified location resulting from the panel excitation. This is accomplished using the Rayleigh integral

$$p(\{R\},t) = \frac{j\omega\rho_o}{2\pi} e^{j\omega t} \int_S \frac{\dot{u}(\{r_s\}) e^{jk(|\{R\}-\{r_s\}|)}}{(|\{R\}-\{r_s\}|)} dS \tag{3.31}$$

where ρ_o is the density of air, k is the acoustic wavenumber, $\dot{u}$ is the normal velocity of the plate, $\{r_s(x,y)\}$ is the position vector to the surface element, and $\{R(R,\phi,\theta)\}$ is the position vector to the control point. A spherical coordinate system with the origin at the center of the plate is used. The coordinate system is shown in Figure 3.4. By assuming that $(|\{R\}-\{r_s\}|) \gg a, b$ the approximation

$$(|\{R\}-\{r_s\}|) \simeq R - x\sin\theta\cos\phi - y\sin\theta\sin\phi \tag{3.32}$$

can be made. For a simply supported plate, the normal velocity due to the rth mode can be written in terms of the modal acceleration as

$$\dot{u}_r = \frac{\ddot{\eta}_r}{j\omega} \frac{2}{(ab)^{1/2}} \sin(\frac{p\pi x}{a}) \sin(\frac{q\pi y}{b}). \tag{3.33}$$

By utilizing the approximation given in Equation 3 32 and by substituting Equation (3.33) into Equation (3.31) and integrating, the frequency response $G_r(\omega)$ for the component of the Rayleigh integral associated with each modal acceleration is

$$G_r(\omega) = \frac{\rho_o(ab)^{1/2}e^{-jkR}}{\pi^3 pqR} \left[\frac{(-1)^q e^{j\beta}-1}{(\beta/q\pi)^2-1}\right] \left[\frac{(-1)^p e^{j\alpha}-1}{(\alpha/p\pi)^2-1}\right] e^{-j\beta/2} e^{-j\alpha/2} \tag{3.34}$$

where

$$\alpha = ka \sin\theta \cos\phi$$

$$\beta = kb \sin\theta \sin\phi.$$

The sound pressure level at the location (R, ϕ, θ) is calculated by using a modal summation of all $G_r(\omega)\dot{\eta}_r(\omega)$.

3.4 Experimental Configuration

An experimental setup was devised to investigate the problem of flow induced structural radiation of sound. The experimental apparatus was configured to approximate the assumptions used in the analytic model. The apparatus consisted of a rectangular panel which was flush mounted in the floor of a quiet flow wind tunnel facility test section. Sound radiated from the panel into an acoustically treated enclosure below the panel. The sound pressure at various microphone locations was compared to that predicted using the analytical model.

In order to use the analytical model for the structural excitation of the plate, simply supported boundary conditions were necessary. However, the analytical model for turbulent flow excitation assumes a boundary layer over a flush mounted plate. Therefore, the apparatus used to support the panel could not interfere with the turbulent flow field. One such design has been suggested by investigators at the University of Sherbrooke [63]. In their work, they approximated simply supported boundary conditions by attaching a plate to the top edge of an L channel beam with small bolts screwed into the sides of the plate. By utilizing bolt sizes that are small compared to the thickness of the panel and by machining the edge of the L channel to 1.5 mm, reasonable results were achieved. However, this design required extensive construction time, is unworkable for thin panels, and does not achieve continuous boundary conditions.

The plate boundary design utilized in this work is approximately simply supported, does not interfere with the turbulent boundary layer, and overcomes the drawbacks of the Sherbrooke design. The panel was a rectangular $46 \times 33 \times 0.48$ *cm* ($18'' \times 13'' \times 3/16''$) 6061 aluminum plate. The boundary condition design is uniform on all four sides of the plate and is shown in Figure 3.5. The 4.8 *mm* (3/16") thick 6061 aluminum plate is connected to a sub-frame via four 1.6 *mm* (1/16") thick aluminum strips. Both the plate and sub-frame were dadoed with high tolerances to tightly host the aluminum strip. The sub-frame was designed such that a 1.6 *mm* (1/16") gap separated the plate from the sub-frame on all sides. To minimize the moment applied to the plate, the thickness of the aluminum strips in the gap area was milled to less than one millimeter.

The sub-frame described above was fastened to a massive frame every 5 *cm* using small countersunk machine screws. The frame was constructed from 7.6×3.8 *cm* ($1.5'' \times 3''$) steel bar stock and provided rigid support of the sub-frame. The complete plate assembly is shown in Figure 3.6.

The assembly, which weighs approximately 45 Kg (100 lbs), was then attached to an acoustically treated wooden enclosure. The enclosure provided additional mass, isolated the plate from the wind tunnel test section structure, and isolated the sound radiated from the panel. The wooden enclosure was constructed using sand filled double plywood walls. The walls were covered with acoustic wedges. A hole matching the plate dimensions was cut in the top of the enclosure to allow sound from the plate to radiate into the enclosure interior. The enclosure was isolated from the test section structure of the wind tunnel. A schematic of the complete enclosure assembly is shown in Figure 3.7.

The assembly, with the longer plate dimension oriented in the streamwise direction, was flush mounted by extending the sub-frame through a hole in the bottom wall of the wind tunnel test section. The air gap between the sub-frame and the floor

of the wind tunnel was covered using Nashua metallic tape. A schematic of the orientation of the plate assembly in the test section is shown in Figure 3.8. A photograph depicting the flush mounted plate and the test section is shown in Figure 3.9.

The Herrick Laboratories low-noise wind tunnel facility has been designed to reduce the amount of noise generated from the operation of the wind tunnel [64]. A special anechoic diffuser and muffler have been included for this purpose. A drawing of the wind tunnel facility is shown in Figure 3.10. The wind tunnel is capable of achieving flow speeds of up to 51 m/s (115 MPH) in the test section.

3.5 Comparison of Analytical Model to Experimental Results

The experimental configuration was used to test the validity of the analytical model. The plate dynamics, structural excitation, and sound radiation portions of the model were investigated.

The analytic plate dynamics were compared to the measured system. A B&K 10 N Type 4810 mini-shaker was co-located with a Kistler 5130 accelerometer. The shaker and accelerometer were mounted in the center of the plate. For this reason, only the odd-odd modes could be sensed or actuated. The transfer function between the input voltage of the shaker and the accelerometer was measured. Since the input force was not measured, it was assumed that the impedance of the plate only consists of the mass of the plate. With this assumption, the approximate transfer function from input force to acceleration was calculated. This transfer function is compared to that for the analytical model and is shown in Figure 3.11. The natural frequencies of the first and fourth mode are close to those calculated by the model. However, the natural frequency of the eighth mode was measured to be approximately 900 Hz while the model predicts it to be 956 Hz. The decrease in the natural frequency is most likely a result of the additional mass associated with the accelerometer and shaker assembly. In addition to lower natural frequencies, the phase of the measured system

decreases with frequency. This characteristic is a result of the delay in the shaker and accelerometer system. As the delay was not included in the analytic model, this characteristic was not predicted.

A microphone was located in the enclosure to compare the sound pressure predictions. The microphone was located at R=36.6 cm, $\phi = 159.4°$, and $\theta = 17.3°$. The predicted and measured sound pressure level for a flow of 35.8 m/s (80 MPH) is shown in Figure 3.12. The most significant sound pressure levels for both the predicted and measured cases occur at the frequencies associated with the modes of the plate. However, there are significant differences in the spectra.

In order to determine the amount of background noise in the sound pressure level measurements, the noise radiated from the panel was blocked. This was accomplished by applying two layers of fiberglass and a piece of plywood to the opening in the top of the enclosure. With this configuration the amount of noise entering the enclosure by paths other than through the panel could be evaluated.

The sound pressure level for the 35.8 m/s (80 MPH) flow case is compared to no flow and to 35.8 m/s (80 MPH) flow where the sound radiation from the panel is blocked in Figure 3.13. Except at the frequency of the first mode (150 Hz), the sound pressure level for the blocked flow is as large as for the unblocked flow for frequencies below 400 Hz. Both the blocked and unblocked cases have sound pressure levels 15 dB higher than the zero flow case. Thus, the noise associated with the operation of the wind tunnel is very significant at low frequencies. A similar conclusion is made for the frequency range near 775 Hz. Since the sound radiated at the first mode is only 5 dB greater than for the blocked case, the noise in the low frequencies is a significant problem.

The sound radiation associated with the fourth mode (580 Hz) is significantly larger for the unblocked case than for the blocked or zero flow cases. Similarly, for frequencies above 700 Hz the sound pressure level for unblocked case is much larger than that for the blocked flow or the zero flow case. In these regions, the sound pressure level is primarily a result of radiation from the panel.

In order to improve the measurement quality, the sound radiated from the panel was increased. This was accomplished by adding a 2.54 cm high fence that extended laterally across the test section. The fence was located 11.4 cm before the leading edge of the panel (Figure 3.8). The fence increased the power spectrum of the pressure field which caused greater structural excitation of the panel. The wake flow created by this fence is complicated in nature. For this reason, there is not a good estimate for the displacement thickness or the power spectra of the wall pressure.

Fei Han [65] measured the wall pressure with and without the fence in place. The measurements were made using microphones flush mounted in an aluminum floor of the wind tunnel test section. The pressure for the case with the fence was found to be approximately ten times the pressure for the case with no fence. However, the pressure spectra measured with the fence in place was not as constant over the 100-1000 Hz region as was the spectra measured without a fence.

By assuming that the Skudrzyk and Haddle approximation is still applicable, a displacement thickness of 12.8 cm gives the correct value for the pressure power spectra. This value was used in the calculation of the turbulent excitation filters. Although the wall pressure spectra impacts the overall magnitude of the sound pressure level in the analytic model, it does not influence the shape of the sound pressure level spectra.

With the increased excitation level, the analytic model was compared to experimental results. As before, a microphone was used to measure sound pressure levels. The microphone was located at R=54.6 cm, $\phi = -40°$, and $\theta = 33°$. In addition, an accelerometer was located in the center of the plate and used to evaluate excitation levels. Since the accelerometer is located in the center of the plate, only the odd-odd modes can be sensed. Various flow velocities were tested.

The model of the acceleration at 35.8 m/s (80 MPH) is compared to the actual measurements in Figure 3.14. The comparison is within 5 dB up to a frequency of 700 Hz. However, the response near the eighth mode (960 Hz) is not accurately predicted. The model overpredicts the acceleration by approximately 10 dB in this region and

the sound radiation associated with the eighth resonance occurs at a frequency near 900 Hz.

The low acceleration magnitude predicted across the 700-900 Hz region was not measured. A potential source of error in this region is measurement noise. As illustrated in Figure 3.13, the operation of the wind tunnel adds significant noise to the measurements. An additional contribution to the noise floor is associated with the limited dynamic range of the analyzer. The noise floor has the potential to mask low plate acceleration magnitudes.

The predicted and measured sound pressure levels are shown in Figure 3.15. The general shapes of the spectra are similar. The model accurately predicts that the majority of the sound pressure level occurs at the modal resonances of the plate. The magnitudes of the sound pressure level at the frequencies of the first, second, fourth, and eighth modes are predicted within 5 dB of the measured values. However, the sound pressure levels predicted near the frequencies of the third and fifth modes are overpredicted by approximately 10 dB. Furthermore, the sound pressure level is underpredicted at frequencies not associated with the modal resonances. The measurement noise floor is a potential reason for underpredicting the sound at these frequencies.

The predicted and measured sound pressure levels associated with flow velocities of 26.8 m/s and 40.2 m/s (60 and 90 MPH) are shown in Figures 3.16 and 3.17 respectively. As predicted using the analytical model, the overall sound pressure levels increased with an increase in flow velocity. The predicted results were similar to those of the 35.8 m/s (80 MPH) case in that the most accurate sound pressure level prediction occurred near the natural frequencies of the plate and the sound pressure levels at frequencies not associated with modal resonances were underpredicted

3.6 Conclusions

The development of an analytical model for the structural radiation of sound due to a turbulent boundary layer excitation has been presented in this chapter. The structural response, turbulent flow excitation, and sound radiation have each been developed separately. The model was based on a 50 mode approximation. This analytical model will be utilized in the development and analysis of robust feedback control.

Although the model provides a useful estimate of the sound pressure, many approximations have been made in the analytical model which have resulted in errors in the sound pressure level predictions. The flow was assumed to have no pressure gradient, to be stationary and homogeneous, and to have a constant momentum thickness over the plate. These assumptions are unrealistic for flow in a test section. Furthermore, the cross-modal excitation terms have been neglected resulting in inaccurate predictions of the response at off resonant frequencies. There are also inaccuracies associated with the spectral factorization of the modal turbulent flow power spectra. Additionally, the vibration of the panel is not assumed to effect the turbulent flow pressure field. Inaccuracies in the dynamic response of the plate include the additional mass and stiffness associated with the accelerometer and shaker assembly. There are also potential errors associated with the assumption of simply supported boundary conditions. Furthermore, the sound is assumed to radiate into a free field and there is assumed to be no loading of the plate due to the sound radiation. Finally, in all parts of the model, system delay has been neglected. The delay is highly important in the design and implementation of control systems.

An experiment has been devised to investigate the turbulent flow induced structural radiation of sound phenomena. The experimental results have been compared to those predicted by the analytical model. Despite the many simplifications of the analytical model, it is capable of predicting the general characteristics of the sound pressure level spectra for this problem. Most of the sound pressure levels associated

with the natural frequencies of the plate are accurately predicted. For this reason, the model is useful in the development and evaluation of various control methodologies.

While the model is acceptable for investigating the relative merits of various control methodologies, controllers designed using the model will not work as expected on the experimental apparatus. Thus, for model based control methodologies a system identification based on experimental measurements is required.

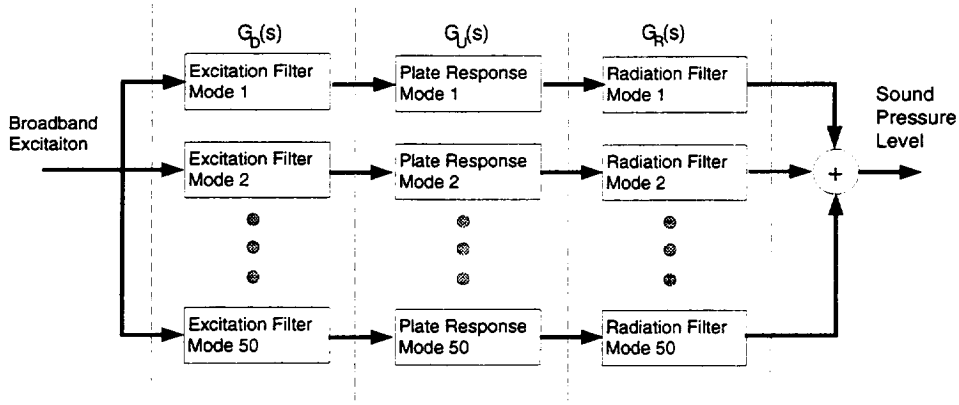

Figure 3.1 Block Diagram of Analytic Model

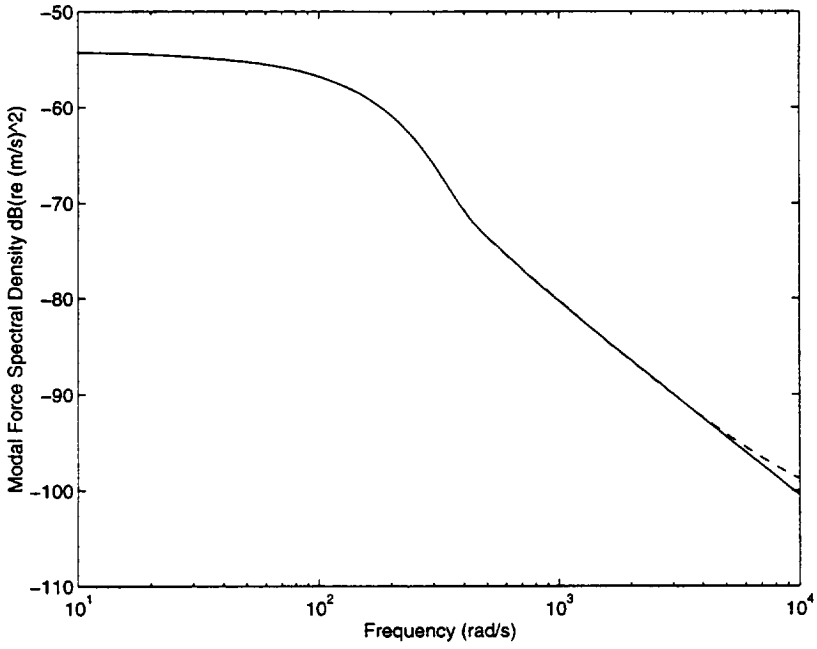

Figure 3.2 Spectral Decomposition For Mode One; Calculated —; Fit - -

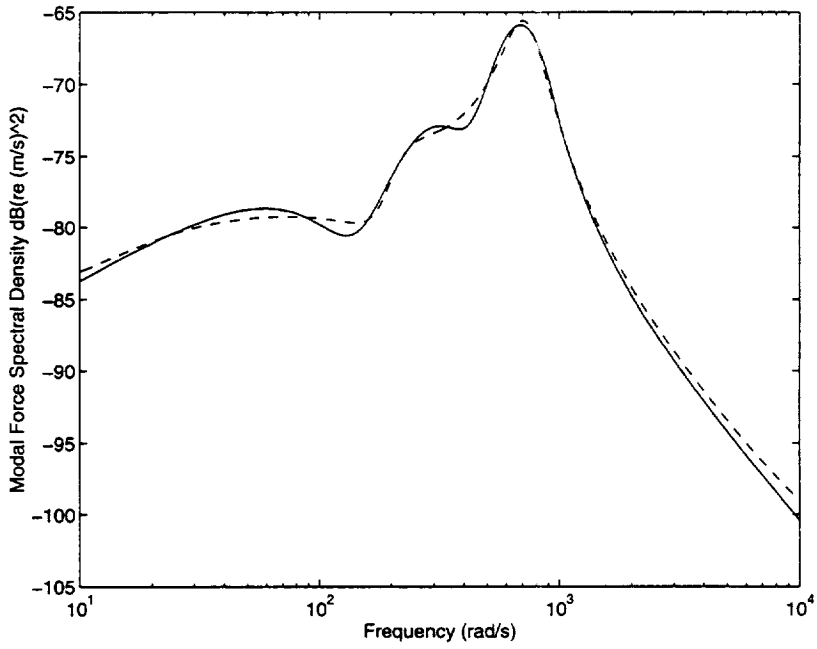

Figure 3.3 Spectral Decomposition For Mode Fourteen; Calculated —; Fit - -

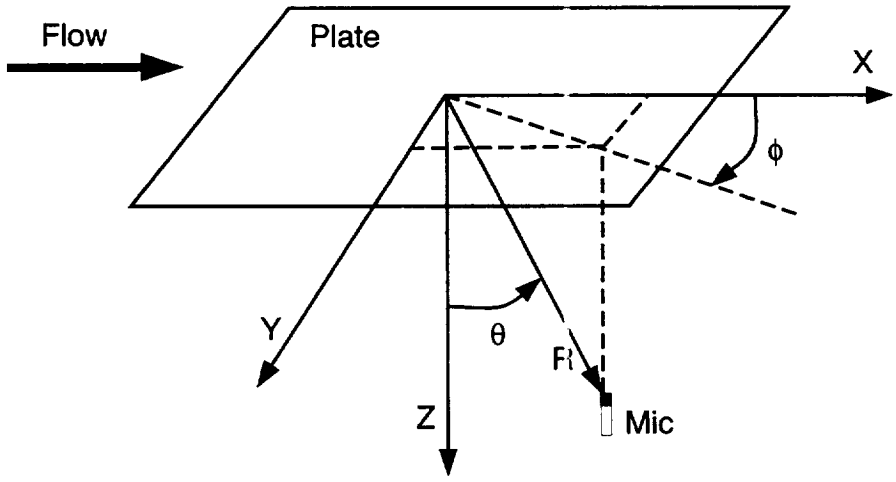

Figure 3.4 Spherical Coordinate Definition

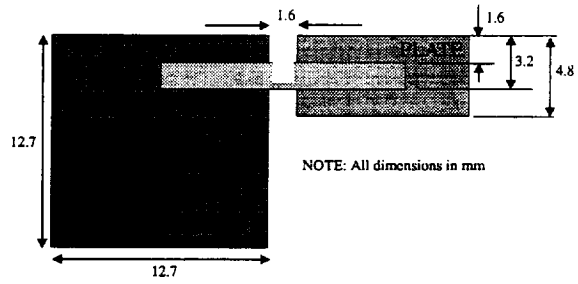

Figure 3.5 Cross-Section of Plate Support Assembly

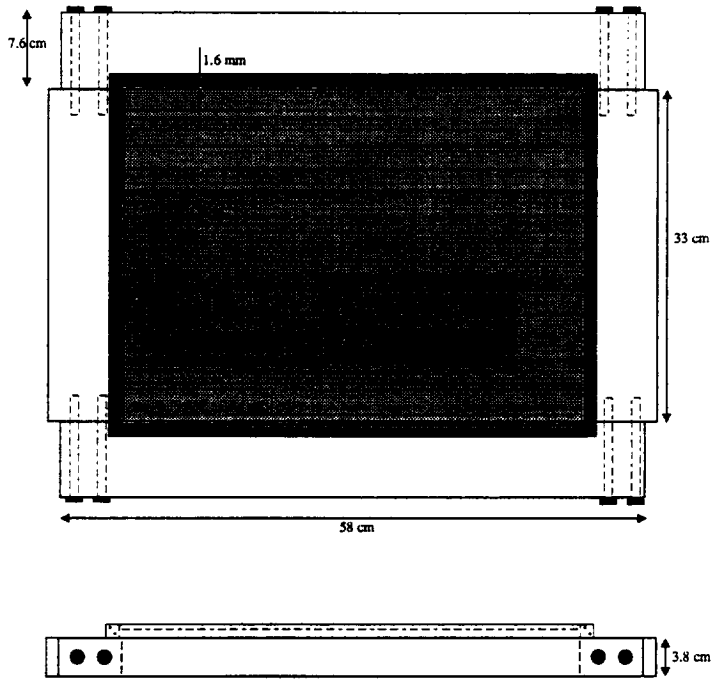

Figure 3.6 Plate Assembly Diagram

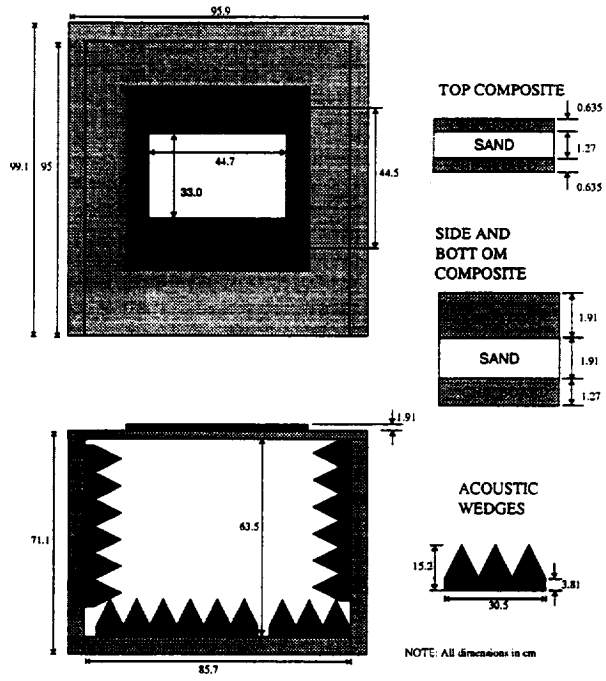

Figure 3.7 Acoustic Enclosure Assembly Diagram

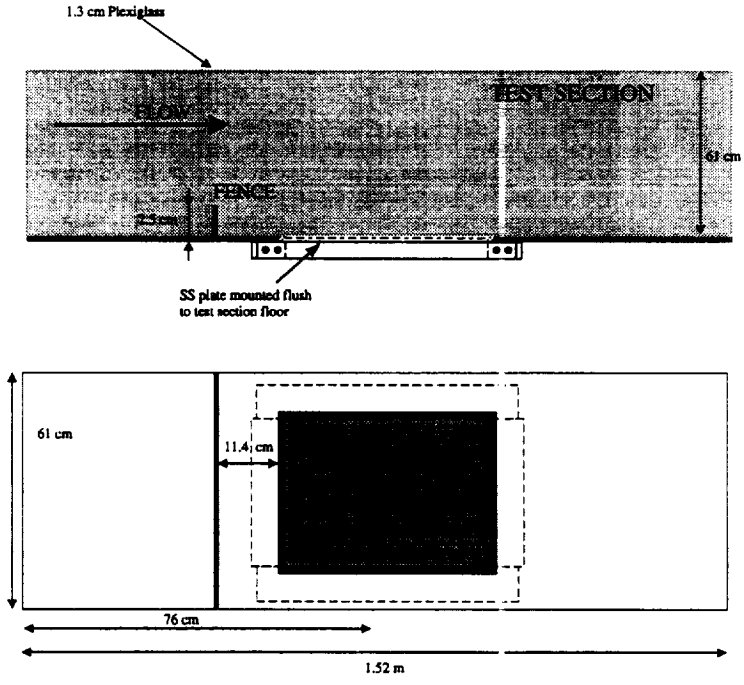

Figure 3.8 Schematic of Mounted Plate Assembly

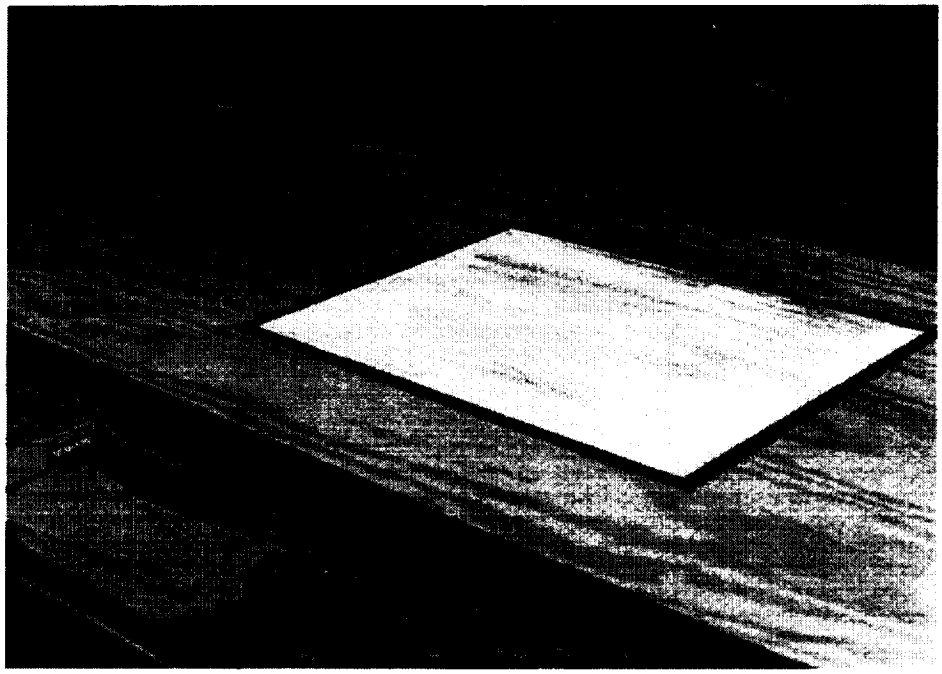

Figure 3.9 Photo of Mounted Plate

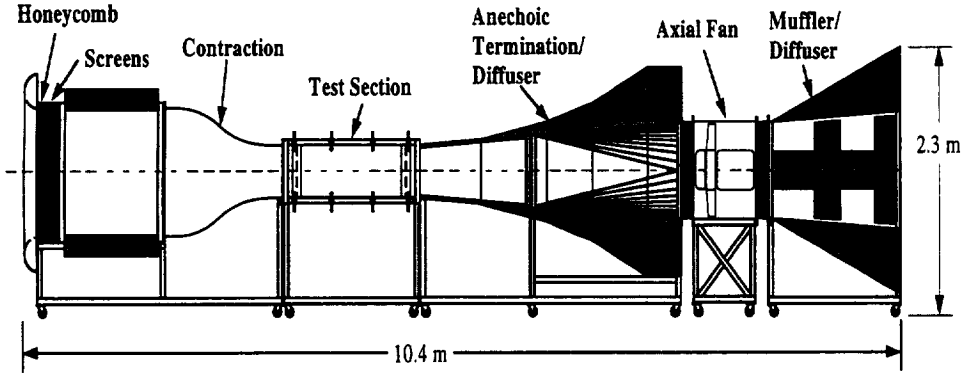

Figure 3.10 Herrick Laboratory Quiet Flow Facility

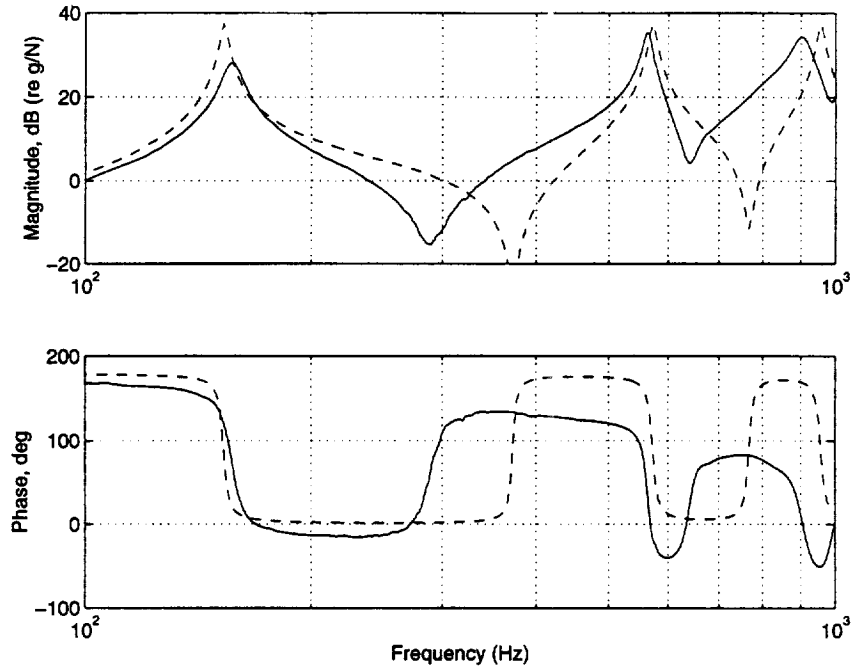

Figure 3.11 Plant Transfer Function Comparison; Measured —; Calculated - -

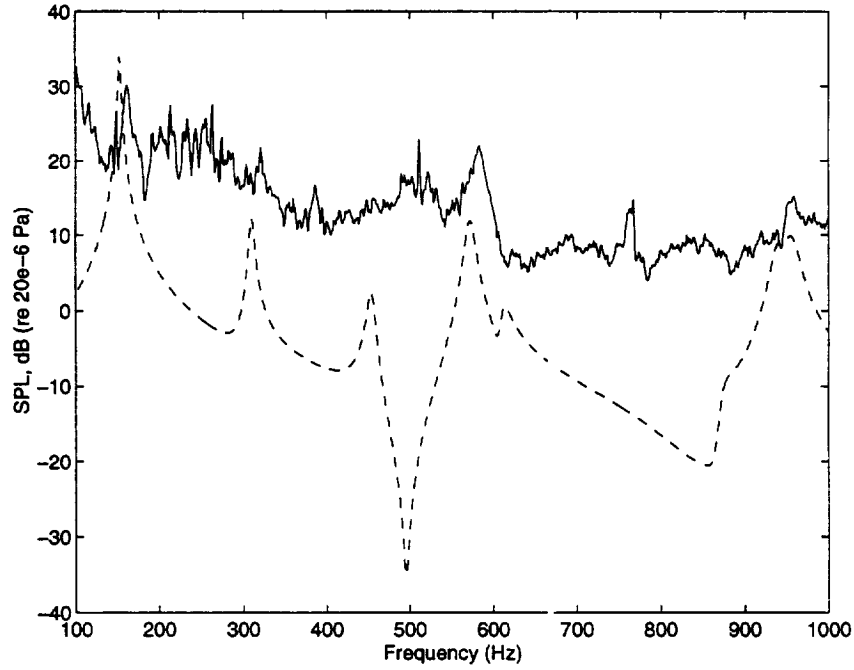

Figure 3.12 Measured and Predicted Sound Pressure Level With No Fence for Mic (36.6, 159.4°, 17.3°); Measured —; Calculated - -

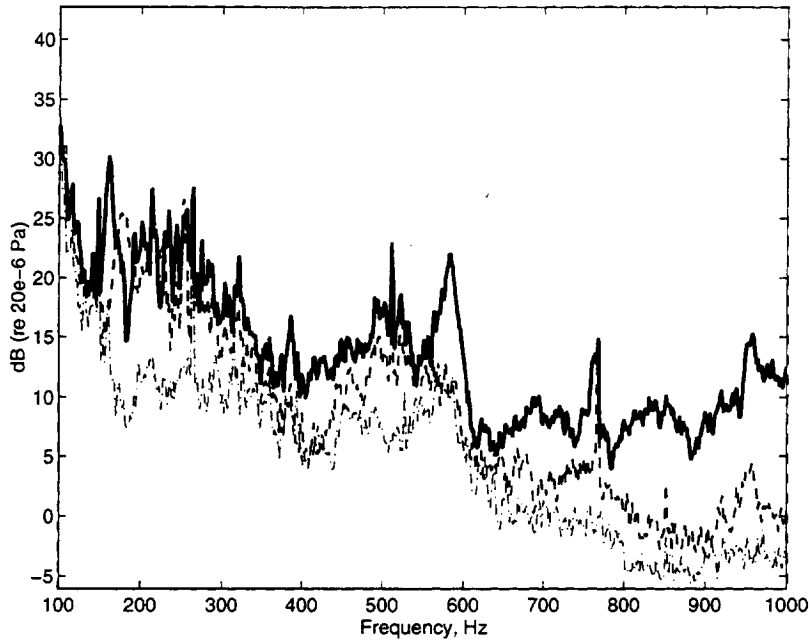

Figure 3.13 Measured Sound Pressure Level With No Fence for Mic $(36.6, 159.4^o, 17.3^o)$; 35.8 m/s —; Blocked 35.8 m/s - -; 0 m/s – ·

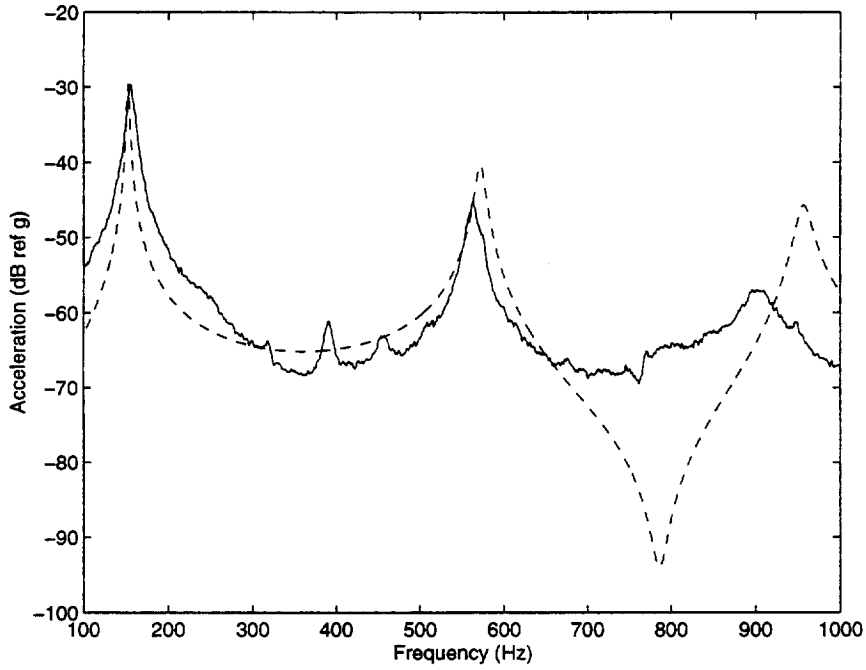

Figure 3.14 Measured and Predicted Acceleration with Fence (35.8 m/s); Measured —; Calculated - -

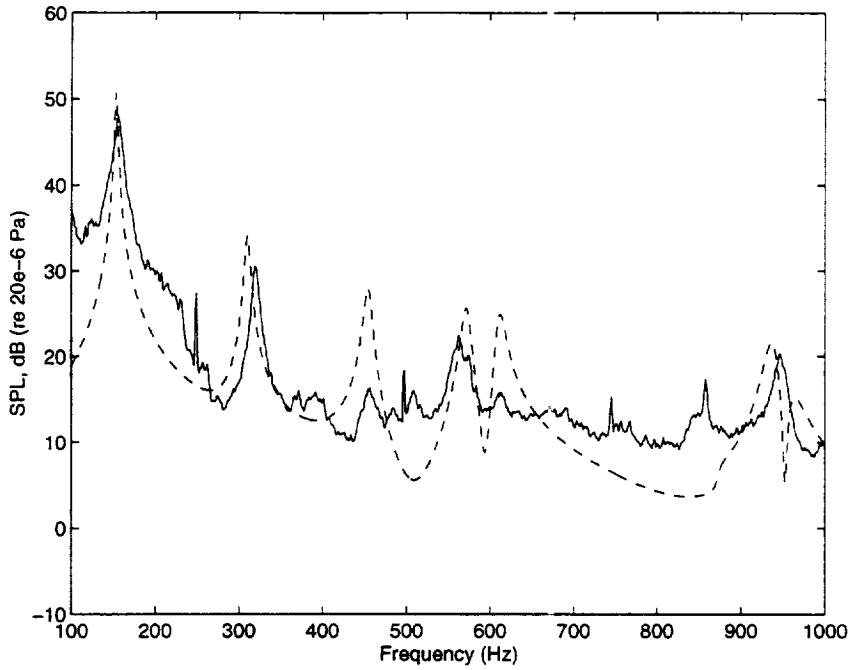

Figure 3.15 Measured and Predicted Sound Pressure Level With Fence for Microphone $(54.6, -40^o, 33^o)$ $(35.8\ m/s)$; Measured —; Calculated - -

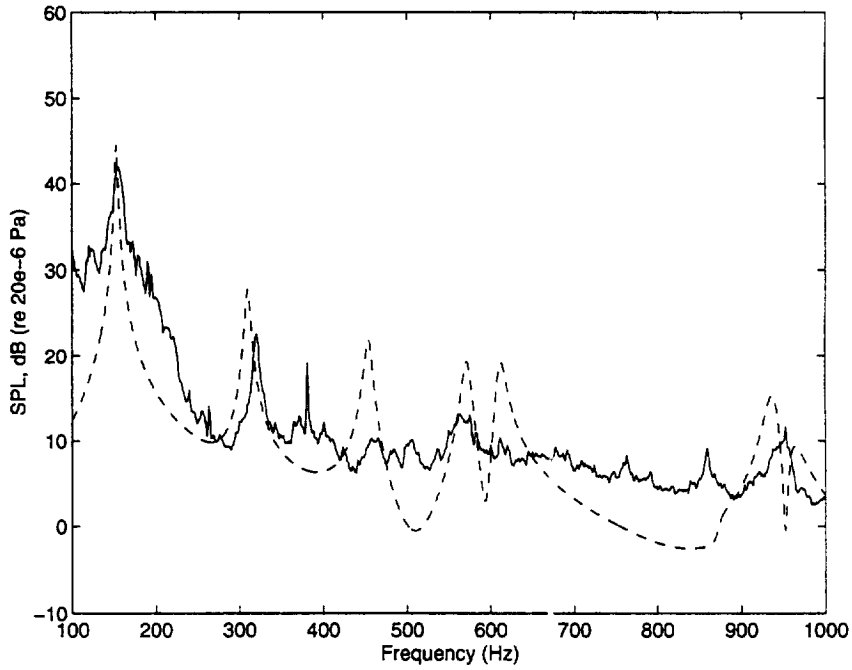

Figure 3.16 Measured and Predicted Sound Pressure Level With Fence for Microphone $(54.6, -40^o, 33^o)$ $(26.8\ m/s)$; Measured —; Calculated - -

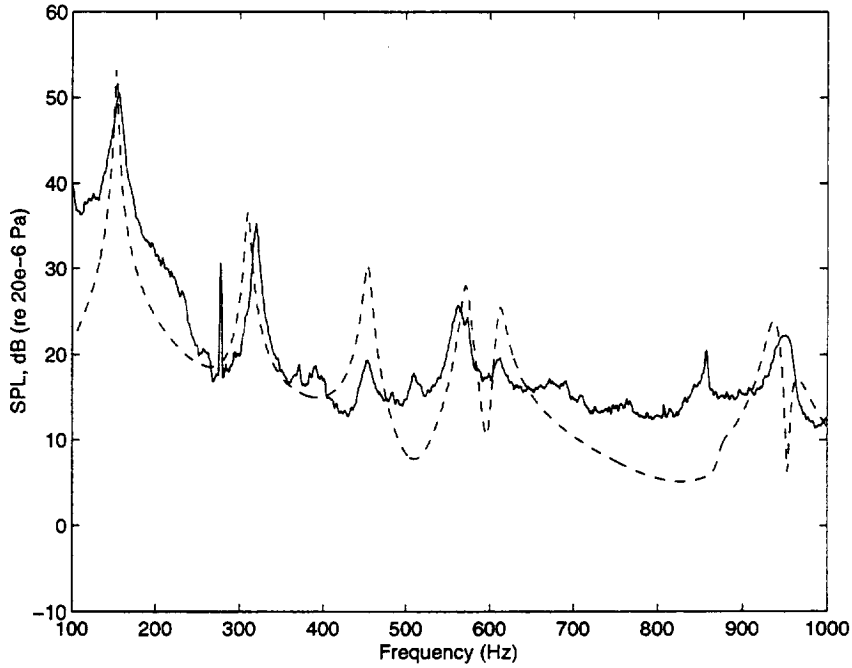

Figure 3.17 Measured and Predicted Sound Pressure Level With Fence for Microphone $(54.6, -40^o, 33^o)$ $(40.2\ m/s)$; Measured —; Calculated - -

CHAPTER 4. EVALUATION OF CONTROL METHODOLOGIES

In this chapter, various active control methods for the problem of flow induced structural radiation of sound are investigated. State space methods are described first. Next, μ synthesis controllers are evaluated using the analytical model developed in the previous chapter. Lastly, an adaptive feedback methodology is implemented in an experimental investigation. Relevant issues associated with these controller design methods are identified.

4.1 State Space Control

State feedback controllers require measurable states or an accurate model of the system. For the turbulent flow induced structural radiation of sound problem, the states associated with the turbulent flow excitation and structural sound radiation are non-physical. Therefore, an observer is required for state feedback control. As shown in Chapter 3, an accurate model of the turbulent flow excitation and structural sound radiation is not realistic. Although the general characteristics of the turbulent flow excitation can be modeled using a high order modal representation, the system cannot be described to the accuracy required to estimate states. Doyle has shown that errors in the model used to estimate unmeasurable states can result in arbitrarily small stability margins [34].

In addition to unobtainable states, there are generally difficulties associated with the truncation of measurable states. Although the states associated with the structural excitation are measurable, for practical reasons the number of states measured

must be finite. Thus, the structural model must be truncated. The truncation of the structural excitation states could reduce closed loop stability and performance.

The effects of delays cannot be incorporated in a state space model. Since delays are present in acoustic systems, this is a significant practical limitation of state space control. The delay associated with many sound radiation problems is the significant limiter of controller performance. This limitation cannot be accurately considered with state space controller design.

Nonlinearities, unmodeled modes, parameter changes, and other system uncertainties are not addressed in state space controller design. All physical systems include uncertainty and large uncertainty is expected for the turbulent flow induced structural radiation of sound problem. Since uncertainty is not included in the controller design, the controller is not robust. For these reasons full state feedback control is not often implementable or practical. Consequently, for this class of systems, state feedback control represents the best that active control can achieve but does not offer a practical solution.

4.2 μ Synthesis Controller Design

In this section robust controller design using the μ synthesis technique is investigated. The controllers were designed and evaluated based on the analytical model developed in Chapter 3.

4.2.1 System Configuration

The system to be controlled was a simply supported rectangular plate with a turbulent boundary layer excitation on one side. The plate was assumed to radiate sound into an anechoic environment and the fluid loading of the air was neglected. A

flow speed of 38 m/s (85 MPH) was considered. The plate and fluid parameters are shown in Table 4.1. A pictorial representation of the system is shown in Figure 4.1.

A single-input-single-output controller with a point force input was used. The feedback was acceleration co-located with the point force in the center of the plate. This location is such that it couples into the odd-odd modes of the plate. This is desirable since the odd-odd modes are the most efficient radiators of noise [66].

The feedback structure associated with the turbulent flow induced sound radiation problem is shown in Figure 4.2. $G_D(s)$ represents the modal excitation due to the turbulent boundary layer given by the spectral factorization of Equation (3.26), $G_U(\alpha, s)$ represents the dynamics of the plate, $G_R(s)$ represents the sound pressure radiation to the control point due to the modal excitation given by Equation (3.34), and $G_C(s)$ is the feedback controller. H and F are the modal participation coefficients associated with the sensor and actuator locations, respectively. The heavy lines indicate modal representations while the thin lines indicate measurable signals.

The system uncertainty was specified using both unstructured and parametric uncertainty. Unstructured uncertainty was used to represent the modeling errors associated with the truncation of modes. This uncertainty is the difference between the nominal system model containing eight modes and the fifty mode model assumed to be the actual system. This type of uncertainty accounts for errors in the system model rather than actual uncertainty that the system might exhibit. Parametric uncertainty was associated with variation in the natural frequencies and the damping ratio. As such, parametric uncertainty represents uncertainty associated with the actual system.

The performance goal was to reduce the sound pressure at a specified location to less than the desired sound pressure level, P_{des}, subject to a control effort limit, κ. However, the sound pressure level was not used as feedback since for most applications it would be impractical to locate microphones at the locations where sound pressure level reduction is desired. Furthermore, using the sound pressure level as the feedback signal would restrict the controller bandwidth, which in turn would limit closed loop

performance. This is a direct result of the phase lag associated with the delay of the sound propagation between the panel and the sensor location. As the distance between the sound pressure feedback sensor and the radiating surface increases, so does the amount of delay.

Although the sound pressure level was not used for feedback, it can be controlled indirectly when plate acceleration is used as feedback. Minimization of the plate acceleration at discrete points does not guarantee that the sound pressure level will be minimized. To effectively reduce sound radiation, the individual modal acceleration coefficients are weighted based on their sound pressure level contribution at the output location. Radiating modes are heavily weighted and non-radiating modes are lightly weighted. In this way, the structural response of the plate is controlled such that the residual plate vibration occurs only in modes which do not efficiently radiate sound.

4.2.2 μ Synthesis Controller Methodology

In this section a robust controller design using the μ synthesis technique is presented. Because a controller designed using μ synthesis is of the same order as the sum of the plant and disturbance models, it was impractical to use the model of the turbulent flow excitation containing 250 states. Instead, the disturbance was assumed to be broadband excitation from a point force. The point force is located at ($a/2.3$, $b/2.3$) such that all of the modeled modes of the plate are excited. Because the turbulent flow filters are smooth and contain few resonant peaks over the frequency range to be considered, the broadband point force excitation is similar to the broadband nature of the turbulent flow excitation. Thus, it was anticipated that the controller design based on a point force excitation will perform satisfactorily for the turbulent flow excitation.

To achieve sound pressure level reductions, the relative magnitudes of the radiation frequency responses ($|G_r|$) from Equation (3.34) were used to weight the accelerations

of each mode in the state space model. The weighting function for each closed loop modal acceleration is given by

$$\xi_r = \frac{\|G_r\|_\infty}{P_{des}} \tag{4.1}$$

where P_{des} is the desired sound pressure level. For this work, P_{des} was taken to be a constant across the frequency range of interest.

The control effort was specified as a performance objective by weighting the closed loop control effort transfer function. The control effort weighting is given by $\xi_c = 1/\kappa$ where κ is the maximum control effort transfer function magnitude. The weighted modal accelerations and control effort were collectively used to construct the overall performance goal given as

$$\left\| \begin{array}{c} \sum_r \xi_r T_r \\ \xi_c T_c \end{array} \right\|_\infty \leq 1 \tag{4.2}$$

where T_r is the closed loop transfer function associated with the rth modal acceleration and T_c is the closed loop transfer function for the control effort.

The parametric uncertainty matrices used to describe perturbations in the natural frequencies and damping ratio were obtained using the method outlined by Steinbunch *et al.* [67]. Steinbunch showed how structured complex perturbations for two parameters ($a = a_{nom} + s_a\delta_a$, $b = b_{nom} + s_b\delta_b$) for the equation

$$\dot{x} = a_{nom}b_{nom}x + (\gamma_1\delta_a + \gamma_2\delta_a\delta_b + \gamma_3\delta_b)x \tag{4.3}$$

can be formulated in state space form using additional uncertainty states. With his method, the variation in the natural frequencies and damping ratios were incorporated into the state space model. A triple complex repeated uncertainty and an additional complex uncertainty were used for each mode of the nominal model.

The unstructured uncertainty was obtained by bounding the difference between the actual system transfer function (50th order) and the nominal transfer function

(8th order). The magnitude of the unstructured uncertainty was bounded by the second order transfer function

$$\frac{1.5 \times 10^{-3} s^2}{(\frac{s}{4200} + 1)(\frac{s}{4200} + 1)}. \tag{4.4}$$

The bounding of the unstructured uncertainty using Equation (4.4) is shown in Figure 4.3.

Similar to the work of Fluder and Kashani [59], the problem was formulated in the general framework for an H_∞ or μ synthesis problem

$$\begin{Bmatrix} Y_1 \\ Y_2 \\ Y_3 \end{Bmatrix} = \begin{bmatrix} P_{11} & P_{12} & P_{13} \\ P_{21} & P_{22} & P_{23} \\ P_{31} & P_{32} & P_{33} \end{bmatrix} \begin{Bmatrix} U_1 \\ U_2 \\ U_3 \end{Bmatrix} \tag{4.5}$$

where U_1, U_2, U_3, Y_1, Y_2, and Y_3 are the uncertainty output, disturbance input, control input, uncertainty input, desired output, and measured output, respectively. U_1 and Y_1 are composed of eight triple complex repeated uncertainty blocks and eight single complex uncertainty blocks associated with the parametric uncertainty and an additional complex uncertainty block associated with the unstructured uncertainty. There is a single disturbance input (U_2), controller input (U_3), and measured output (Y_3). The desired output (Y_2) is composed of the first eight modal accelerations and the control effort. A block diagram representation is shown in Figure 4.4. In Figure 4.4, Δ is the 33 input-33 output uncertainty matrix, P is the 35 input-43 output model of the plant, disturbance, and uncertainty, and K is the SISO controller to be synthesized.

In this investigation, the μ synthesis problem is solved using the D-K iteration method proposed by Doyle [68, 69]. In the D-K iteration procedure, the minimization of

$$\|D\mathcal{F}_l(P, K)D^{-1}\|_\infty \leq 1 \tag{4.6}$$

is solved iteratively for either K or D while holding the other constant. For a fixed D, the problem is an H_∞ optimization problem, while for a fixed K, the problem is

a convex optimization problem at each frequency. The convex optimization problem is expressed as

$$\min_{D_\omega} \bar{\sigma}[D_\omega \mathcal{F}_l(P,K) D_\omega^{-1}]. \tag{4.7}$$

The solution to the convex optimization problem gives an optimal frequency dependent scaling matrix (D_ω) which corresponds to the system perturbation matrix Δ. The magnitude of the optimal matrix (D_ω) is fit with a stable, minimum-phase transfer function (D). For D chosen to be a constant no additional states are added to P and subsequently to the controller K. However, for a better approximation of the μ solution, dynamics can be used in D. The order of the controller will increase by the number of states associated with these dynamics. Although the D-K iteration procedure works well on many engineering problems, it is not guaranteed to converge to a global minimum.

The controlled system can be represented as

$$\begin{Bmatrix} Y_1 \\ Y_2 \end{Bmatrix} = \begin{bmatrix} Q_{11} & Q_{12} \\ Q_{21} & Q_{22} \end{bmatrix} \begin{Bmatrix} U_1 \\ U_2 \end{Bmatrix}. \tag{4.8}$$

This representation is depicted in Figure 4.5 where Δ is the system uncertainty and Q is the linear fractional transformation of the controller and the plant given by

$$Q = \mathcal{F}_l(P,K) = P_{21} + P_{22}K(I - P_{32}K)^{-1}P_{31}. \tag{4.9}$$

The maximum Structured Singular Values (SSV) of Q provide information on the controlled system performance and stability. For each D-K iteration, the SSV more closely approximates $\mu(Q)$ where

$$\frac{1}{\mu(Q)} = min\{\bar{\sigma} : \Delta \in \mathbf{\Delta}, det(I - Q\Delta) = 0\}. \tag{4.10}$$

If $\mu(Q)$ does not exceed unity for any frequency, robust performance and stability are guaranteed [68, 69]. The SSV of Q_{11} is used to evaluate robust stability and

the SSV of Q_{22} is used to evaluate nominal performance. For this work, the Perron eigenvalues are used to estimate the SSV. These eigenvalues were shown to be a good upper bound on the SSV by Safonov [70].

4.2.3 Controller Design and Evaluation

Fluder and Kashani [59] reported difficulty in obtaining a controller which satisfied both robust performance and robust stability. Similar difficulties were encountered in this investigation. A μ synthesis controller was developed for the case where $\kappa = 10\ N$ and $P_{des} = 105\ dB$. The control effort constraint was chosen to be 10 times the RMS value of the disturbance force. The degree of parametric uncertainty was assumed to be one percent variation in the natural frequencies and five percent variation in the damping ratio. The SSV of Q for each of three D-K iterations are shown in Figure 4.6. For each iteration, the D matrix was fit using constants. Since each of the iterations has singular values which exceed unity, robust performance was not guaranteed. Additional iterations did not significantly improve the closed loop performance. Robust stability was not guaranteed since the SSV for Q_{11} for each of the three iterations shown in Figure 4.7 was greater than unity. Although robust stability was not guaranteed, nominal performance was. The SSV for Q_{22} for each of the three iterations is shown in Figure 4.8. Since the maximum SSV is less than unity, nominal performance was guaranteed.

In order to satisfy robust stability, another μ synthesis controller was designed for a reduced parametric uncertainty of 0.1 percent variation in the natural frequencies and 0.5 percent variation in the damping ratios. The control effort was restricted using $\kappa = 10N$. The desired sound pressure level was changed from $P_{des} = 105\ dB$ to $P_{des} = 100\ dB$. Thus, larger sound pressure level reductions are required. The SSV of Q for each three D-K iterations are shown in Figure 4.9. As before, the SSV for Q exceeded unity and therefore robust performance was not achieved. However, the

SSV for Q_{11} for each of the three iterations, as shown in Figure 4.10, was less than unity. Therefore, robust stability was achieved for the reduced degree of parametric uncertainty. The SSV for Q_{22} for each of the three iterations is greater than unity and is shown in Figure 4.11. Thus, the increased performance requirement was not satisfied for the nominal case.

A μ synthesis controller was developed for the reduced parametric uncertainty of 0.1 percent variation in the natural frequencies and 0.5 percent variation in the damping ratios and the sound pressure level performance requirement of $P_{des} = 105\ dB$. As before, the control effort was restricted by $\kappa = 10N$. The SSV for Q for each of the three iterations is less than unity and is shown in Figure 4.12. Therefore, robust performance and hence robust stability and nominal performance were guaranteed.

Since the controller order is contingent upon the number of states of P, the controller order is large (18 states). The Bode plot of the controller is shown in Figure 4.13. The maximum controller gain was approximately -75 dB. There are significant lightly damped controller dynamics in the 500-2000 rad/s frequency band.

The sound pressure level for the broadband point force disturbance input for the uncontrolled and the controlled system are shown in Figure 4.14. The sound pressure level was calculated as the sum of the sound pressure levels due to the individual modal accelerations. The full 50 mode model was used for both the controlled and uncontrolled responses. The sound radiation associated with the first mode was reduced by approximately 5 dB and that associated with the third mode was reduced by approximately 2 dB. The desired sound pressure level of 105 dB was achieved and there was no control spillover into higher modes. The closed loop frequency response of the control effort is shown in Figure 4.15. The response was less than the allowable limit of 10 N.

The sound pressure level at the control point was also calculated for the flow noise disturbance model. The performance was evaluated using the full 50 mode model. The uncontrolled and controlled sound pressure level responses are both shown in Figure 4.16. As with the point force disturbance, approximately 5 and 2 dB of sound

pressure level reductions were achieved at the first and third resonances, respectively. The time history of the acceleration at the sensor location is shown in Figure 4.17. The acceleration was only slightly attenuated as is indicated by the fact that the RMS value of the controlled acceleration is $4.1 \times 10^{-3} m/s^2$ while that of the uncontrolled acceleration is $4.4 \times 10^{-3} m/s^2$. The control effort is less than 0.6 μN and is shown in Figure 4.18.

The use of dynamic scaling in the D matrix was also investigated. The controller performance parameters were specified as $\kappa = 10N$, $P_{des} = 105\ dB$ with parametric uncertainty of 0.5 percent variation in the natural frequencies and 2.5 percent variation in the damping ratio. The SSV for Q for three iterations with no additional dynamics in D is shown in Figure 4.19. Robust performance is not guaranteed for this design. The sound pressure level for the turbulent flow disturbance is shown in Figure 4.20. Approximately 5 and 3 dB of sound pressure level reductions were achieved at the first and third modal resonance respectively.

The same parameters were used to design a controller where dynamics were included in the D scale. The approximation of the μ bound was most sensitive to the uncertainty associated with the unstructured uncertainty block. A second order transfer function was used to fit the portion of the D matrix associated with the unstructured uncertainty block. The other uncertainty blocks were fit with constant D scaling. This allowed for improved accuracy in the approximation of the μ bound. The resulting SSV for Q for three iterations is shown in Figure 4.21. Additional iterations did not improve the controller design. As shown in Figure 4.21, robust performance is not achieved. However, the additional dynamics in D did improve the controller design. The maximum SSV for the non-constant D weighting are less than those for the constant D weighting. Furthermore, the SSV has been changed from approximately 2 to approximately 0.8 in the 500 rad/s region.

The sound pressure level for the turbulent flow disturbance is shown in Figure 4.22. Approximately 8 and 5 dB of sound pressure level reductions were achieved at the first and third modal resonance respectively. The sound pressure level at the second

resonance frequency (312 Hz) was not controlled since the shaker and accelerometer were on a node line of this mode. The additional dynamics in D better approximate μ and thereby achieve improved system performance. However, the dynamic weighting increases the controller order.

It should be noted that the μ synthesis method was sensitive to changes in the performance objectives. For example, for a constant D matrix, $P_{des} = 72\ dB$, and $\kappa = 0.2N$, robust performance, nominal performance, and robust stability were not achieved. However, sound pressure level reductions are achieved. The controlled and uncontrolled sound pressure levels for the turbulent flow disturbance are shown in Figure 4.23. Approximately 18 dB of sound pressure level reduction is achieved at the first resonance. Additional reductions of approximately 2 and 4 dB are achieved at the third and eighth resonances respectively. Although the closed loop nominal performance is significant, the controller itself is unacceptable because a right half plane complex conjugate pole pair has been included in the controller. A Nichols chart of the open loop transfer function is shown in Figure 4.24. Note that the open loop transfer function makes a clockwise encirclement of the stability point (0 dB, -180 degrees). This corresponds to two counterclockwise encirclements of the stability point in a Nyquist plot. Thus, the Nyquist stability criteria is satisfied. The plant has been used to stabilize the controller. Although closed loop stability is achieved, a failure of the feedback sensor or a variation in the controller gain would result in an unstable system. The μ synthesis technique offers no *a priori* means of avoiding right half plane controller poles.

4.2.4 μ Synthesis Conclusions

The μ synthesis technique was successfully employed to design a robust controller for the flow induced structural radiation of sound problem. Sound pressure level reductions were approximately 5 dB at the first modal frequency for both the flow

and point force disturbance excitations. However, robust stability was not achieved except in the case of small parametric uncertainty. Furthermore, robust performance was not achieved except for small parametric uncertainty and reduced sound pressure level reduction requirements.

The impact of the performance criteria and uncertainty on the controller design is not clear during the μ synthesis controller design procedure. When robust stability is not achieved, it is not known whether the unstructured uncertainty or a particular modal parameter variation is responsible for the design failure. Likewise, when nominal performance is not satisfied it is unknown whether the control effort restriction is too severe or the desired sound pressure level is too small.

The μ synthesis controller is of the same order as the system model. For this reason, the large flow noise disturbance model was impractical and a more simplistic point source disturbance was used. Even if robust performance is achieved for a point force disturbance, it does not guarantee robust performance for the turbulent flow induced structural radiation of sound problem.

Another drawback of the μ synthesis techniques is that a model of the system is required. Appropriate uncertainty must be incorporated in the system to account for any inaccuracies in the model. This uncertainty is in addition to any uncertainty associated with actual changes in the system. This additional uncertainty reduces the controller performance.

4.3 Adaptive Feedback Controller Investigation

In this section, adaptive feedback control is considered. With an adaptive feedback controller, a reference transducer is not required. Therefore, it is possible to implement adaptive feedback control for the turbulent flow induced structural radiation of sound problem. Adaptive feedback control requires no *a priori* system information. An online system identification procedure is utilized to obtain a model of the plant

transfer function. Once a plant model has been obtained, a gradient based adaptive algorithm is utilized to adapt the controller dynamics.

4.3.1 Adaptive Feedback Controller Methodology

Adaptive feedback control is accomplished by configuring the feedback system such that a feedforward methodology can be used. Nelson and Thomas [46] have shown that if an accurate model of the plant transfer function is known, the controller can be configured such that adaptive feedforward algorithms can be used. This is accomplished by using the controller configuration shown in Figure 4.25. The controller is given by

$$G_C(s) = \frac{H(s)}{1 + H(s)\hat{G}_U(s)} \tag{4.11}$$

where $H(s)$ is the equivalent feedforward controller and $\hat{G}_U(s)$ is an estimate of the plant transfer function. With this controller, the closed loop transfer function between the disturbance and the system output is given as

$$\frac{Y}{D} = \frac{G_D(s)(1 + H(s)\hat{G}_U(s))}{1 + (\hat{G}_U(s) - G_U(\alpha, s))H(s)}. \tag{4.12}$$

With an accurate controller model of the plant ($\hat{G}_U(s) = G_U(\alpha, s)$), the closed loop transfer function is the same as for a feedforward system

$$\frac{Y}{D} = G_D(s)(1 + H(s)G_U(\alpha, s)). \tag{4.13}$$

By utilizing an accurate model of the plant transfer function in the controller, a feedback configuration is converted to a feedforward configuration for the control filter $H(s)$. In this way the controller $H(s)$ does not have to satisfy any stability criteria. Furthermore, standard feedforward adaptation algorithms such as the filtered-U algorithm can be used to adapt the controller filter $H(s)$.

The problem with utilizing this type of controller is that errors in the controller plant model can result in stability problems. The system stability is determined by the denominator of Equation 4.12. Thus, the function $\hat{L}(s) = (\hat{G}_U(s) - G_U(\alpha, s))H(s)$ must satisfy the Nyquist stability criteria. There is a possibility for instability when the magnitude of $\hat{L}$ is greater than one. Therefore, the plant transfer function model must be accurate at the frequencies where the controller gain $|H(s)|$ is large.

In order to explore the effect of plant model errors on the stability of the system, the single mode plant

$$G_U(s) = \frac{0.2(s/500 + 1)}{((s/1000)^2 + 2(0.02)s/1000 + 1)} \tag{4.14}$$

is considered. The plant is plotted as a heavy solid line on an extended Nichols chart in Figure 4.26. A unit gain controller ($H(s) = 1$) will achieve control and is considered in this example. The dashed line in Figure 4.26 is the Nichols plot of $\hat{L}(s)$ for an error in the frequency of the mode. The modeled plant is the same as the actual plant except that the resonance is at 995 Hz rather than 1000 Hz. The modeled plant is given by

$$\hat{G_U}(s) = \frac{0.2(s/500 + 1)}{((s/995)^2 + 2(0.02)s/995 + 1)}. \tag{4.15}$$

As shown in Figure 4.26, $\hat{L}(s)$ encircles the stability point at -180 degrees. This error in the plant model would cause the system to be unstable.

An error in the gain of the plant model is also investigated. The dashed dotted line in Figure 4.26 corresponds to $\hat{L}(s)$ for a gain error of 15 percent. As in the previous case, the stability point is encircled and the system is unstable.

4.3.2 Adaptive Feedback Controller Experimentation

Using the controller configuration of Figure 4.25, the adaptive feedback control approach was investigated experimentally for the turbulent flow induced structural radiation of sound problem. The experimental configuration described in Chapter 3 was utilized. A single-input-single-output controller consisting of a point force control

actuator and a microphone feedback sensor was used. The point force control actuator was located in the center of the plate. The microphone was located at R=54.6 cm, $\phi = -40°$, $\theta = 33°$. This location was 46 cm away from the plate. The delay associated with the sound radiation was approximately 1.3 ms.

The control was implemented on a Digisonix dX-100 adaptive digital filter system. This system incorporates A/D and D/A architecture with a TMS320C30 DSP processor. Various adaptive algorithms have been programmed for implementation on this system. For this investigation, the filtered-U algorithm [71] was utilized to update the IIR filter H. The filtered-U algorithm was also utilized in the online system identification of the plant $\hat{G}_U$. The number of numerator and denominator coefficients used in the controller was selectable for the experiment. Both the plant filter and the controller filter were configured with 30 numerator and 29 denominator coefficients. The sample rate of the controller was limited by the computation speed of the DSP chip to 5000 Hz. The anti-aliasing filters on the A/D were removed from the Digisonix hardware. The anti-aliasing was accomplished by adding a Wavetex Model 852 low-pass filter set at 2000 Hz to the plant.

Wind tunnel flow speeds of 26.9, 35.8, and 40.2 m/s (60, 80, and 90 MPH) were investigated. Gaussian noise was used to perform the on-line system identification of the plant transfer function. This system identification was performed for each wind tunnel speed prior to the adaptation of the controller filter. The identification process was continued until the plant filter coefficients stabilized. This identification process required several minutes.

For each of the flow speeds tested, the closed loop system became unstable. The instability is a direct result of the delay associated with microphone feedback. The delay associated with the time for the sound radiated from the structure to arrive at the microphone causes phase lag in the plant transfer function. This phase lag can not be accurately modeled using a discrete filter. Figure 4.27 shows the actual and modeled plant transfer function. Although the plant transfer function used 30 numerator and 29 denominator coefficients, an accurate model was not achieved. The

model contained many non-minimum phase zeros in an attempt to match the phase lag associated with the delay. However, phase differences on the order of 200 degrees occurred. Furthermore, the magnitude of the transfer function was not accurately matched.

Additional filter coefficients were included in the plant model in order to better model the plant. The case for 60 numerator coefficients and 59 denominator coefficients is shown in Figure 4.28. Although the additional coefficients improved the model, neither the phase nor the magnitude were accurately modeled. An additional configuration using a 120 coefficient FIR filter was tested. The comparison between the model and the actual plant transfer function is shown in Figure 4.29. As before, the phase was not accurately modeled. Furthermore, the lack of denominator coefficients results in a poor approximation of the actual transfer function magnitude. Without an accurate plant model, the feedback system was not equivalent to a feedforward configuration which resulted in the observed instability.

To reduce the delay, a microphone located closer to the plate was used as the feedback sensor. The new microphone location was R=13.3 cm, $\phi = 131^o$, $\theta = 62^o$. This location is 6 cm from the plate. At this distance the delay associated with sound radiation is approximately 0.19 ms. This delay is almost 1/7 of that for the previous microphone location. With the smaller delay, the plant model's accuracy was improved which allowed the adaptive algorithm to achieve control. Both the plant filter and the controller filter contained 30 numerator and 29 denominator coefficients. The controlled and uncontrolled sound pressure levels for 35.8 m/s (80 MPH) flow are shown in Figure 4.30. The only sound pressure level reduction is near the frequencies associated with the first resonance of the panel. Approximately 5 dB is removed from the sound associated with this resonance. The total sound pressure level reductions across the 100-1000 Hz band are 1.9 dB. Similar control was achieved at flow speeds of 26.9 and 40.2 m/s (60 and 90 MPH).

In order to eliminate the problems associated with the acoustic delay, experiments were performed using acceleration feedback. As before, the dX-100 system was used to

implement a single-input-single-output adaptive feedback controller. The accelerometer and control actuator were located at the center of the plate. At this location the sensor and actuator couple with the odd-odd modes of the plate. A microphone mounted inside the box (R=54.6 cm, $\phi = -40°$, $\theta = 33°$) was used to evaluate the controller performance but was not used as feedback.

By using acceleration feedback, the controller is trying to minimize vibration rather than sound pressure. With current adaptive feedback technology there is no weighting associated with the interaction between the structural vibration and the sound radiation. Therefore, there is no guarantee of sound pressure level reductions. Since most of the vibration occurs at the structural resonances of the problem, only sound at these frequencies will be controlled. Thus, if the acoustic field is strongly coupled to an off resonant structural excitation, little sound pressure level reductions could be achieved.

The plant identification procedure described previously was utilized to determine the plant filter coefficients. An estimate of the plant was obtained for each wind tunnel speed prior to the adaptation of the controller filter. As before, the plant transfer function was modeled using a 30 numerator, 29 denominator IIR digital filter. For accelerometer feedback, the plant transfer function was from the shaker input to the accelerometer output. In order to improve the adaptation algorithm, the plant transfer function included a second order Butterworth high pass filter set at 40 Hz and a second order low pass Butterworth filter set at 1000 Hz. These filters were implemented in software by the dX-100.

The plant transfer function estimate is compared to the experimentally measured transfer function in Figure 4.31. The measured transfer function was modified to include the effects of the controller software filters. The plant filter was able to accurately fit the magnitude and phase of the first two measured resonances. However, both the high frequencies and the low frequencies were not accurately modeled using the limited number of filter coefficients. Although the general characteristics of the

phase were captured, there were inaccuracies as large as 80 degrees over the 100-8000 Hz range.

After modeling the plant transfer function, the adaptation of the controller filter was begun. The controller filter was an IIR filter with 30 numerator coefficients and 29 denominator coefficients. The adaptation was left on during testing. The acceleration from the feedback sensor and the sound pressure at a microphone location were measured. The controlled and uncontrolled acceleration power spectra for a flow speed of 26.9 m/s (60 MPH) are shown in Figure 4.32. As expected, the controller reduced the acceleration at the feedback sensor location. The primary reductions occurred at the modal resonances of the plate. The Nichols chart of the open loop transfer function is shown in Figure 4.33. This plot shows that the lowest sensitivity was achieved at the first and fourth structural resonance 981 rad/sec and 3542 rad/sec respectively. The controller has phased the resonances to achieve the lowest sensitivity near these frequencies. This was accomplished using a pair of complex non-minimum phase zeros at $\omega = 3400\ rad/s, \zeta = 0.13$. The controller gain decreased at higher frequencies which kept the higher order modes from becoming unstable.

Improved results could have been achieved if additional phase lag were used to lag the eighth resonance near 5655 rad/sec. This would have pushed this resonance away from the stability point at -900 degrees. With this additional phase lag, the controller gain could have been increased resulting in improved attenuation while maintaining stability.

Although the sound pressure level played no part in the controller implementation, sound pressure level reductions were achieved. The sound pressure levels of the microphone for the uncontrolled and the controlled case are shown in Figure 4.34. The sound pressure level reductions were achieved at the structural resonances of the plate. Approximately 4 dB of control was achieved at the first structural resonance and 3 dB of control at the fourth structural resonance. The sound pressure level reduction across the 100-1000 Hz band was 1.3 dB.

The controller performed slightly better for a flow speed of 35.8 m/s (80 MPH). As before, the acceleration of the resonance frequencies was reduced (Figure 4.35). The reduction in acceleration resulted in the sound pressure level reduction shown in Figure 4.36. Approximately 8 dB and 5 dB of reduction were achieved at the frequencies of the first and fourth structural resonance respectively. The Nichols chart of the open loop for the 35.8 m/s (80 MPH) case is shown in Figure 4.37. The plot is similar to that of the 26.9 m/s (60 MPH) case. The primary sensitivity reductions are achieved at the first and fourth modal resonances. As in the 26.9 m/s (60 MPH) case, the eighth modal resonance is near the -900^o degrees stability point. Since the sensitivity near the eighth mode is greater than unity, disturbance rejection in this region is poor. In fact, the acceleration in this region increased by approximately 2 dB (Figure 4.35).

The closed loop system did not remain stable for the 40.2 m/s (90 MPH) test. Although the controller filter was stable at the start, after approximately 2 minutes of adaptation an unstable controller design was reached. The adaptation algorithm could not recover from the unstable state. Repeated investigations resulted in the same outcome. To better understand the cause of the instability, the controller adaptation was turned off prior to the occurrence of instability and the controller coefficients, acceleration, and sound pressure level were recorded.

The Nichols chart of the open loop transfer function is shown in Figure 4.38. The open loop was similar to those for the 26.9 and 35.8 m/s (60 and 80 MPH) cases over most of the frequency range of interest. The first and fourth modal resonances had sensitivity reduction and would have achieved acceleration attenuation. As in the other cases, the eighth modal resonance did not have enough phase lag and is centered under the 900^o stability point. For the 40.2 m/s (90 MPH) case the frequencies associated with the eighth mode (5200 rad/sec) are much closer to the stability point. The gain margin is approximately 5 dB less for the 40.2 m/s (90 MPH) case at this gain crossover frequency than for the 26.9 m/s (60 MPH) case.

Therefore the frequencies in the 5200 rad/sec region have an increased sensitivity resulting in poor performance.

The most significant difference in the open loop transfer function was the increased gain near 1520 rad/sec. The frequencies near 1520 rad/sec were close to the stability point of -540^o. Furthermore, the frequencies near 1520 rad/sec did not correspond with high levels of acceleration. Therefore, the controller gain in this region was unnecessary. It is believed that the gain near the 1520 rad/sec frequency increases with continued adaptation. As the gain increased the open loop encircled the -540^o stability point resulting in closed loop instability.

The controlled and uncontrolled vibration spectra for the 40.2 m/s (90 MPH) case are shown in Figure 4.39. As expected, the first and fourth modal resonance are attenuated. The attenuation is similar to that achieved in the 35.8 m/s (80 MPH) case. The predicted poor performance near the eighth modal resonance is shown in the plot as an increase in the acceleration by approximately 4 dB. Additionally, the poor performance near 1520 rad/sec caused an increase in the acceleration of approximately 4 dB. As shown in the plot there was not a significant amount of acceleration in this frequency region. Thus, the time domain gradient based adaptive algorithm converged to a solution that does not make sense from a frequency domain design point of view. The controlled and uncontrolled sound pressure levels are shown in Figure 4.40. Aside from the increase in the sound pressure level near the 1520 and 5200 rad/sec bands, the reduction is similar to that achieved in the 35.8 m/s (80 MPH) case.

Bode plots of the adaptive feedback controllers for each flow speed are shown in Figure 4.41. All of the controllers had non-minimum phase zeros near $\omega = 3400$ with damping ratios near $\zeta = 0.13$. These non-minimum phase zeros added phase lag such that the fourth modal resonance is between the -540^o and -900^o stability points. The controller for the 26.9 m/s (60 MPH) case had a gain less than one at all frequencies. The controllers for the 35.8 and 40.2 m/s (80 and 90 MPH) cases had gains greater than one at some frequencies. Both of these controllers had a

pair of lightly damped zeros ($\zeta = 0.053$, $\omega = 961\ rad/sec$) near the first resonance. This reduced the gain and therefore the acceleration attenuation of the first mode. The high frequency oscillation of the transfer functions occurred as a result of lightly damped poles and zeros which are equally spaced in frequency. This indicates that more controller filter coefficients were used than were necessary.

The problem with the 40.2 m/s (90 MPH) case is shown in its controller Bode plot (Figure 4.41). A pair of lightly damped poles ($\zeta = 0.026$, $\omega = 1527\ rad/sec$) resulted in a large gain in the 1520 rad/sec region. The z domain plot of the controller poles and zeros is shown in Figure 4.42. The poles at $\omega = 1527\ rad/sec$ are close to the unit circle. Thus, the IIR controller filter is close to being unstable. As these poles moved closer to the unit circle, the open loop gain increased causing closed loop instability.

The adaptation of IIR filter coefficients which results in unstable filters has been observed by Scheper [72]. In her investigations, adapting filters were observed to cross the stability boundaries several times before finally converging to the proper values. Thus, the adaptation algorithm was able to recover from the filter instability. However, in this investigation a feedback configuration was used. As a result, the filter instability caused a closed loop instability from which the adaptation algorithm did not recover.

4.3.3 Adaptive Feedback Controller Conclusions

The experimental investigation has yielded important information regarding the use of adaptive feedback algorithms for active control of structural sound radiation problems. The adaptive feedback algorithm was found to be ineffective when sound pressure was used as the feedback variable. This was a direct result of the difficulties associated in modeling the pure delay associated with sound propagation. In order to avoid these problems, acceleration feedback was used. However, acceleration feedback

is not guaranteed to minimize the sound pressure levels. Therefore, the largest sound pressure level reductions may not be achieved by minimizing the acceleration.

With acceleration feedback, sound pressure level reductions were achieved at the frequencies associated with the resonances of the structure. After adaptation, the controller filter included non-minimum phase zeros which provided phase lag to space the system resonances. In this way the plant dynamics were utilized by the controller. However, additional gain could have been used to improve performance.

An important aspect of broadband vibration and noise problems is the bandwidth that can be controlled. In adaptive feedback control the processing time associated with the adaptation algorithm is a primary consideration. In this investigation, the sample rate was limited to 5000 Hz which restricted the controller performance.

Another major drawback to adaptive feedback control is its apparent instability under certain conditions. The instability was shown to be a result of the adaptation to unstable IIR filters. If adaptive feedback control is to be considered, techniques for maintaining closed loop stability must be found.

4.4 Conclusions

In this chapter the active control of flow induced structural sound radiation has been shown to present many challenges for active control. The dynamic systems describing the flow excitation, structural response, and sound radiation are complex. As a result analytical models are inaccurate. Thus, model based controller methodologies require the inclusion of large amounts of uncertainty in order to describe the errors associated with the model. Furthermore, the inclusion of a large system model results in high order controllers in some control methodologies. Therefore, a non-model based control methodology is desirable.

The flow induced structural sound radiation problem is broadband in nature. This necessitates a high bandwidth controller. Therefore, computationally intensive

control algorithms are not feasible. Although sound pressure reductions are required, the sound pressure level cannot be utilized as feedback. This is a consequence of the delay associated with sound propagation. Furthermore, the blind use of acceleration feedback does not necessarily result in sound pressure level reductions. Therefore, the controller must relate the acceleration feedback to the amount of sound radiated from the structure.

Another difficulty associated with this problem is that the plant transfer functions change significantly over the operating range of the system. Thus, the controller must account for a large degree of system uncertainty. Furthermore, the controller must maintain robust stability and performance over the entire operating region. Control methodologies which do not consider robustness can not be utilized.

Finally, it is important that the control methodology guarantee that specific performance criteria are satisfied. The impact of these criteria on the controller design should be clear to the designer. In this way, the impact of the performance requirements on the number of control actuators, sensors, and control effort can be discerned.

Table 4.1 System Parameters

Plate Material	Aluminum
Plate Dimensions (a,b,h)	(0.4,0.2,0.001) m
Modal Damping Ratio	0.01
Actuator Location	(a/2,b/2)
Sensor Locations	(a/2,b/2)
Controlled Location	(2m,45deg,45deg)
Fluid	Air
Air Velocity U_∞	38 m/s (85 mi/hr)
Convected Velocity U_c	0.65 U_∞
γ_1	0.115
γ_3	0.7

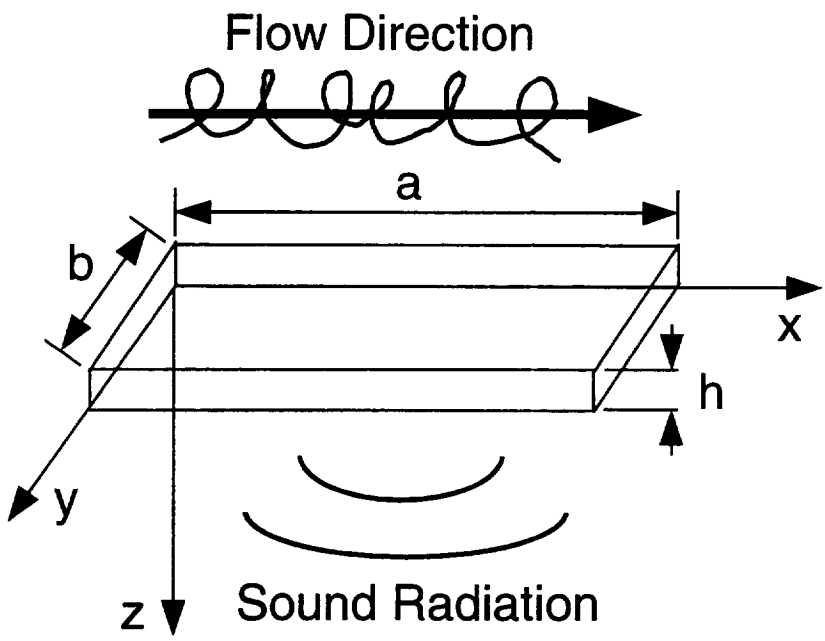

Figure 4.1 Pictorial Representation of System

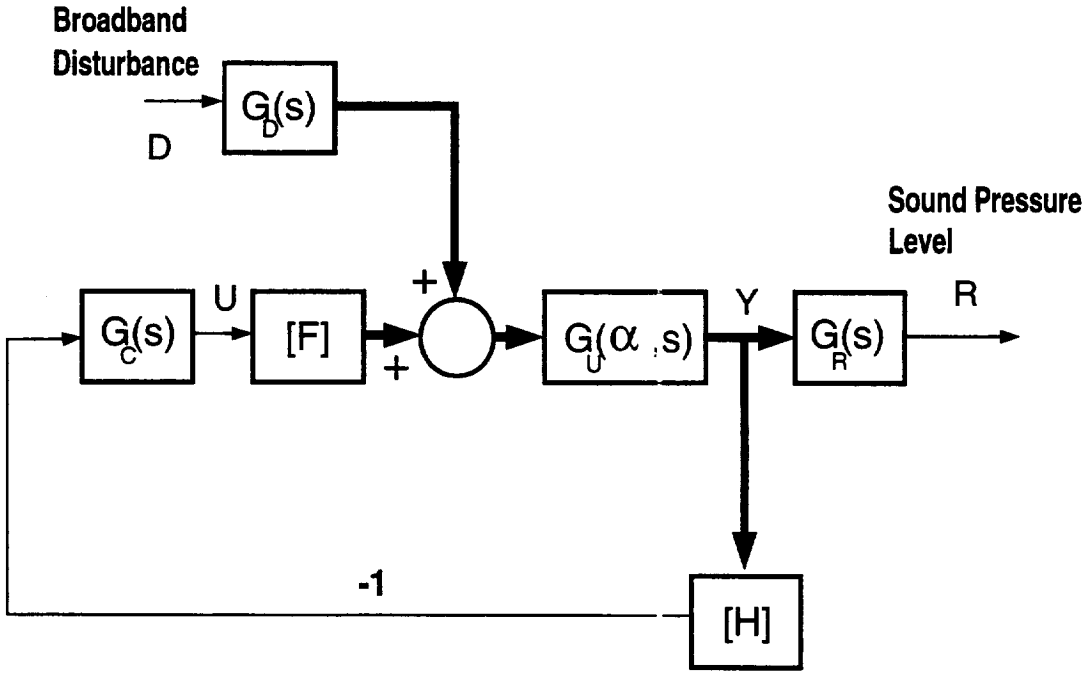

Figure 4.2 Block Diagram of System

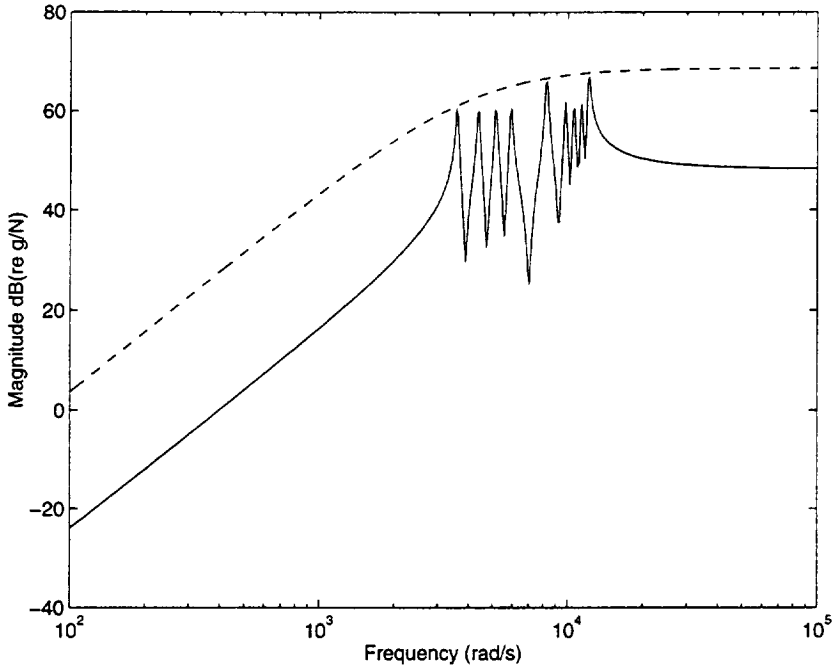

Figure 4.3 Bounding of Unstructured Uncertainty; Actual —; Fit - -

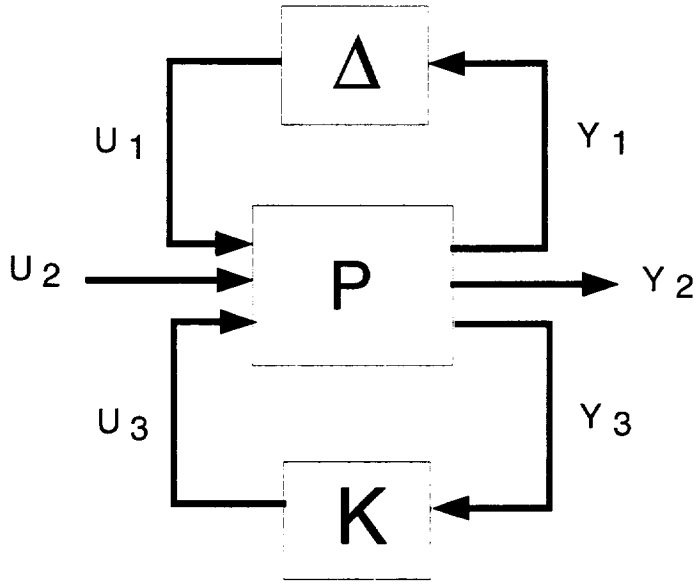

Figure 4.4 H_∞, μ Synthesis Framework

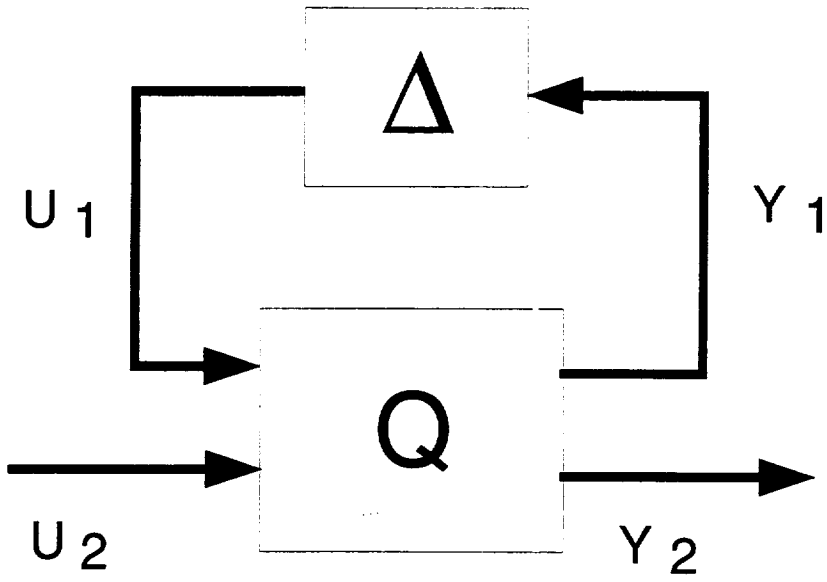

Figure 4.5 System Representation with Linear Fractional Transformation

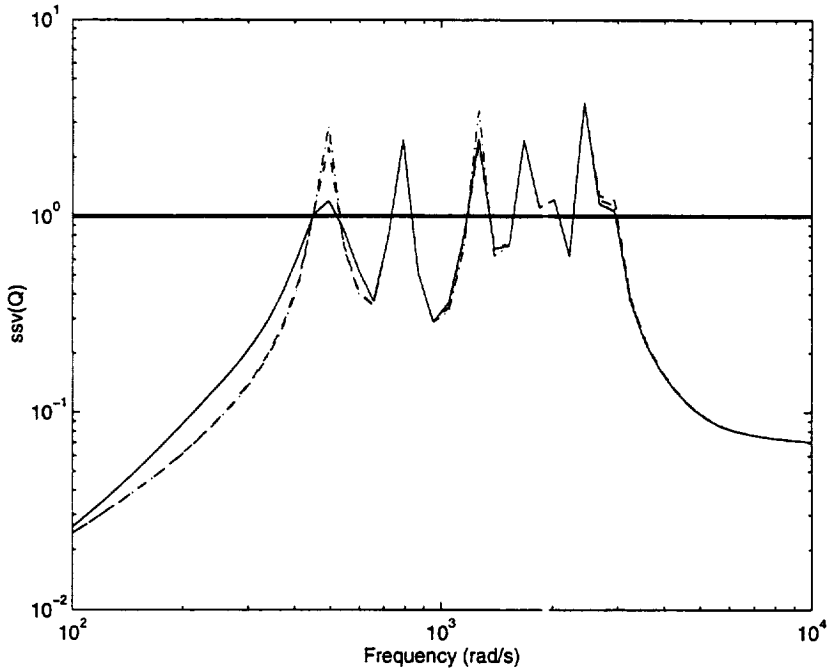

Figure 4.6 Robust Performance; $\Delta\zeta = 5\%$, $\Delta\omega_r = 1\%$, $P_{des} = 105\ dB$; Iteration No. 1 —; 2 - -; 3 – ·

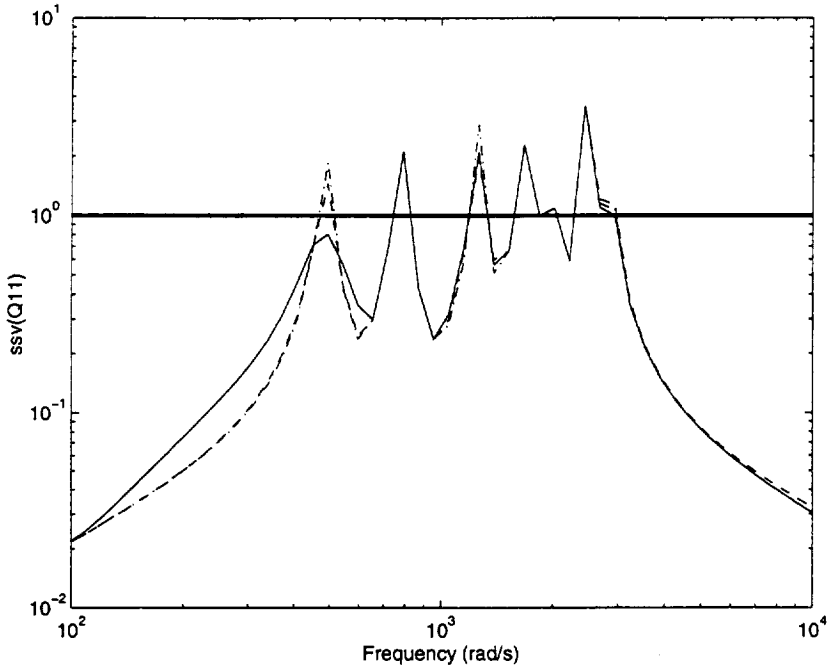

Figure 4.7 Robust Stability; $\Delta\zeta = 5\%$, $\Delta\omega_r = 1\%$, $P_{des} = 105\ dB$; Iteration No. 1 —; 2 - -; 3 – ·

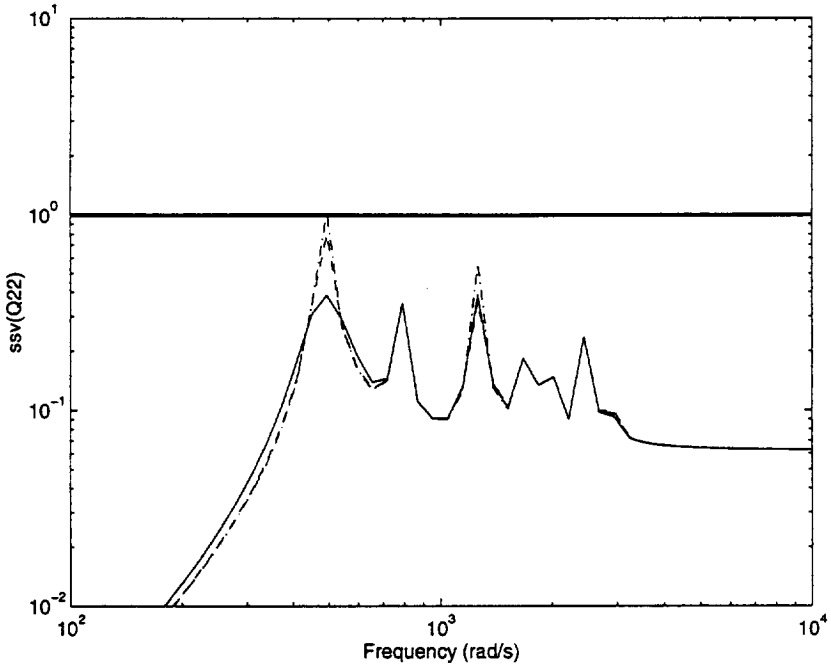

Figure 4.8 Nominal Performance; $\Delta\zeta = 5\%$, $\Delta\omega_r = 1\%$, $P_{des} = 105\ dB$; Iteration No. 1 —; 2 - -; 3 – ·

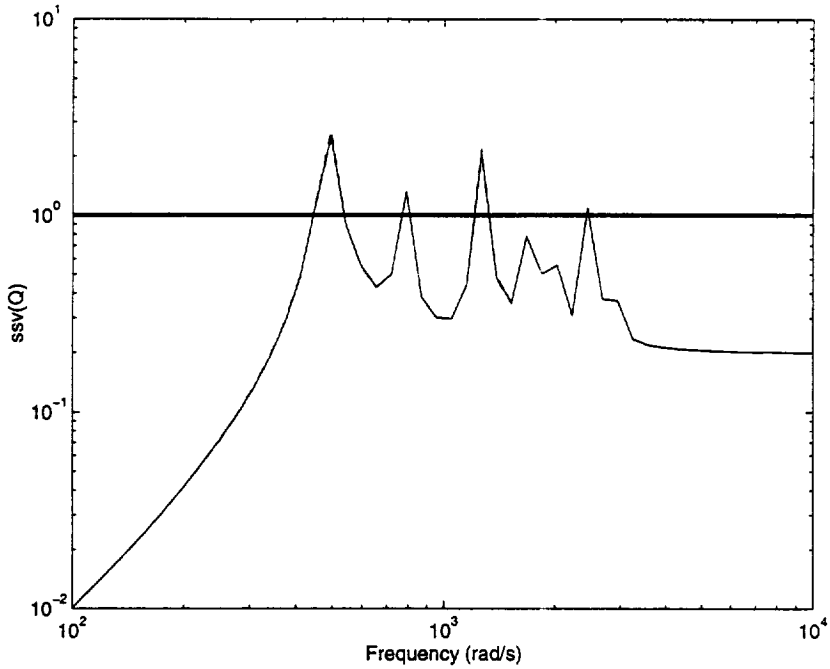

Figure 4.9 Robust Performance; $\Delta\zeta = 0.5\%$, $\Delta\omega_r = 0.1\%$, $P_{des} = 100\ dB$; Iteration No. 1 —; 2 - -; 3 - ·

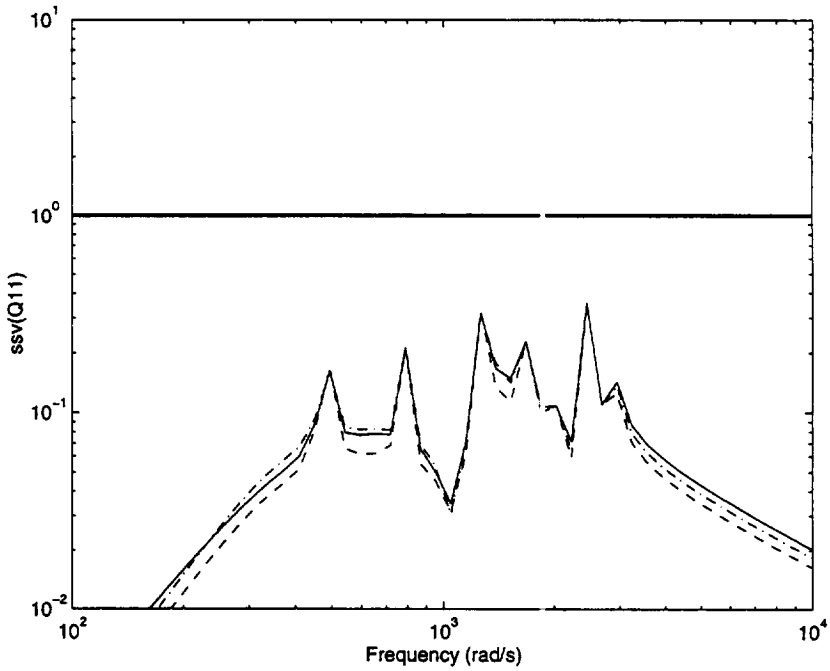

Figure 4.10 Robust Stability; $\Delta\zeta = 0.5\%$, $\Delta\omega_r = 0.1\%$, $P_{des} = 100\ dB$; Iteration No. 1 —; 2 - -; 3 - ·

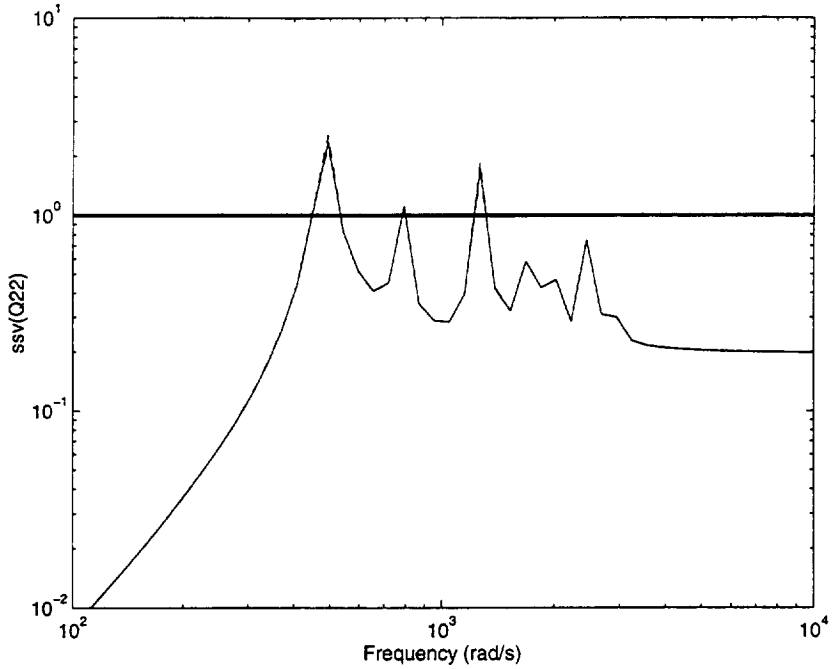

Figure 4.11 Nominal Performance; $\Delta\zeta = 0.5\%$, $\Delta\omega_r = 0.1\%$, $P_{des} = 100\ dB$; Iteration No. 1 —; 2 - -; 3 – ·

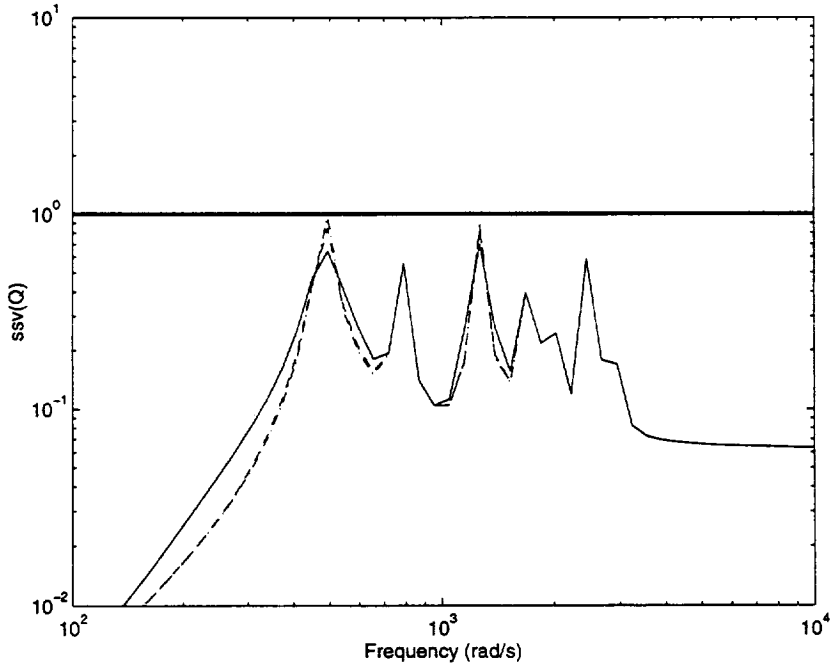

Figure 4.12 Robust Performance; $\Delta\zeta = 0.5\%$, $\Delta\omega_r = 0.1\%$, $P_{des} = 105\ dB$; Iteration No. 1 —; 2 - -; 3 – ·

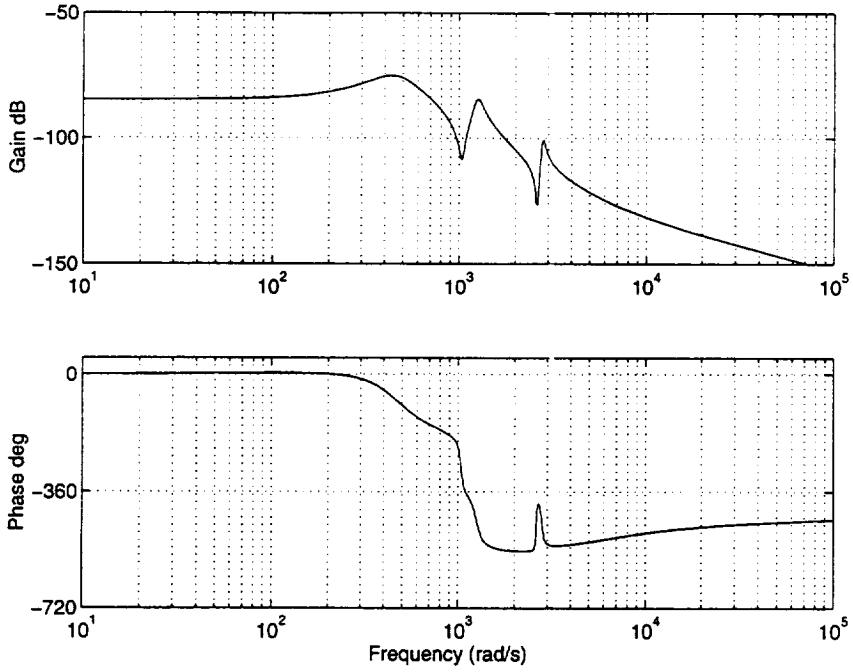

Figure 4.13 Bode Plot of μ Synthesis Controller $G_C(s)$

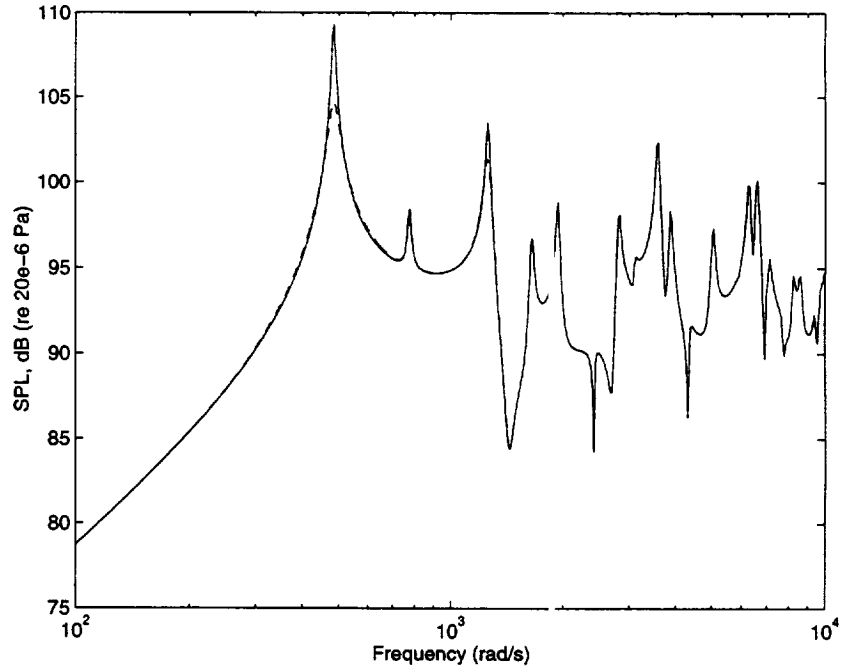

Figure 4.14 Sound Pressure Level for Point Force Excitation; Uncontrolled —; Controlled - -

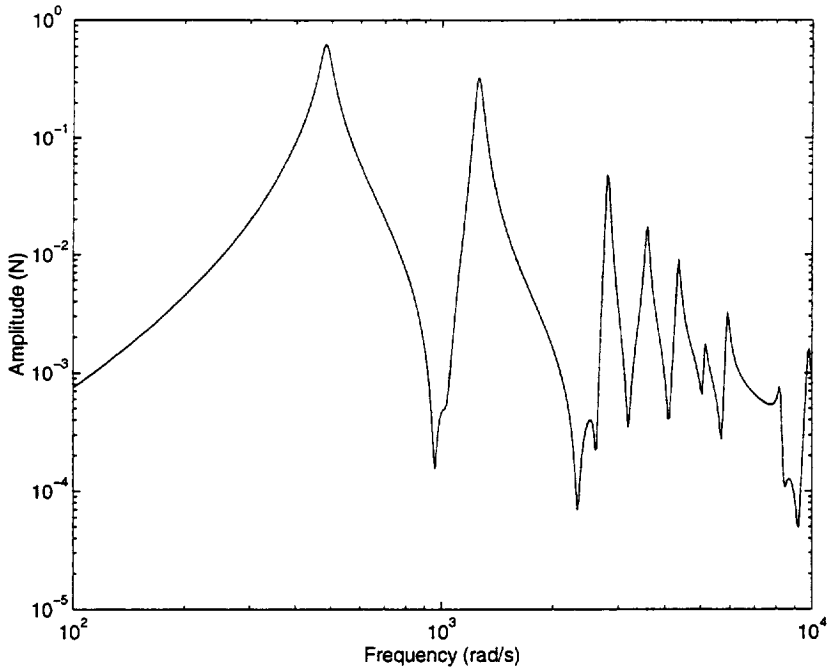

Figure 4.15 Control Effort for Point Force Excitation

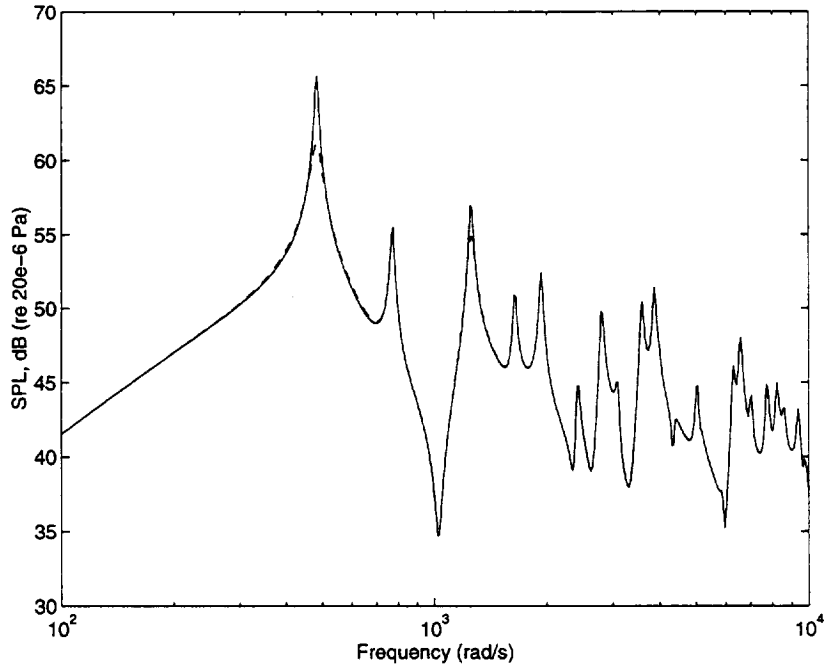

Figure 4.16 Sound Pressure Level for the Turbulent Flow Excitation; Uncontrolled —; Controlled - -

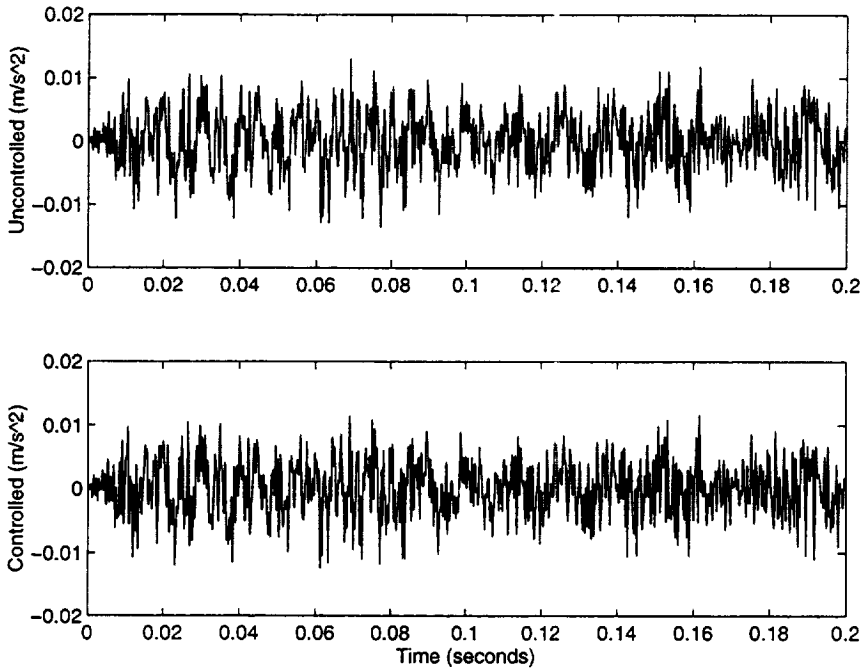

Figure 4.17 Sensor Acceleration for Flow Disturbance

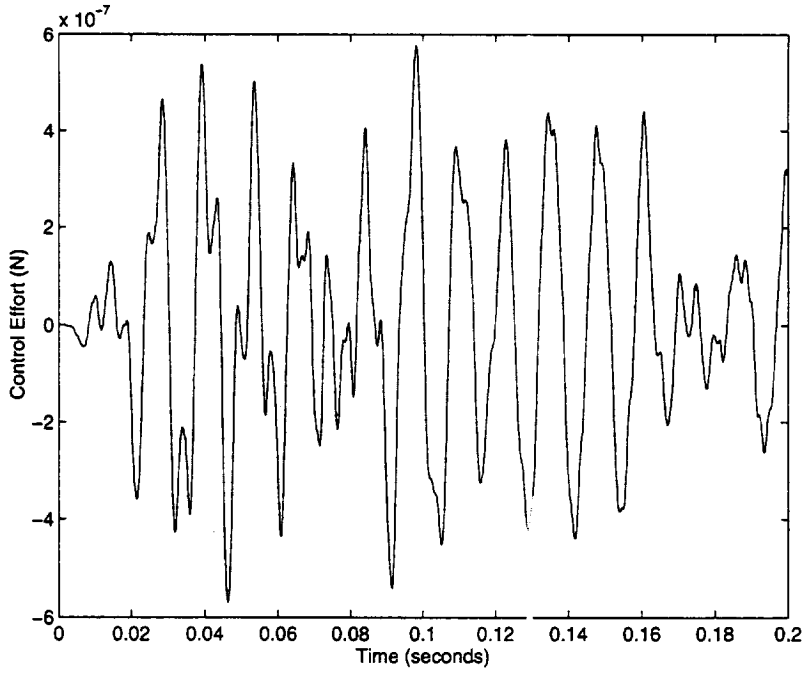

Figure 4.18 Control Effort Response to Flow Disturbance

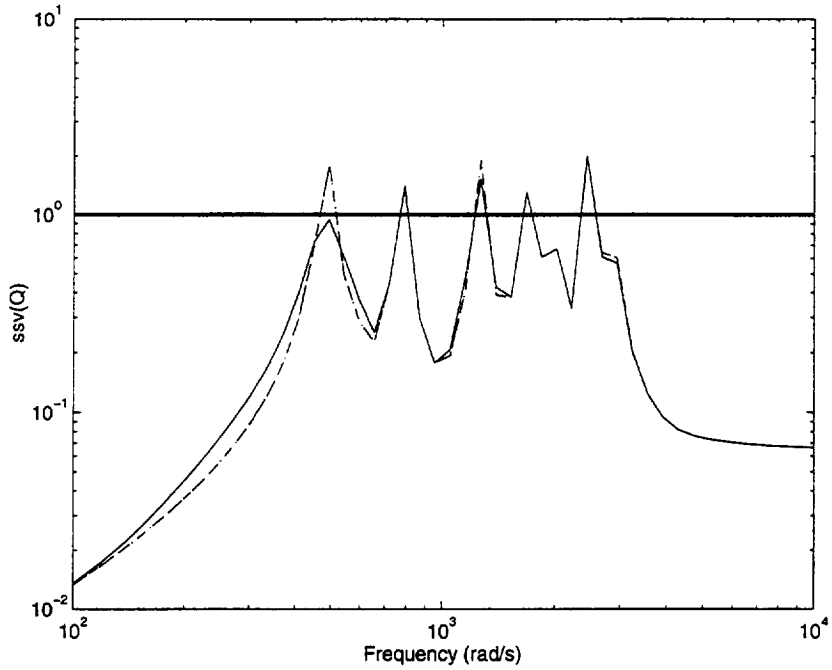

Figure 4.19 Robust Performance with Constant D Matrix; Iteration No. 1 —; 2 - -; 3 – ··

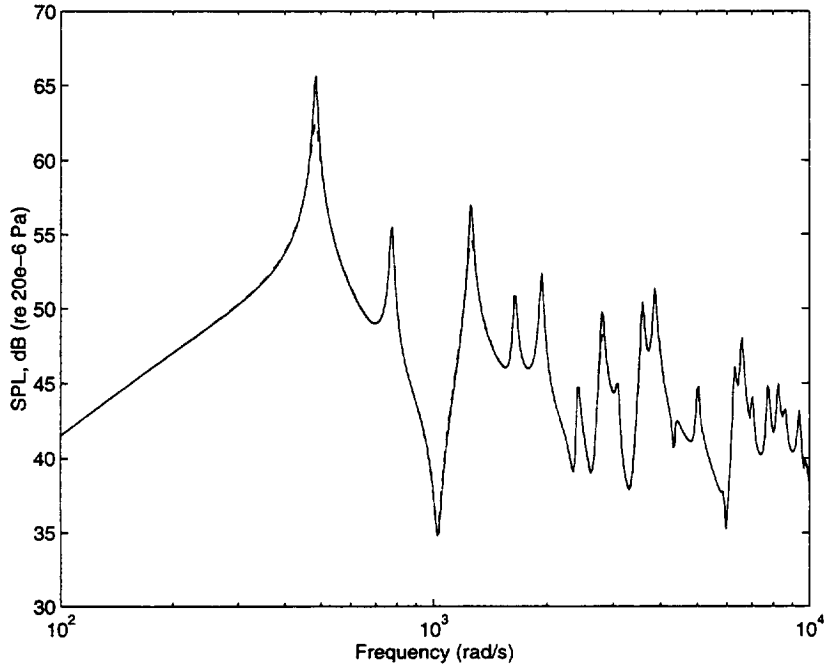

Figure 4.20 Sound Pressure Level for the Turbulent Flow Excitation with Constant D Matrix; Uncontrolled —; Controlled - -

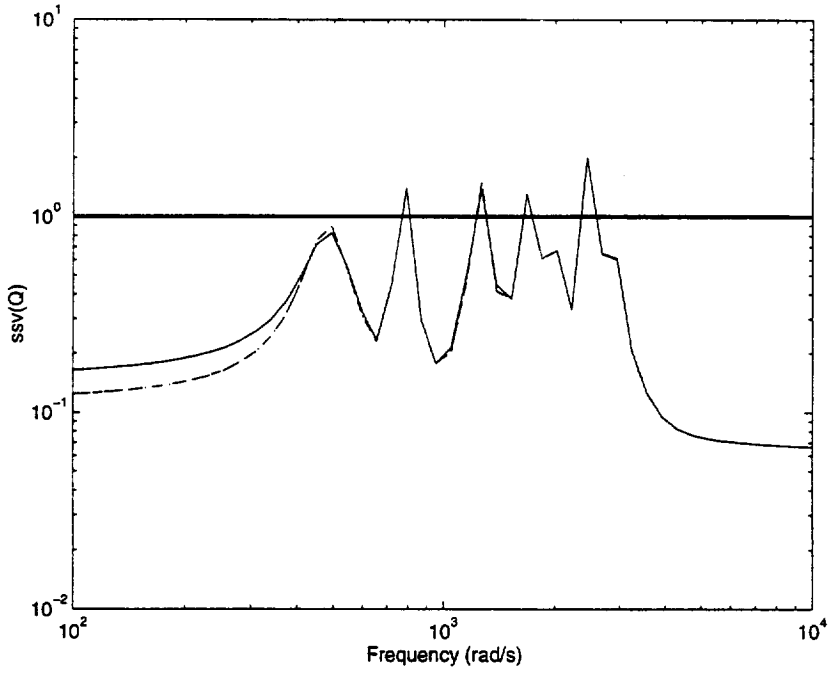

Figure 4.21 Robust Performance with Non-constant D Matrix; Iteration No. 1 —; 2 - -; 3 – ·

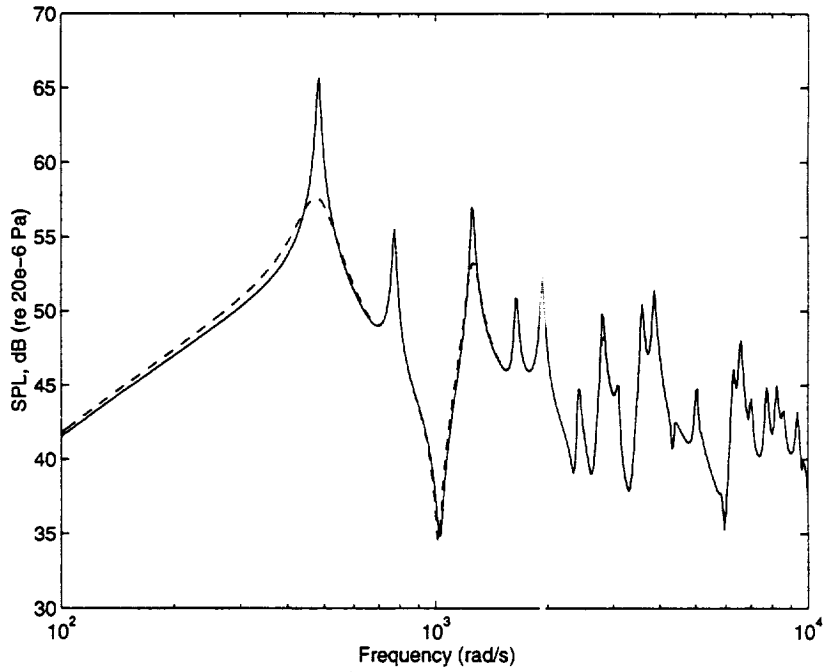

Figure 4.22 Sound Pressure Level for the Turbulent Flow Excitation with Non-constant D Matrix; Uncontrolled —; Controlled - -

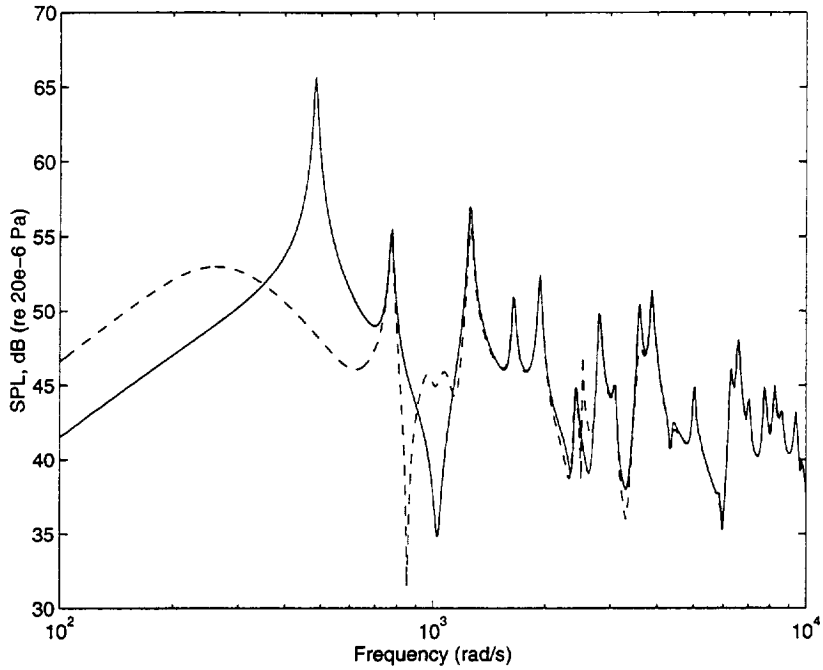

Figure 4.23 Sound Pressure Level $\Delta\zeta = 5\%$, $\Delta\omega_r = 1\%$, $P_{des} = 72\ dB$; $\kappa = 0.2\ N$; Uncontrolled —; Controlled - -

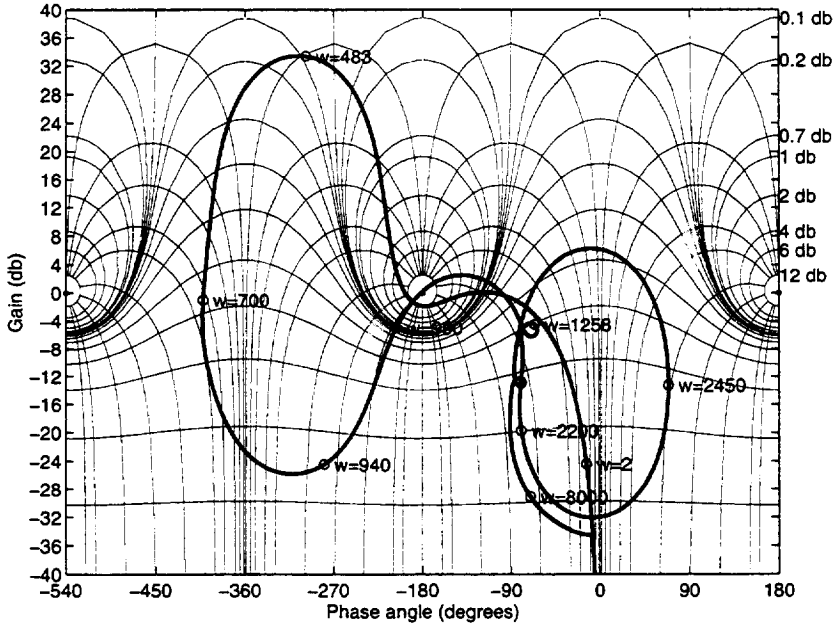

Figure 4.24 Nichols Chart Plot of Open Loop Unstable Design

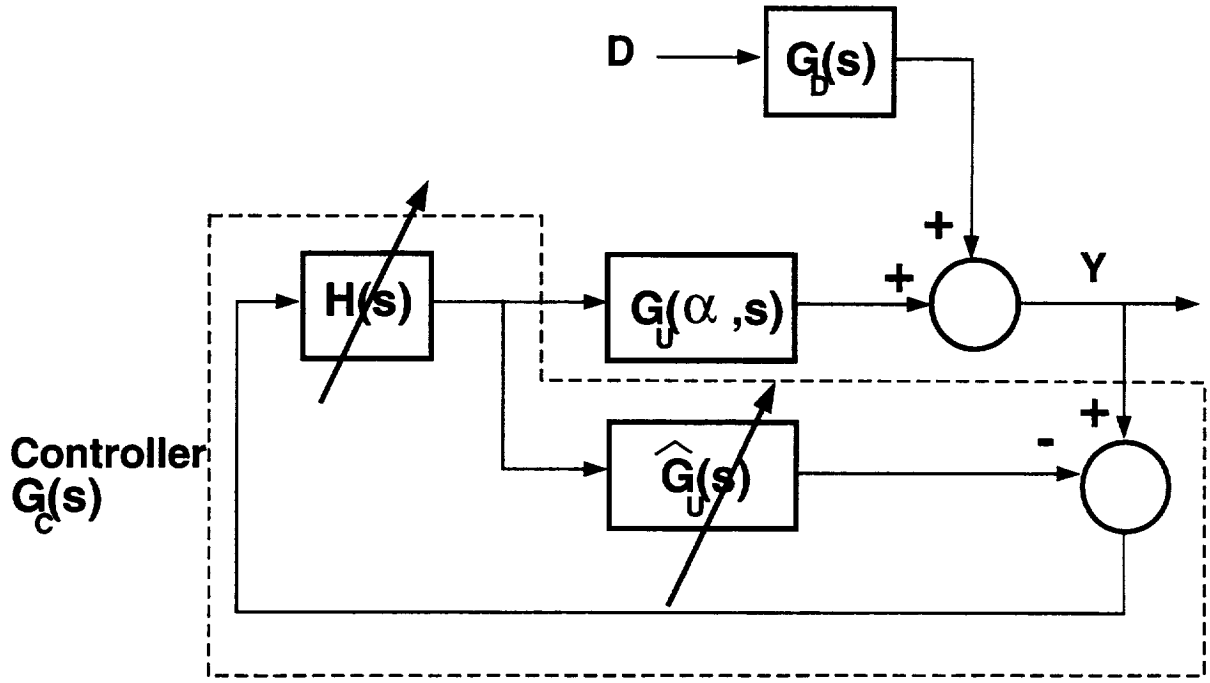

Figure 4.25 Block Diagram for an Adaptive Feedback Controller

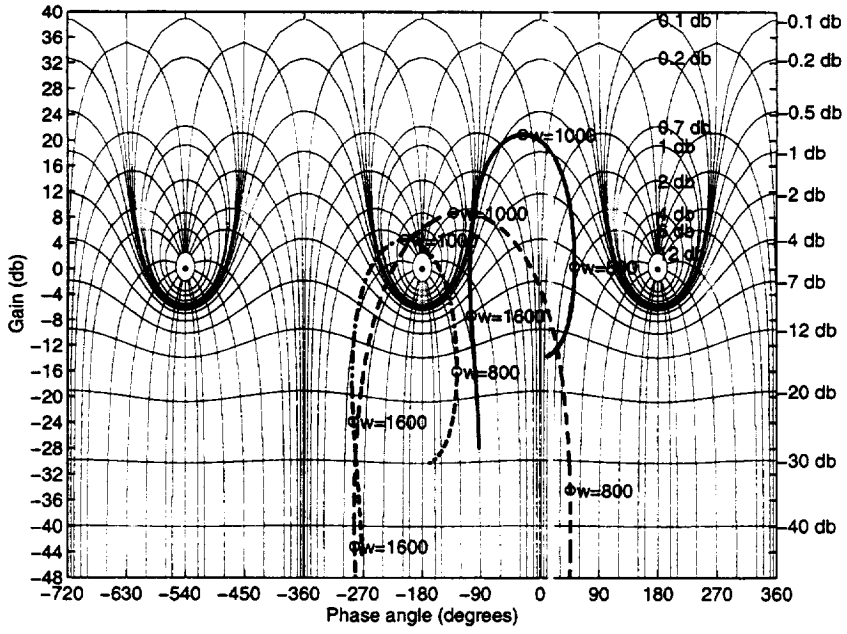

Figure 4.26 Nichols Chart of $\hat{L}$; Open loop —; $\hat{L}$ (Phase Error) - -; $\hat{L}$ (Gain Error) – .

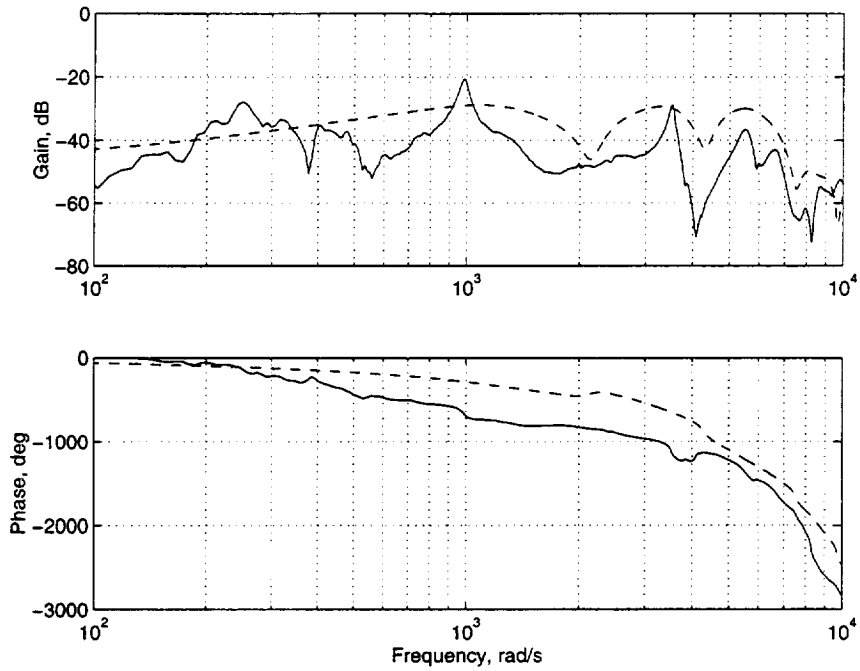

Figure 4.27 Plant Transfer Function (30 Numerator; 29 Denominator); Actual —; Controller Filter - -

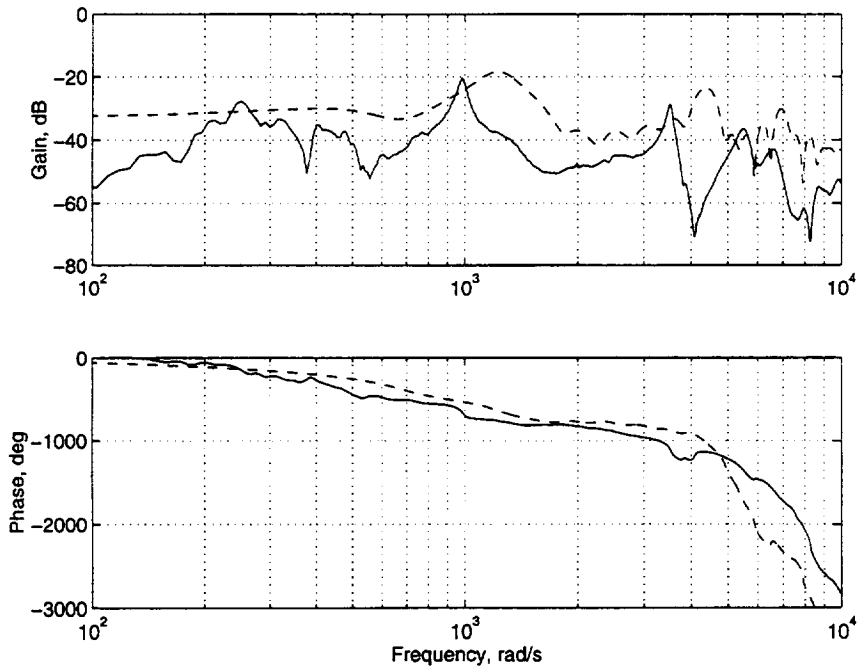

Figure 4.28 Plant Transfer Function (60 Numerator; 59 Denominator); Actual —; Controller Filter - -

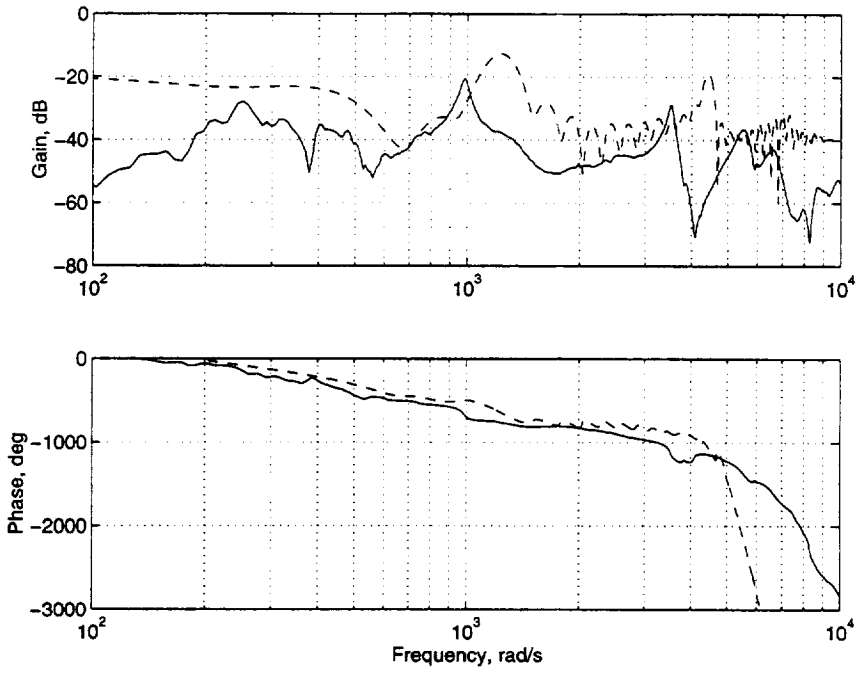

Figure 4.29 Plant Transfer Function (120 Numerator); Actual —; Controller Filter - -

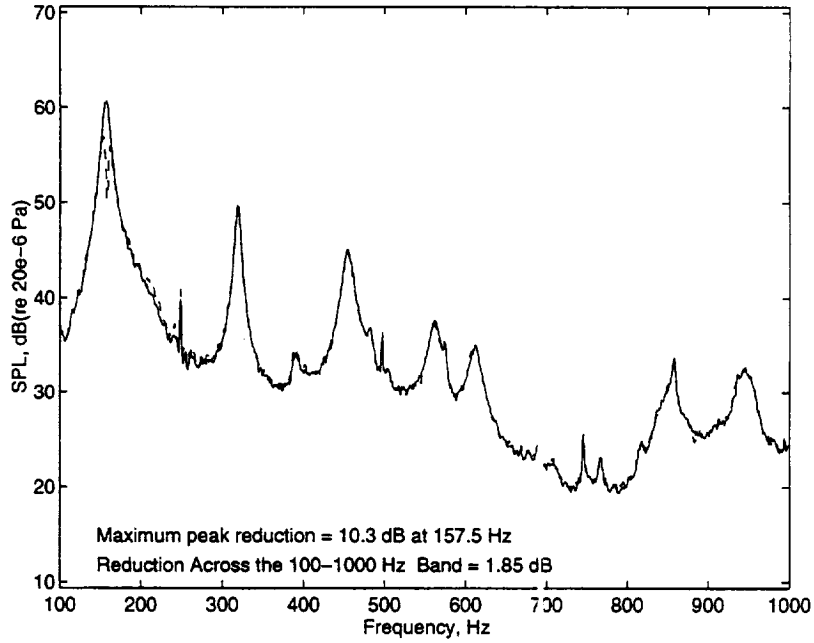

Figure 4.30 Sound Pressure Power Spectra (35.8 m/s); Uncontrolled —; Controlled - -

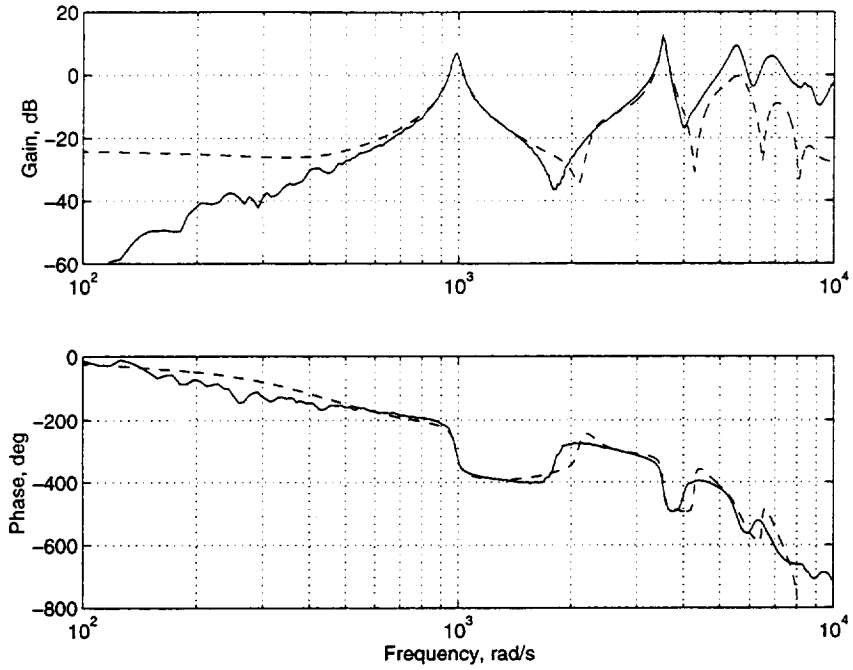

Figure 4.31 Plant Transfer Function; Actual —; Controller Filter - -

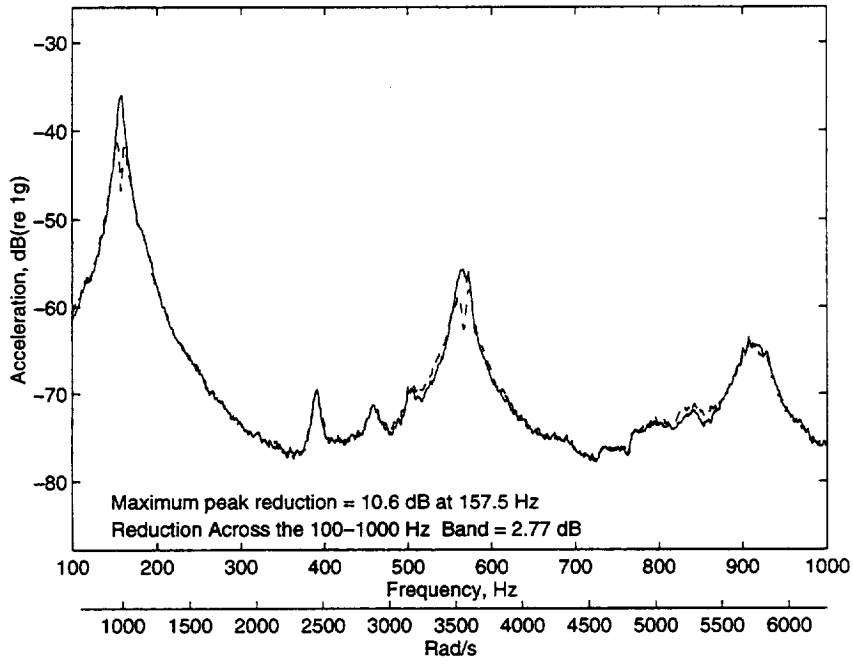

Figure 4.32 Acceleration Power Spectra (26.9 m/s); Uncontrolled —; Controlled - -

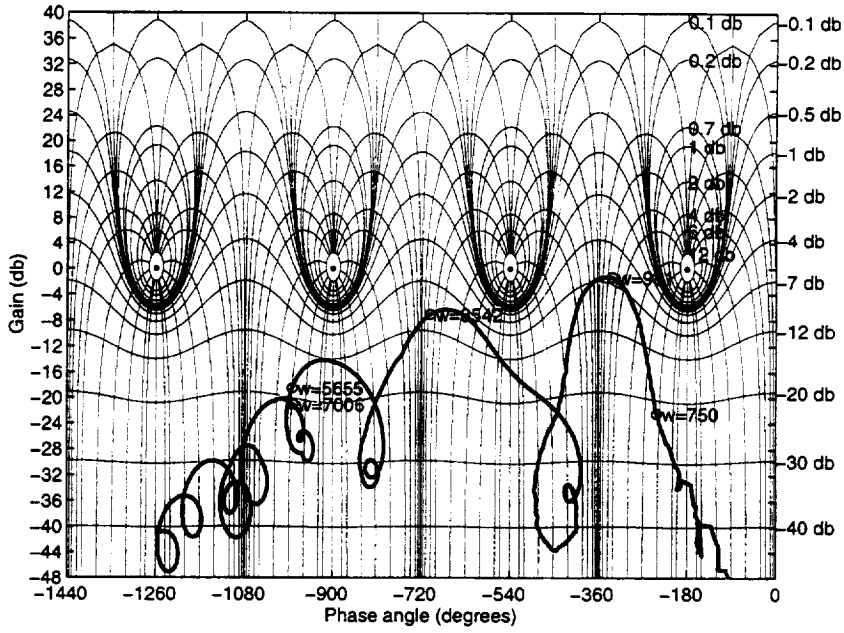

Figure 4.33 Nichols Chart of Open Loop (26.9 m/s)

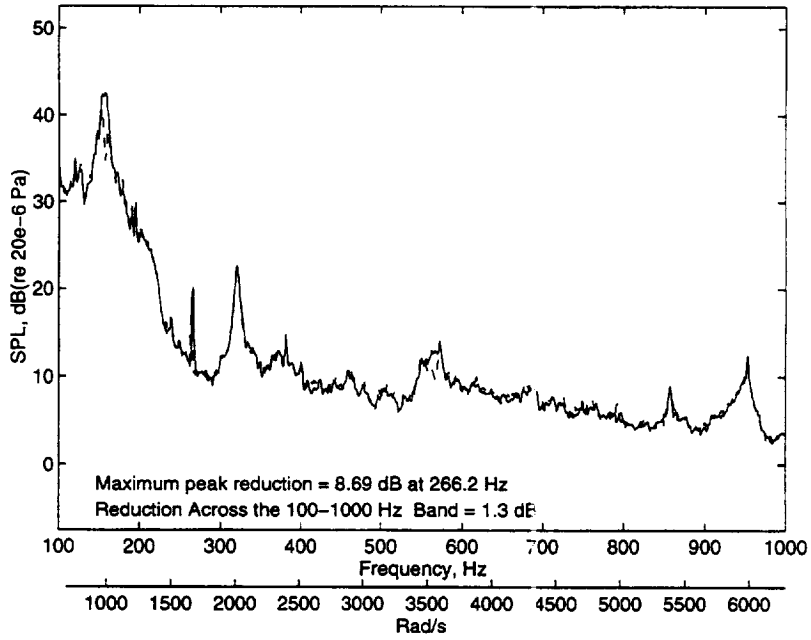

Figure 4.34 Sound Pressure Power Spectra (26.9 m/s); Uncontrolled —; Controlled - -

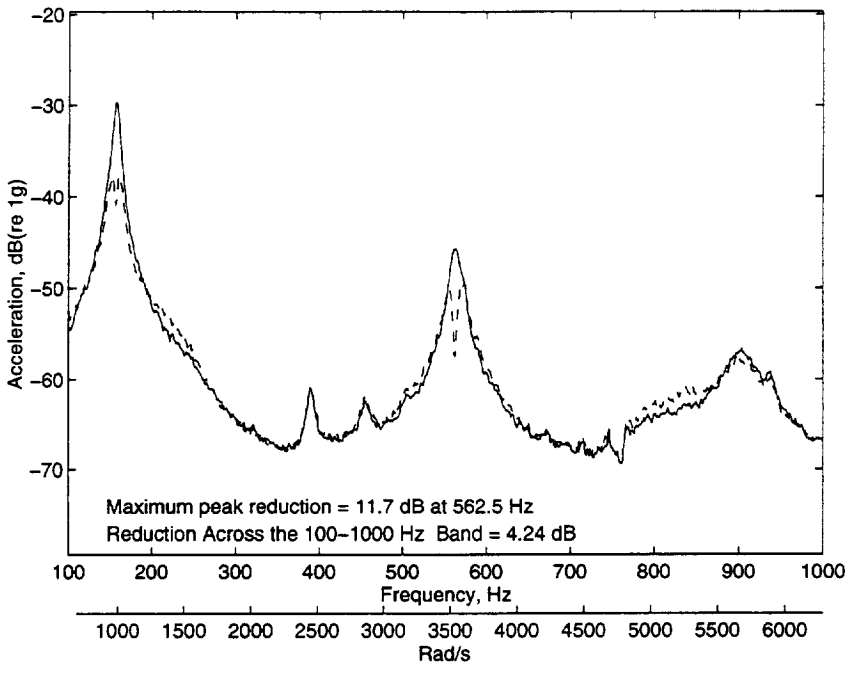

Figure 4.35 Acceleration Power Spectra (35.8 m/s); Uncontrolled —; Controlled - -

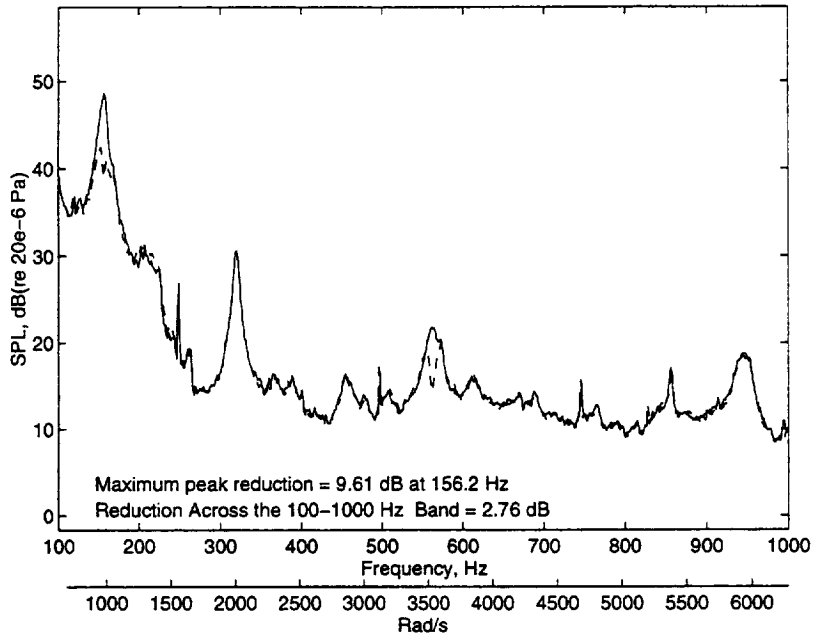

Figure 4.36 Sound Pressure Power Spectra (35.8 m/s); Uncontrolled —; Controlled - -

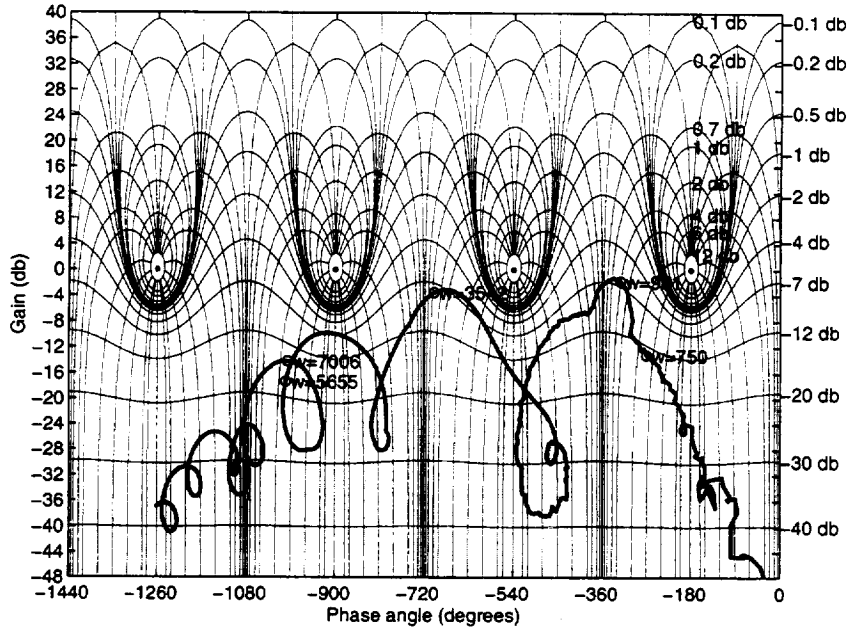

Figure 4.37 Nichols Chart of Open Loop (35.8 m/s)

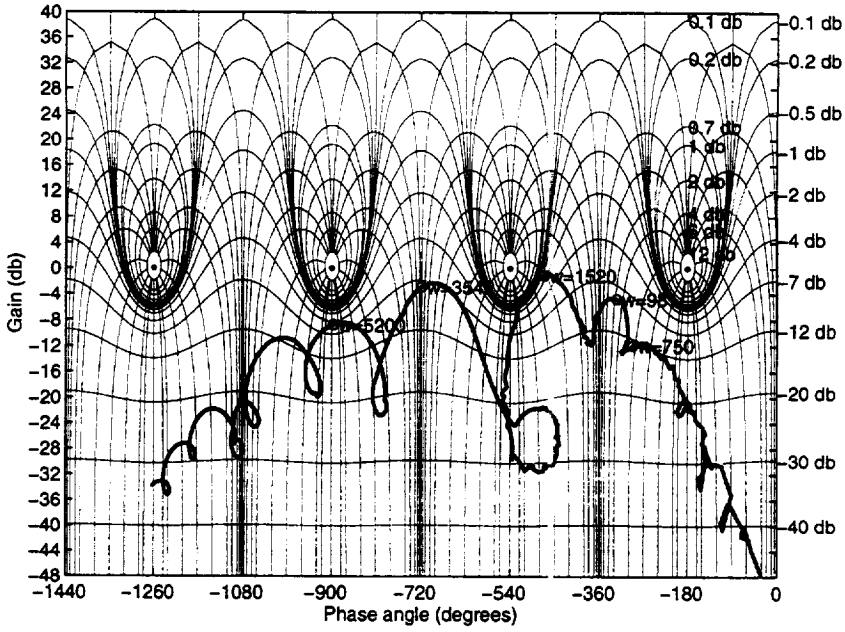

Figure 4.38 Nichols Chart of Open Loop (40.2 m/s)

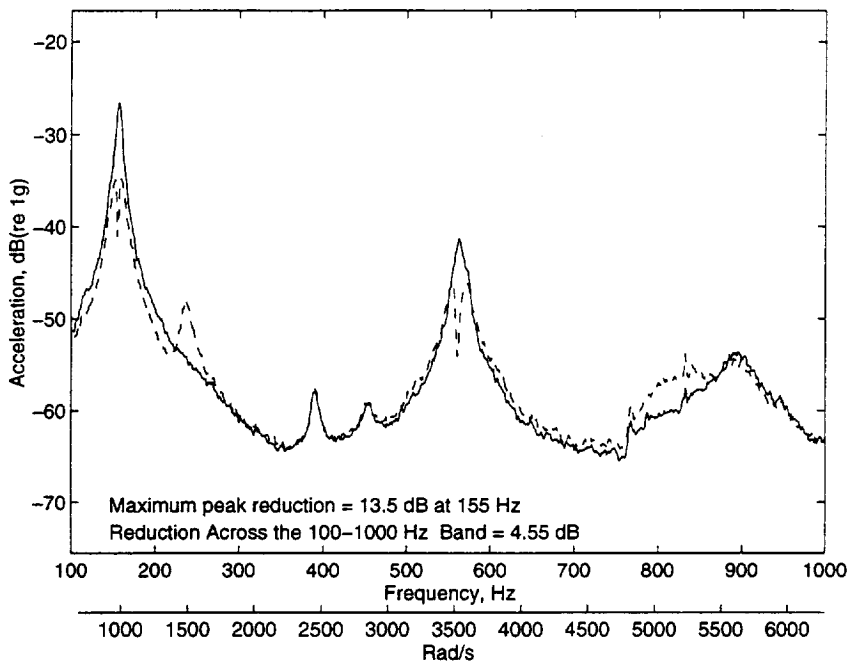

Figure 4.39 Acceleration Power Spectra (40.2 m/s); Uncontrolled —; Controlled - -

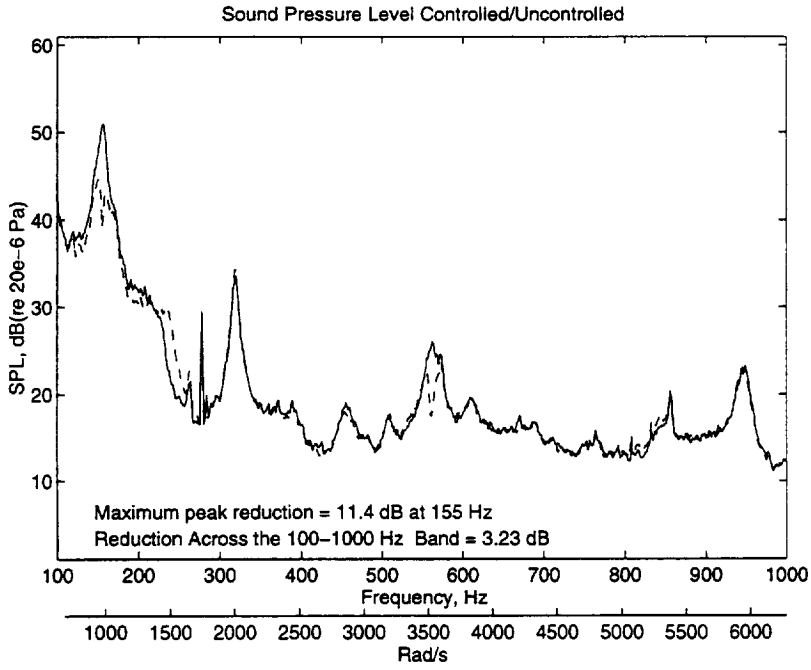

Figure 4.40 Sound Pressure Power Spectra (40.2 m/s); Uncontrolled —; Controlled - -

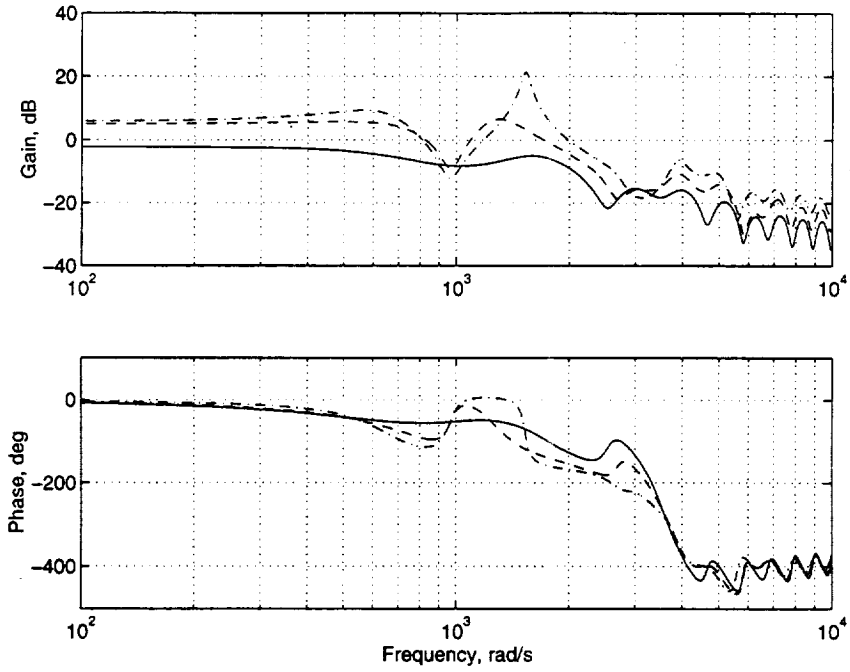

Figure 4.41 Bode Plot of Adaptive Feedback Controllers; 26.9 m/s —; 35.8 m/s - -; 40.2 m/s – ·

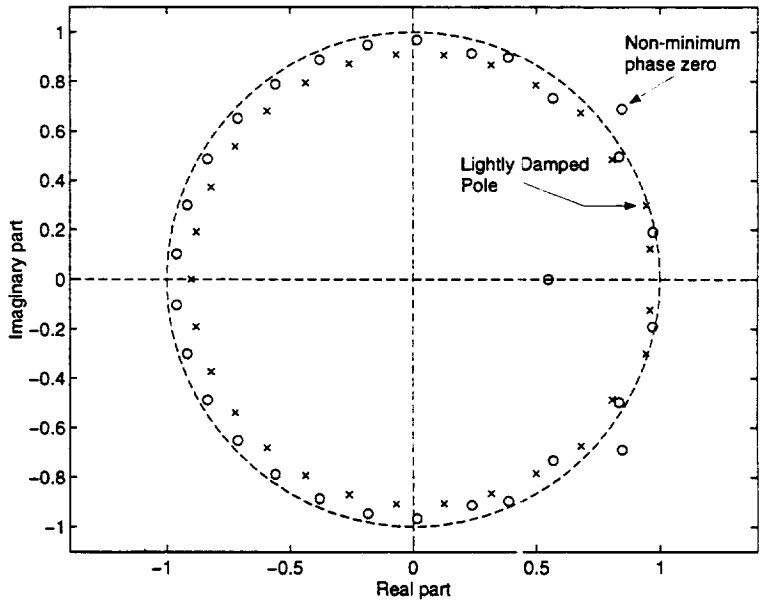

Figure 4.42 Controller Pole/Zero Plot (40.2 m/s)

CHAPTER 5. ROBUST FREQUENCY DOMAIN CONTROLLER DESIGN AND EVALUATION

In this chapter a robust frequency domain controller design methodology is developed and evaluated for control of turbulent flow induced structural radiation of sound. Both SISO and MIMO controllers were designed and tested. Additionally, an optimization considering both performance and controller issues is performed to determine the best actuator and sensor locations to be used. Finally, the robustness of the MIMO controller to unmeasured system variations is evaluated.

5.1 Controller Configuration

The performance of acoustical control problems is typically measured by the reduction of the power spectrum of the sound pressure level measured over a specified frequency range. As a result, in this work the controller is designed to achieve specified performance in the frequency domain rather than the time domain. The controller objective is to robustly reduce the radiated noise such that the time averaged power spectra of the sound pressure at the prespecified locations are less than the desired sound pressure level P_{des} subject to control effort limitation.

Although sound pressure is to be controlled, the sound pressure level is not used as feedback. For most applications, it would be impractical to position microphones at the locations where sound pressure level reduction is desired. Furthermore, using the sound pressure level as the feedback signal restricts the controller bandwidth which in turn limits closed loop performance. This is a direct result of the excessive phase lag associated with the delay of the sound propagation between the panel and the

sensor location. As the distance between the sound pressure feedback sensor and the radiating surface increases, so does the amount of delay.

The problem associated with system delay is illustrated using the single mode plant given by

$$G_U(s) = \frac{0.2(s/500+1)}{((s/1000)^2 + 2(0.02)s/1000 + 1)} \tag{5.1}$$

which is plotted as a heavy solid line on an extended Nichols chart in Figure 5.1. Since the total phase associated with the mode is less than 180^o and the resonance is centered between the Nyquist stability points at 180^o and -180^o, a unit gain feedback controller which utilizes the system dynamics can be used. For a unit gain feedback controller the closed loop sensitivity is low at the modal resonance (1000 rad/s).

Consider the same modal plant containing a 6 $msec$ delay which is representative of a microphone sensor located 2 m from the structure. This delay introduces phase lag at all frequencies. The resulting transfer function is plotted as a heavy dashed line in Figure 5.1. The delay has significantly increased the phase lag associated with the mode. As a result, the response is unacceptably close to the stability points located at -180^o and -540^o. To achieve acceptable stability margins, the controller gain would have to be less than one. Since the controller must attenuate the response, the controller bandwidth has been limited. The spreading of the phase associated with a modal response due to the delay, as demonstrated in this example, is worse for higher modal frequencies or increased delay. Furthermore, controller dynamics can not be used to overcome large amounts of delay. For this reason, it is of great importance to avoid system delay.

To eliminate the delay associated with microphone feedback for acoustic systems, plate acceleration feedback rather than sound pressure level feedback is utilized. Although the sound pressure level is not used for feedback, it can be controlled indirectly using plate acceleration as feedback. Contrary to initial impressions, minimization of the plate acceleration does not guarantee that the sound pressure level will be minimized. Instead, the acceleration feedback must be weighted based on the uncontrolled sound pressure levels of the locations to be controlled. Thus microphones are

necessary for the controller design process, but are not part of the feedback control system. With this design method the structural response of the plate is modified such that it rejects the excitation of the turbulent flow field in the frequency regions that strongly contribute to the sound pressure levels at the locations to be controlled. The control actuation is provided by point force inputs to the plate.

5.2 Controller Design Methodology

The flow induced radiation of sound problem can be described using the feedback structure shown in Figure 5.2. $G_D(s)$ represents the modal excitation of the plate due to the turbulent boundary layer, $G_U(\alpha, s)$ represents the dynamics of the plate including uncertainty, $G_R(s)$ represents the sound level radiation to the control point due to the modal responses, and $G_C(s)$ is the feedback controller. H and F are the modal participation coefficients associated with the sensor and actuator, respectively. In Figure 5.2 the heavy lines indicate modal representations while the thin lines indicate measurable signals.

For this frequency domain controller design methodology, the open loop transfer functions are loop shaped on a Nichols chart using classical frequency domain design tools. The Nichols chart provides closed loop information, such as sensitivity and complementary sensitivity, based upon the open loop transfer function. The complementary sensitivity is the closed loop transfer function

$$\frac{L}{1+L} \tag{5.2}$$

where L is the open loop transfer function. In general, lower complementary sensitivity transfer functions utilize less control effort. Open loop transfer function values having a constant complementary sensitivity magnitude are M circles on the Nichols chart. The sensitivity transfer function is given by

$$\frac{1}{1+L}. \tag{5.3}$$

The sensitivity transfer function gives the influence of the disturbance on the closed loop output. A lower sensitivity gives greater disturbance rejection. Open loop transfer functions values having a constant sensitivity magnitude are inverted M circles on the Nichols chart.

The loop shaping procedure involves augmenting the natural plant dynamics $G_U(\alpha, s)$ with the dynamics of the controller such that the design objectives are achieved. The design objectives, sound pressure reduction, stability, and control effort limitations, are introduced into the design process in terms of bounds on the Nichols chart. These performance bounds define the acceptable design region by imposing amplitude and phase conditions on the open loop transfer functions to be designed.

The open loop transfer functions are loop shaped sequentially. The dynamics of the transfer function loops already designed are included in the bound development for the subsequent loops. If the bounds cannot be satisfied, additional control loops are added.

5.2.1 Performance Bound Generation

Performance bounds are generated by limiting the sound pressure level at the locations to be controlled to be less than a specific pressure level ($R(j\omega) \leq P_{des}(j\omega)$). Since sound pressure levels rather than acceleration are to be controlled, the unique approach of developing performance bounds for a non-measured parameter is used. In this novel approach, these bounds can be developed as if the control system were a MISO system. The interaction between the loops is considered in the performance bound development by including the dynamics associated with the previously designed loops in the generation of the performance bounds for the current loop. When

the sound pressure levels are to be controlled at multiple points, bounds are generated for each of the points. In this way multiple, MISO control problems are solved.

Using the system block diagram (Figure 5.2), the transfer function between the disturbance (D) and the sound pressure level at the microphone location to be controlled (R) for a controller having q loops is written as

$$R(\alpha, j\omega) = \frac{G_R(j\omega)G_U(\alpha, j\omega)G_D(j\omega)}{1 + L_1(\alpha, j\omega) + L_2(\alpha, j\omega) + \cdots + L_q(\alpha, j\omega)} D(j\omega). \tag{5.4}$$

where $L_m(\alpha, j\omega)$ is the mth open loop transfer function given by

$$L_m(\alpha, j\omega) = G_u(\alpha, j\omega)F_m G_{C_m}(j\omega)H_m. \tag{5.5}$$

The performance criteria at each microphone location is given by

$$|R(j\omega)| \leq |P_{des}(j\omega)|. \tag{5.6}$$

Equation 5.4 is substituted into the performance criteria (Equation 5.6) and used to develop the frequency domain bound associated with the kth loop of the controller. The bound is written as

$$\left| \frac{1}{1 + L_k^o(\alpha_o, j\omega)\mathcal{P}_k(\alpha, j\omega)} \right| \leq P_{des}(j\omega) \left| \frac{1 + \sum_{m=1}^{k-1} L_m(\alpha, j\omega)}{G_R(j\omega)G_U(\alpha, j\omega)G_D(j\omega)D(j\omega)} \right| \tag{5.7}$$

where $\mathcal{P}_k(\alpha, j\omega)$ accounts for the measured system uncertainty and the dynamics of the control loops which have already been designed. $\mathcal{P}_k(\alpha, j\omega)$ is given by

$$\mathcal{P}_k(\alpha, j\omega) = \frac{G_U(\alpha, j\omega)F_k H_k}{G_U(\alpha_o, j\omega)F_k H_k} \left(\frac{1}{1 + \sum_{m=1}^{k-1} L_m(\alpha, j\omega)} \right) \tag{5.8}$$

and $L_k^o(\alpha, j\omega)$ is the nominal open loop transfer function given by

$$L_k^o(\alpha_o, j\omega) = G_u(\alpha_o, j\omega)F_k G_{Ck}(j\omega)H_k. \tag{5.9}$$

The inequality expression of Equation 5.7 gives a sensitivity bound on the Nichols chart for the set of open loop transfer functions $L(\alpha, j\omega)$. The sensitivity bound is

an inverted M circle bound. There is a different bound associated with each ω and α pair. For loop shaping purposes it is desirable to loop shape a single transfer function rather than the entire set of transfer functions $L(\alpha, j\omega)$. Therefore, the bound is shifted in magnitude and phase by the normalized plant $\mathcal{P}_k(\alpha, j\omega)$ so that it becomes an amplitude bound on the nominal open loop transfer function, $L_k^o(\alpha_o, j\omega)$. Each $\mathcal{P}_k(\alpha, j\omega)$ is a function of the system uncertainty α and is determined by measuring the plant transfer functions for various operating conditions. Thus, the sensitivity bound at each frequency is shifted by multiple $\mathcal{P}_k$s corresponding to different measured plant transfer functions.

A unique $G_R(j\omega)$ exists for each location where the sound pressure level is to be controlled. Therefore, each $G_R(j\omega)$ is used with Equation 5.7 to develop sensitivity bounds associated with each of the locations to be controlled. Each set of bounds is shifted by $\mathcal{P}_k$ and plotted on the Nichols chart to define a design region for controller k at each frequency. To satisfy the inequalities from Equation 5.7, the magnitude of the nominal open loop transfer function at ω for uncertainty α must be greater than the shifted bound. Additional control loops are added only if Equation 5.7 cannot be satisfied with the existing loops. Note that the bounds associated with the kth loop incorporate the dynamics of the previously designed loops.

5.2.2 Stability Bound Generation

Stability bounds are also shown on the Nichols chart. The stability bounds are used to insure stability to measured system uncertainty. They also provide additional robustness to unmeasured system uncertainty. Stability is guaranteed if the design of each control loop robustly satisfies the stability bounds [73]. The stability bounds are based upon the plant dynamics and do not include the dynamics associated with sound radiation. Therefore, the sound pressure level transfer function $G_R(j\omega)$ is not necessary for this development since it is not contained in the feedback loop. Thus,

the stability bounds are generated in the same manner as for a MIMO control system where the system output is used as feedback.

The block diagram for the MIMO control system utilized in this derivation is shown in Figure 5.3. The heavy solid lines represent the multi-channel nature of the system. For a two-input-two-output diagonal controller the block diagram in Figure 5.3 can be expanded as in Figure 5.4. In Figure 5.4 $G_{w1}(s)D_1(s)$ and $G_{w2}(s)D_2(s)$ represent the point accelerations of the plate at the feedback sensor locations due to the turbulent flow excitation. $Y_1(s)$ and $Y_2(s)$ are the point accelerations of the plate which are used as feedback by the diagonal controller composed of $G_{c1}(s)$ and $G_{c2}(s)$. The point force inputs to the plate are $U_1(s)$ and $U_2(s)$. The plant dynamics from the point forces inputs to the acceleration feedback signals are given by the $G_{U_{ij}}(s)$ transfer functions.

In this work a sequential loop design methodology is utilized [73]. With this method, stability bounds are developed for each of the q loops in the controller. The transfer function relating the disturbance to the system output is given by

$$\{T_Y(s)\} = [[I] + [G_U(s)][G_C(s)]]^{-1} \{G_W(s)\} \tag{5.10}$$

where, $[G_U(s)]$, $[G_C(s)] \in S^{q\times q}$ and $[G_W(s)] \in S^{q\times 1}$. With the assumption that $\det[G_U(s)] \neq 0$, the plant inverse $[G_U^{-1}(s)]$ is used to write Equation 5.10 as

$$\left[[G_C(s)] + [G_U^{-1}(s)]\right] \{T_Y(s)\} = [G_U^{-1}(s)]\{G_W(s)\}. \tag{5.11}$$

By expressing the matrix multiplication as a summation and assuming a diagonal controller, the transfer function from the disturbance to the ith output is written as

$$\sum_{j=1}^{q} P_{ij}(s)t_j(s) + g_{c_i}(s)t_i(s) = \Theta_i \tag{5.12}$$

where g_{c_i} is the ith diagonal controller of $[G_C(s)]$ and

$$P_{ij}(s) = [G_U^{-1}(s)]_{ij} \tag{5.13}$$

$$\{\Theta(s)\} = [G_U^{-1}(s)]\{G_W(s)\}. \tag{5.14}$$

The transfer function associated with the first loop is given by

$$t_1 = \left(\frac{\Theta_1 - \sum_{j=2}^{q} P_{1j}t_j}{P_{11}}\right)\left(\frac{1}{1 + \frac{L_1^o}{G_{U_{11}}^o P_{11}}}\right). \tag{5.15}$$

From Equation 5.15 the stability of the first loop is guaranteed if the denominator has no poles in the right half plane. Therefore, for stability

$$\frac{L_1^o}{G_{U_{11}}^o P_{11}} \tag{5.16}$$

must satisfy the Nyquist criteria.

All previous loops are incorporated in the subsequent loops using Gauss elimination. Using this process, the transfer function associated with the second output is given by

$$t_2 = \left(\frac{[\Theta_2]^2 - \sum_{m=3}^{q}[P_{2m}]^2 t_m}{[P_{22}]^2}\right)\left(\frac{1}{1 + \frac{L_2^o}{G_{U_{22}}^o [P_{22}]^2}}\right) \tag{5.17}$$

where

$$[P_{2m}]^2 = P_{2m} - \frac{P_{21}P_{1m}}{P_{11} + g_{c_1}} \tag{5.18}$$

$$[\Theta_2]^2 = \Theta_2 - \frac{\Theta_1 P_{21}}{P_{11} + g_{c_1}} \tag{5.19}$$

Thus, for stability

$$\frac{L_2^o}{G_{U_{22}}^o [P_{22}]^2} \tag{5.20}$$

must satisfy the Nyquist stability criteria.

The Gauss elimination process can be written as a recursive relationship [74]. After closing k loops, the output transfer functions are given by

$$t_i = \frac{[\Theta_i]^{(k+1)} - \sum_{m=(k+2)}^{q} [P_{im}]^{(k+1)} t_m}{[P_{ii}]^{(k+1)} \left[1 + \frac{L_i^o}{G_{U_{ii}}^o [P_{ii}]^{(k+1)}}\right]}, i \geq k+1 \tag{5.21}$$

where

$$[P_{ij}]^{(k+1)} = [P_{ij}]^{(k)} - \frac{[P_{ik}]^k [P_{kj}]^k}{[P_{kk}]^k + g_{c_k}}, i, j \geq k+1 \tag{5.22}$$

$$[\Theta_i]^{(k+1)} = [\Theta_i]^{(k)} - \left[\frac{[P_{ik}]^k}{[P_{kk}]^k + g_{c_k}}\right] [\Theta_k]^k, i \geq k+1 \tag{5.23}$$

Thus, for the $k+1$ loop

$$\frac{L_i^o}{G_{U_{ii}}^o [P_{ii}]^{(k+1)}} \tag{5.24}$$

must satisfy the Nyquist stability criteria. The Nyquist stability point can be shifted by the magnitude and phase of $G_{U_{ii}}^o [P_{ii}]^{(k+1)}$ to determine a new stability point for the open loop transfer function L_i^o. Bounds are developed by placing an M circle bound at these stability points. By using these M circle bounds, additional robustness to unmeasured system uncertainty is obtained.

5.2.3 Control Effort Bound Generation

Finally, control effort bounds are developed to ensure that the controller does not saturate the actuator. The bounds are frequency domain restrictions on the closed loop control effort transfer function magnitude. Franchek [75] has shown that for a step input disturbance a time domain control effort constraint ($|u(t)| \leq \kappa$) can be directly guaranteed by a frequency domain bound ($|U(s)/D(s)| \leq \frac{\kappa}{\Lambda}$) where Λ is a constant used in the time to frequency domain conversion. Thus, by restricting the control effort transfer function magnitude, time domain restrictions are achieved.

The control effort bounds are developed similarly to the stability bounds. The frequency domain bounds for control effort are developed from the closed loop transfer

function by relating the disturbance $D(s)$ to the control effort $U(s)$. Using the general MIMO control system shown in Figure 5.3, the transfer function from the disturbance to the control effort is given by

$$\{T_U(s)\} = -\left[[I] + [G_C(s)][G_U(s)]\right]^{-1}[G_C(s)]\{G_W(s)\}. \tag{5.25}$$

Using the controller inverse $[G_C^{-1}(s)]$ each loop is isolated and the transfer function is written as

$$\left[[G_C^{-1}(s)] + [G_U(s)]\right]\{T_U(s)\} = \{G_W(s)\}. \tag{5.26}$$

The transfer function from the disturbance to the ith controller output is written as

$$\sum_{j=1}^{q} G_{U_{ij}}(s)t_{u_j}(s) + \frac{1}{g_i(s)}t_{u_i}(s) = G_{W_i}. \tag{5.27}$$

Using this equation the transfer function to the first controller output is given by

$$t_{u_1} = \left(\frac{G_{W_1} - \sum_{m=2}^{q} G_{U_{1m}}t_{u_m}}{G_{U_{11}}}\right)\left(\frac{L_1^o\mathcal{P}_1}{1 + L_1^o\mathcal{P}_1}\right) \tag{5.28}$$

where

$$L_1^o = G_{U_{11}}^o g_{c_1} \tag{5.29}$$

$$\mathcal{P}_1 = \frac{G_{U_{11}}}{G_{U_{11}}^o} \tag{5.30}$$

As before, Gauss elimination is used to isolate the control effort for subsequent loops. The transfer function for the second loop is given by

$$t_{u_2} = \left(\frac{[Z_2]^2 - \sum_{m=3}^{q}[G_{U_{2m}}]^2 t_{u_m}}{[G_{U_{22}}]^2}\right)\left(\frac{L_2^o\mathcal{P}_2}{1 + L_2^o\mathcal{P}_2}\right) \tag{5.31}$$

where

$$[G_{U_{2m}}]^2 = G_{U_{2m}} - \frac{G_{U_{21}}G_{U_{1m}}}{G_{U_{11}} + g_{c_1}^{-1}} \tag{5.32}$$

$$[Z_2]^2 = G_{W_2} - \frac{G_{W_1} G_{U_{21}}}{G_{U_{11}} + g_{c_1}^{-1}} \tag{5.33}$$

$$\mathcal{P}_2 = \frac{[G_{U_{22}}]^2}{G^o_{U_{22}}} \tag{5.34}$$

After the first k loops have been designed, the recursive relationship for the Gauss elimination process is used to write the output transfer functions as

$$t_{u_i} = \frac{[Z_i]^{(k+1)} - \sum_{m=(k+2)}^{q} [G_{U_{im}}]^{(k+1)} t_{u_m}}{[G_{U_{ii}}]^{(k+1)}} \left[\frac{\mathcal{P}_i L_i^o}{1 + \mathcal{P}_i L_i^o} \right], i \geq k+1 \tag{5.35}$$

where

$$[G_{ij}]^{(k+1)} = [G_{U_{ij}}]^{(k)} - \frac{[G_{U_{ik}}]^k [G_{U_{kj}}]^k}{[P_{U_{kk}}]^k + g_{c_k}}, i, j \geq k+1 \tag{5.36}$$

$$[Z_i]^{(k+1)} = [Z_i]^{(k)} - \left[\frac{[G_{U_{ik}}]^k g_{c_k}}{1 + [G_{U_{kk}}]^k g_{c_k}} \right] [Z_k]^{(k)}, i \geq k+1 \tag{5.37}$$

$$\mathcal{P}_i = \frac{[G_{U_{ii}}]^{k+1}}{G^o_{U_{ii}}(s)} \tag{5.38}$$

From the control effort transfer function equations (Equation 5.28, 5.31, and 5.35), the control effort constraint

$$|\{U(s)\}| \leq \{\kappa\}. \tag{5.39}$$

can be satisfied. However, the subsequent control loops have not been closed so each t_{u_m} is unknown. Therefore, the triangle inequality is used with Equations 5.28, 5.31, and 5.35 to find the control effort bounds for loop 1, 2, and i as

$$\left| \frac{\mathcal{P}_1 L_1^o}{1 + \mathcal{P}_1 L_1^o} \right| \leq \frac{|[G_{U_{11}}]^{(k+1)} \kappa_1|}{|G_{W_1} D(s)| + \sum_{m=2}^{q} |G_{U_{1m}} \kappa_m|} \tag{5.40}$$

$$\left| \frac{\mathcal{P}_2 L_2^o}{1 + \mathcal{P}_2 L_2^o} \right| \leq \frac{|[G_{U_{22}}]^2 \kappa_2|}{|[Z_2]^2 D(s)| + \sum_{m=3}^{q} |[G_{U_{2m}}]^2 \kappa_m|} \tag{5.41}$$

$$\left[\frac{\mathcal{P}_i L_i^o}{1+\mathcal{P}_i L_i^o}\right] \leq \frac{|[G_{U_{ii}}]^{(k+1)}\kappa_i|}{|[Z_i]^{(k+1)}D(s)| + \sum_{m=(k+2)}^{q}|[G_{U_{im}}]^{(k+1)}\kappa_m|}, i \geq k+1 \qquad (5.42)$$

respectively. The inequality expressions of Equations 5.40, 5.41, and 5.42 give an M circle bound on the open loop transfer function $L_k(\alpha, j\omega)$ for each ω. As with the performance bounds, $\mathcal{P}$ is used to shift the bound in magnitude and phase so that it becomes an amplitude bound on the nominal open loop transfer function, $L_k^o(\alpha_o, j\omega)$. In this way a nominal open loop transfer function is loop shaped to satisfy shifted bounds associated with the various uncertainty, rather than loop shaping multiple transfer functions associated with the various uncertainty to satisfy a single bound.

5.2.4 Composite Bounds

The inverted M circle bounds associated with sound pressure level reductions (Equation 5.7), the Nyquist stability M circle bounds (Equations 5.16 5.20, and 5.24), and the M circle bounds associated with control effort limitations (Equations 5.40, 5.41, and 5.42) are combined to form the design region used in the loop shaping process. A typical design region for a single frequency is shown in Figure 5.5. The dashed line is the performance bound associated with the reduction of the sound pressure level. At the frequency associated with this bound, the open loop must have a greater magnitude than the bound. The solid lines are the control effort and stability bounds. At the frequency associated with these bounds, the open loop must lie outside the bounds. Therefore, to satisfy sound pressure level reductions, stability, and control effort limitations, the open loop must lie in the shaded design region at the frequency for which these bounds were developed. The bounds are developed over a wide range of frequencies. By satisfying the most restrictive bounds, the bounds associated with the intermediate frequencies will also be satisfied.

5.3 Optimization of Actuator Position

In many control problems, the type and location of actuators and sensors utilized by the active controller are constrained. However, in some structural excitation problems, such as the flow induced structural radiation of sound problem, there is flexibility in these parameters. Using the model developed for active control of flow induced structural sound radiation, the effect of locating the actuator and sensors at various positions on the structure can be evaluated. As a result, it is possible to optimize the actuator and sensor locations to achieve the best possible control with the least amount of control effort.

In this investigation the actuator and sensor locations were optimized using the analytical model developed in Chapter 3. The optimization is performed without designing the specific controllers (G_{C_m}). The optimization procedure was used to find the locations where the natural plant dynamics have high gain in the frequency regions where low sensitivity is required. In this way, the plant will provide the dynamics useful for achieving the performance goals. Since the frequency domain controller design approach can utilize the beneficial plant dynamics, the controller gain and order can be reduced and the desired performance achieved.

From Equation 5.4 the closed loop sound pressure $R(s)$ is small at the frequencies where the open loop transfer functions L_m given by

$$L_m = G_U(\alpha, j\omega) F_m G_{C_m}(j\omega) H_m \tag{5.43}$$

are large. Since each F_m is a function of the control actuator location and each H_m is a function of the sensor location, the actuator and sensor locations can be used to increase $L_m(\alpha, j\omega)$. By increasing $L_m(\alpha, j\omega)$ in this way, sound pressure level reductions can be achieved with less controller gain. Thus, it is assumed that the controller will add additional dynamics such that robust stability, performance, and control effort restrictions are met. Using this assumption the optimization is used to minimize the function

$$O(j\omega) = \frac{G_R(j\omega)G_U(\alpha, j\omega)G_D(j\omega)D(j\omega)}{\sum_{m=1}^{q} \left|G^o_{U_{mm}}(\alpha_o, j\omega)\right|} \tag{5.44}$$

where

$$G^o_{U_{mm}}(\alpha_o, j\omega) = G_u(\alpha_o, j\omega)F_m H_m. \tag{5.45}$$

This function is minimized over the frequency range of interest. By minimizing Equation 5.44, the performance bounds given by Equation 5.7 will require less controller gain to achieve.

In this investigation Equation 5.44 was evaluated over the frequency range from 0 to 1000 Hz. A two-input-two-output controller configuration was considered. The parameters associated with the experimental setup were used in the system model. The flow speed was assumed to be 26.8 m/s (60 MPH) and the sensors were constrained to be co-located with the actuators. The plate was partitioned into an eleven by eleven grid. Equation 5.44 was evaluated for the various combination of actuator locations. Due to the symmetries in the problem, it was not necessary to evaluate all of the combinations.

The ten best actuator/sensor locations are shown in Table 5.1. Each of the combinations includes a location near the center of the plate. Furthermore, four of the best five combinations include the location in the center of the plate $(0.229m, 0.165m)$. Locating an actuator/sensor pair near the center of the plate gives beneficial plant characteristics for controlling the strongly radiating first mode. The best three actuator/sensor pair locations are shown on the plate in Figure 5.6.

5.4 Experimental Investigation

The frequency domain controller method outlined in the previous section was used to design controllers for an experimental investigation of flow induced structural

radiation of sound. The experimental setup described in Chapter 3 was used for the investigation. Both SISO and MIMO controllers were designed and implemented.

5.4.1 SISO Experimental Investigation

A single-input-single-output controller consisting of a point force control actuator and an accelerometer feedback sensor was designed. The accelerometer and control actuator were located at the center of the plate. At this location the sensor and actuator couple with the odd-odd modes of the plate. As indicated in the results of Chapter 3, significant sound is radiated at the odd-odd modes of the plate. Microphones were mounted inside the box to evaluate the controller performance. A spherical coordinate system with the origin at the center of the plate was used to position the microphones (Figure 3.4). Performance specifications were placed on a single microphone located at R=54.6 cm, $\phi = -40^o$, and $\theta = 33^o$.

5.4.1.1 SISO Controller Development

The uncertainty in the system was measured experimentally. The system uncertainty was measured for various operating conditions. Broadband noise was input to the control shaker and used to measure the plant transfer function $\{H\}G_U(\alpha, s)\{F\}$. The uncertainty associated with different flow speeds was found. Speeds of 0, 26.8, 35.8, 40.2 m/s (0, 60, 80, and 90 MPH) were used. The transfer functions were measured on two separate days to include variation due to changes in environmental conditions. The Bode plot of the measured responses are shown in Figure 5.7. Variations in the plant transfer function increase with frequency. The magnitude of the plant transfer function varied as much as 8 dB and the phase varied by as much as 88 degrees in the 100-2000 Hz region. Furthermore, the magnitude varied by 0.7 dB, 2.0 dB, and 3.7 dB and the phase varied by 13^o, 27^o, and 30^o at the first, fourth, and eighth resonance, respectively. The variation between the transfer functions measured on the two days was greater than the variations due to the flow speed.

Performance bounds were developed using Equation 5.7. For this case a nominal transfer function was not used in the loop shaping process. As a result, the bounds were not shifted by $\mathcal{P}$. Each of the measured transfer functions is plotted independently on the Nichols chart. This is possible because the stability bound does not shift for a SISO controller. Furthermore the effect of the plant variations is easier to see when each loop is plotted on the Nichols chart.

For this application, the largest sound pressure levels occur at the resonances of the plate. Thus, the sound pressure level at the control location was specified to be less than 32 dB, 10 dB, and 8 dB at the first, fourth, and eight modal resonance (981, 3542, 5655 rad/s), respectively. Using Equation 5.7, the three performance bounds were calculated and are shown in Figure 5.8 as solid lines.

Stability bounds are developed on the Nichols chart from Equation 5.24 and used to insure stability for the measured system uncertainty. For a SISO controller design, Equation 5.24 reduces to the open loop transfer function $L(\alpha, j\omega)$. Therefore, the stability point is -1. By using an M circle constraint about this point, the closed loop transfer function magnitude is limited and additional robustness to unmeasured uncertainty is obtained. The M circle constraint is the complementary sensitivity bound

$$\left| \frac{L(\alpha, j\omega)}{1 + L(\alpha, j\omega)} \right| \leq A \tag{5.46}$$

For this controller design the stability constraint (A) was 5 dB for all frequencies. This guarantees a gain margin of 3.89 dB and a phase margin of 33 degrees. The bounds are shown as dashed lines in Figure 5.8.

Finally, control effort bounds are developed to ensure that the controller does not saturate the actuator. The control effort bounds were generated from Equation 5.40. For a SISO controller, the transfer functions in Figure 5.3 are related to those in the block diagram associated with the flow induced structural radiation of sound problem (Figure 5.2) by

$$G_{W_1} = \{H\}G_U G_D \tag{5.47}$$

and

$$G_{U_{11}} = \{H\}G_U\{F\}. \tag{5.48}$$

Therefore, for the SISO case, the control effort bound is written as

$$\left|\frac{L(\alpha, j\omega)}{1 + L(\alpha, j\omega)}\right| \leq \left|\frac{\kappa H_1 G_U(\alpha, j\omega) F_1}{H_1 G_U(\alpha, j\omega) G_D(j\omega) D(j\omega)}\right|. \tag{5.49}$$

For this application the control effort $U(s)$ was restricted to be less than 40 mV. The control effort bounds were less restrictive than the stability bounds at all frequencies. For this reason, the control effort bounds are not shown in Figure 5.8.

The performance bounds in Figure 5.8 require a large open loop gain (low gain on the sensitivity transfer function) at the natural frequencies of the plate. The frequency domain bounds for stability and control effort imposed a low gain condition on the complementary sensitivity transfer function at the off-resonance frequencies. Furthermore, the stability requirements based on the Nyquist stability criterion, require the gain of the open loop transfer function to be below unity for phases at and near multiples of $-180°$. These Nyquist stability points are shown in Figure 5.8 as dots.

The Nichols chart of the plant transfer function is shown in Figure 5.9. The resonances associated with the modes cause the loops in the plot. The phase associated with these loops is approximately 360 degrees. This large phase spread would violate the stability bounds. Traditional solutions use the controller to add phase lead to compensate for excessive lag due to the plant dynamics or to cancel the plant dynamics with controller dynamics. However, canceling the lightly damped plant dynamics is difficult for systems with uncertainty. Furthermore, this approach increases the controller order since additional controller dynamics are required to cancel potentially beneficial plant dynamics.

In this work an alternative method was devised and utilized. The controller was used to add additional phase lag such that the performance requirements are satisfied while also meeting the stability bounds. By adding phase lag, the frequencies regions of high gain due to the resonances of the plate can be placed between the Nyquist stability points. In this way the performance bounds which require a large open loop gain (low gain on the sensitivity transfer function) at the natural frequencies of the plate are achieved primarily with the plant dynamics. Furthermore, the frequency domain bounds for stability and control effort, which impose a low gain condition on the complementary sensitivity transfer function at the off-resonance frequencies, can also be achieved primarily with the plant dynamics. Thus, the natural dynamics of the plate produce the amplitude characteristics required by the bounds. Through the addition of phase lag, it was possible to take advantage of these natural dynamics of the system to minimize controller order and actuator requirements.

In this controller design the phase lag is achieved using a combination of poles and non-minimum phase zeros. The amplitude roll-up associated with the non-minimum phase zeros is attenuated by the amplitude roll-off of the complex poles. Therefore, the desired phase characteristic is achieved without decreasing the natural gain of the plant at the resonance. For single crossover systems, non-minimum phase zeros restrict the controller bandwidth thereby reducing the system performance. However for multiple crossover systems, this problem can be avoided. The penalty is that the sensitivity will be greater than one in the frequency regions were the phase is an odd multiple of 180 degrees. Because the system input is broadband, the regions of high sensitivity have worse closed loop performance than open loop performance. However, the bounds developed for this problem show that this is an acceptable sacrifice which enables control of sound at the higher frequencies.

Using this loop shaping process, a pair of complex poles at $\omega = 1500\ rad/sec, \zeta = 0.15$ and a pair of non-minimum phase complex zeros at $\omega = 2200\ rad/sec, \zeta = 0.2$ are used to add phase lag so that the first natural frequency ($\omega = 981$) is centered between the stability points at 180° and -180° degrees. The amplitude roll-up associated with

the non-minimum phase zeros is attenuated by the amplitude roll-off of the complex poles. Therefore, the desired phase characteristic is achieved without decreasing the natural gain of the plant at the resonance. Additional gain is achieved at the first natural frequency using a complex lead compensator composed of a pair of complex zeros at $\omega = 780\ rad/sec, \zeta = 0.6$ and a pair of complex poles at $\omega = 860\ rad/sec, \zeta = 0.2$ to meet the lower bound at $\omega = 981$. Similarly, the lower bound at the fourth natural frequency ($\omega = 3542$) is achieved by adding gain using a complex lead compensator composed of a pair of complex zeros at $\omega = 2500\ rad/sec, \zeta = 0.2$ and a pair of complex poles at $\omega = 3800\ rad/sec, \zeta = 0.4$. A non-minimum phase complex conjugate pair of zeros at $\omega = 5000\ rad/sec$, $\zeta = 0.1$ and a pair of complex poles at $\omega = 4000\ rad/sec, \zeta = 0.38$ are then used to add phase lag to place the resonance peak corresponding to the eighth mode ($\omega = 5655\ rad/sec$) between the stability points of -540^o and -900^o. In this way, the lower bound at the eighth natural frequency ($\omega = 5655$) is met. To roll-off the gain of the controller at high frequencies, an additional pair of complex poles are added at $\omega = 4000\ rad/sec$ with ζ=0.38. The resulting controller

$$G(s) = \frac{1.2[s^2/780^2+2(0.6)s/780+1][s^2/2200^2-2(0.2)s/2200+1]}{[s^2/860^2+2(0.2)s/860+1][s^2/1500^2+2(0.15)s/1500+1]} \frac{[s^2/2500^2+2(0.2)s/2500+1][s^2/5000^2-2(0.1)s/5000+1]}{[s^2/3800^2+2(0.4)s/3800+1][s^2/4000^2+2(0.38)s/4000+1]^2} \tag{5.50}$$

is tenth order with a DC gain of 1.2 dB. The plant transfer functions for each operating condition were augmented with the controller dynamics such that the bounds were achieved. The open loop and a few key frequency domain bounds are shown on an extended Nichols chart in Figure 5.10 as heavy solid lines. The frequencies associated with each bound and the corresponding frequency on the open loop transfer functions are labeled. Each of the bounds shown in Figure 5.10 has been satisfied. For this reason, the controller is expected to meet performance, stability, and control effort design criteria.

5.4.1.2 SISO Controller Results

The controller was implemented on a 166 MHz Pentium computer running Matlab Real Time Workshop. Keithley Metrabyte analog to digital and digital to analog cards were used. The sample rate of the controller was 20 kHz. A Wavetex 852 low-pass filter set at 5 kHz was used to prevent aliasing of the feedback signal.

The uncontrolled and controlled sound pressure level responses for the location to be controlled are shown in Figure 5.11 for a flow velocity of 35.8 m/s (80 MPH). The desired sound pressure levels of 32 dB, 10 dB, and 8 dB at the first, fourth, and eighth resonance were achieved. This corresponds to sound pressure level reductions of approximately 15 and 8 dB at the first and fourth resonance, respectively. The overall reduction across the 100-1000 Hz band is 3.7 dB. The control effort restriction of 40 mV was also achieved.

The acceleration at the feedback sensor location was decreased. The uncontrolled and controlled acceleration is shown in Figure 5.12 for a flow velocity of 35.8 m/s (80 MPH). The acceleration levels were decreased by approximately 20, 10, and 5 dB at the first, fourth, and eighth resonance respectively.

The sound pressure levels were measured at various locations inside the enclosure. The sound pressure level reductions over the 100-1000 Hz band are shown in Table 5.2. Control was achieved at each microphone. The sound pressure level at the control point $(54.6, -40°, 33°)$ for different flow velocities is shown in Table 5.3. The controller was robust to changes in velocity. The sound pressure level reductions were consistently between 3 and 4 dB over the 100-1000 Hz band and around 15 dB and 8 dB at the first and fourth resonance, respectively.

The open and closed loop plant transfer function magnitudes are shown in Figure 5.13. The closed loop transfer function magnitude is significantly different than the open loop transfer function. Over the 100-1000 Hz region the open loop and closed loop transfer function magnitudes differ by as much as 20 dB. In the frequency band near the first resonance, the magnitude of the closed loop transfer function is

approximately one. The difference in the open loop and closed loop transfer function magnitudes shows that the active controller significantly alters the dynamics of the plate.

The sensitivity magnitude is shown in Figure 5.14. At frequencies where the sensitivity value is less than one, there will be disturbance rejection. Where the sensitivity is greater than one there will be disturbance amplification. In Figure 5.14, the sensitivity is small in the frequency regions associated with the sound radiating resonances of the plate. Therefore, the acceleration in these frequency regions will be attenuated. In the frequency regions away form the resonances of the plate the sensitivity is greater than one and the feedback controller increases the acceleration.

It is interesting to compare the changes in the closed loop transfer function to those which would be achieved by additional passive damping. This analytical model developed in Chapter 3 was used to calculate the transfer functions and the sound pressure levels associated with different damping coefficients. The system parameters were those associated with the experimental investigation. A flow speed of 35.8 m/s (80 MPH) was considered. The magnitude of the plant transfer functions for $\zeta = 0.01$, $\zeta = 0.05$, and $\zeta = 0.1$ are shown in Figure 5.15. The vibration levels at the resonances of the plate are significantly reduced with the addition of damping. The increase of ζ from 0.01 to 0.1 results in a reduction of the acceleration by approximately 20 dB at the first, fourth, and eight modal resonance. However, the vibration levels at the off resonance frequencies were increased significantly.

The effect of passive damping on the sound pressure level was also evaluated using the analytical model. The results are shown in Figure 5.16. The sound pressure levels associated with turbulent flow for $\zeta = 0.01$, $\zeta = 0.05$, and $\zeta = 0.1$ are shown. The additional passive damping significantly reduces the sound pressure levels at the microphone location. The increase of ζ from 0.01 to 0.1 results in a reduction of the sound pressure level by approximately 20, 15, 20, and 15 dB at the first through fifth modal resonance frequencies. Slight sound pressure level increases were predicted at

off resonant frequencies. This is a good, but fundamentally different control approach than that accomplished using active control.

5.4.2 MIMO Experimental Results

A multiple-input-multiple-output controller consisting of two point force control actuators and two accelerometer feedback sensors was designed and implemented. As with the SISO investigation, microphones were mounted inside the box to evaluate the controller performance. However in this case, the sound pressure level at two microphone locations is to be controlled to illustrate that the performance specifications for multiple microphone locations can be achieved. Control of more than one microphone is achieved by meeting multiple, multiple-input-single-output sound pressure level reduction bounds. The first microphone was located at R=50.7 cm, $\phi = 90^o$, and $\theta = 17.6^o$. The second microphone location to be controlled was the same as that used in the SISO investigation (R=54.6 cm, $\phi = -40^o$, and $\theta = 33^o$).

Each of the accelerometers was co-located with a control actuator. The locations of the sensors and actuators were selected using the optimization of Equation 5.44 as described previously. The uncontrolled sound pressure level associated with the second microphone location was utilized in the optimization. The radius of the shakers prevented the best two sets of actuator/shaker location combinations from being utilized. Thus, the third set of locations in Table 5.1 were utilized. The first actuator/sensor pair was located in the center of the plate. The second pair was located at $(a/3, b/2)$ where a and b are the longitudinal and lateral length of the panel respectively. This location allows control of some of the even-odd modes of the structure. For example, the (2,1) mode can be controlled with this sensor/actuator location.

5.4.2.1 MIMO Controller Development

A MIMO controller was developed for the wind noise problem using the controller design methodology previously described. As with the SISO investigation, the

experimental facility was utilized to measure the system uncertainty for various operating conditions. A broadband noise input was used to measure the transfer function $G_U(\alpha, s)$. The uncertainty associated with different flow speeds was found. Speeds of 0, 35.8, 40.2, 44.8, 51.5 m/s (0, 80, 90, 100, and 115 MPH) were used.

The Bode plot of the plant transfer function of the first loop $G_{U_{11}}(\alpha, s)$ is shown in Figure 5.17. As with the SISO investigation, variations in the plant transfer function increase with frequency. The magnitude of the plant transfer function varied as much as 11 dB and the phase varied by as much as 81 degrees in the 100-2000 Hz range. The magnitude varied by 2 dB, 3 dB, and 6 dB and the phases varied by 15^o, 34^o, and 27^o for the first, fourth, and eighth plate resonance, respectively.

The Bode plot of the plant transfer function of the second loop $G_{U_{22}}(\alpha, s)$ is shown in Figure 5.18. Over the 100-2000 Hz region the magnitude varied by as much as 12 dB and the phase as much as 84 degrees. The magnitude varied by 1 dB, 1 dB, and 4 dB and the phases varied by 17.5^o, 39^o, and 32^o for the first, second, and eighth plate resonance, respectively.

The Bode plot of the plant transfer function $G_{U_{12}}(\alpha, s)$ is shown in Figure 5.19. This is transfer function from the second shaker to the first accelerometer. Over the 100-2000 Hz region the magnitude varied by as much as 19 dB and the phase as much as 154 degrees. The calculation of the transfer function in the region of the fourth mode (564 Hz) is poor since the second shaker position is on a node line. Therefore, there is little input power to the plate at this frequency which results in a poor transfer function estimate.

The Bode plot of the plant transfer function $G_{U_{21}}(\alpha, s)$ is shown in Figure 5.20. This is transfer function from the first shaker to the second accelerometer. Over the 100-2000 Hz region the magnitude varied by as much as 27 dB and the phase as much as 161 degrees. The calculation of the transfer function in the region of the second mode (312 Hz) is poor. This is because the first shaker position is on a node line of the second (2,1) mode. As before, this causes small input power at this frequency

and a poor transfer function estimate. The uncontrolled sound pressure levels and acceleration levels were also measured for use in the controller development.

For this application, the sound pressure level was specified for a flow speed of 35.8 m/s (80 MPH). The sound pressure levels at both microphone locations are specified to be 38, 21, 18, and 15 dB at the first, second, fourth, and eighth resonance (958, 1964, 3542, 5655 rad/s), respectively. Equation 5.7 was used to calculate the performance bounds.

The performance bounds for the first loop associated with the microphones are shown in Figure 5.21. The bounds are the composite performance bounds associated with each of the two locations where the controlled sound pressure level is specified. The bounds associated with the first microphone are solid and those associated with the second microphone are dashed. At the first resonance (958 rad/s) the bounds for the two microphones are nearly identical. However, the second microphone has a significantly more restrictive bounds at the second resonance (1964 rad/s). This is understandable since the even longitudinal modes of the plate do not contribute significant sound at the location of the first microphone. This is a result of the fact that the first microphone location is located on the lateral midline of the plate. However, the sound pressure at the second microphone location has contributions from all modes. Therefore, there is larger uncontrolled sound pressure levels at these frequencies necessitating greater sensitivity reductions. The bounds associated with the first microphone at the fourth resonance (3542 rad/s) are more restrictive than those of the second microphone. However, at the eighth resonance (5655 rad/s) the bounds associated with the second microphone are more restrictive than those of the first microphone. By achieving the sensitivity reductions required by these bounds, the desired sound pressure level at both microphones will be achieved.

The Nyquist stability points were bounded by 6 dB M circles. The control effort $U(s)$ was restricted to be less than 1 V for each shaker. A few key composite frequency bounds associated with the first loop are shown on an extended Nichols chart in Figure 5.22. The frequencies associated with each bound are labeled. The dashed

bounds are sensitivity bounds requiring the open loop transfer function gain to exceed that of the bound. These bounds are most restrictive at the natural frequencies of the plate. This is a direct result of the fact that most of the sound is radiated at these frequencies. The solid bounds are complementary sensitivity bounds requiring the open loop transfer function to be outside and below the bounds.

From Figure 5.22 it can be determined that the bounds associated with 1964 rad/s cannot be satisfied. The lower bound exceeds the upper bound leaving no acceptable design region. The sound pressure level associated with 1964 rad/s is primarily a result of sound radiation due to the second mode of the panel. The sensor actuator pair of the first loop is located in the center of the plate and lies on a node line of the second mode of the panel. For this reason, large control effort is required to achieve the desired sound pressure level reductions at this frequency. The required control effort exceeds the control effort specifications. Therefore, an additional control loop is required to achieve sound pressure level reductions at this frequency.

The first loop was used to achieve as many performance bounds as possible without violating stability or control effort restrictions. A second loop was used to achieve the remaining performance bounds. The Nichols chart of the first loop with no controller dynamics is shown in Figure 5.23. As in the SISO controller design, the natural dynamics of the plate produce the amplitude characteristics required by the bounds. Furthermore, the resonances associated with the plant transfer function cause loops in the Nichols plot which cover a phase range of approximately 360 degrees. Therefore, as in the SISO controller design, the controller was used to add additional phase lag such that the regions of high gain associated with the resonances of the plate are placed between the Nyquist stability points. In this way the performance requirements are satisfied while also meeting both the stability and control effort bounds. As before, the phase lag was added using a combination of poles and non-minimum phase zeros.

Two pairs of non-minimum phase complex conjugate zeros at $\omega = 4500\ rad/sec$, $\zeta = 0.4$, a pair of complex poles at $\omega = 4500\ rad/sec, \zeta = 0.4$, and a pair of complex poles at $\omega = 4500\ rad/sec, \zeta = 0.5$ are used to add phase lag to the first open loop

transfer function. In this way the first and fourth resonance are separated in phase by approximately 360°. A complex lead compensator consisting of a pair of complex poles at $\omega = 700\ rad/sec$, $\zeta = 0.3$ and a pair of complex zeros at $\omega = 420\ rad/sec$, $\zeta = 0.8$ are used to add phase lead so that the first natural frequency ($\omega = 958\ rad/sec$) is centered between the bounds associated with the $\omega = 750\ rad/sec$ and $\omega = 1500\ rad/sec$ frequencies. The lightly damped poles also add gain so that the sensitivity bound at $\omega = 958\ rad/sec$ is achieved. A pair of complex poles is added at $\omega = 2400\ rad/sec$ with $\zeta = 0.7$. These poles are used to add phase lag to appropriately space the 4th mode ($\omega = 3542\ rad/sec$) between the stability points at $-180°$ and $-540°$. These poles also roll off the open loop gain so that the stability bounds at the higher order modes can be satisfied and sensor noise is attenuated. A complex lead compensator is used to add gain near the 4th resonance ($\omega = 3542\ rad/sec$). The complex poles are at $\omega = 2200\ rad/sec, \zeta = 0.5$ and the complex zeros are at $\omega = 2000\ rad/sec, \zeta = 0.7$. Using these dynamics, the sensitivity bound at $\omega = 3542\ rad/sec$ is satisfied. The resulting controller

$$G_{C_1}(s) = \frac{1.2[s^2/420^2+2(0.8)s/420+1][s^2/2000^2+2(0.7)s/2000+1]}{[s^2/700^2+2(0.3)s/700+1][s^2/2200^2+2(0.5)s/2200+1]} \frac{[s^2/4500^2-2(0.4)s/4500+1]^2}{[s^2/2400^2+2(0.7)s/2400+1][s^2/4500^2+2(0.4)s/4500+1]} \frac{1}{[s^2/4500^2+2(0.5)s/4500+1]} \tag{5.51}$$

is a tenth order controller with a DC gain of 1.2 dB. The open loop transfer function for the first loop is plotted in Figure 5.24 as a heavy solid line. The open loop transfer function satisfies all of the bounds except the sensitivity bound at 1964 rad/s. A Bode plot of the controller $G_{C1}(s)$ is shown in Figure 5.25. The controller transfer function is smooth since it does not include lightly damped dynamics.

The bounds associated with the second loop are shown in Figure 5.26. As before, the dashed bounds are sensitivity bounds and the solid bounds are complementary sensitivity bounds. After designing the first loop, the only significant performance bound left to be achieved is associated with sound radiation form the second mode. Therefore, the only sensitivity bound is at 1964 rad/s.

The same approach taken for the first loop is also used in the second loop. However, in this case phase lag is added between the second (1964 rad/s) and the eighth (5655 rad/s) resonances. This leaves the first and second resonances between the stability points of 180^o and -180^o and the higher resonances between the -180^o and -540^o stability points. Most of the phase lag is achieved using a lightly damped complex pole pair with $\omega = 3300\ rad/sec, \zeta = 0.15$. Additional phase lag is achieved using a non-minimum phase zero at $\omega = 6000\ rad/sec$. A complex lead compensator consisting of a pair of complex poles at $\omega = 5000\ rad/sec, \zeta = 0.45$ and a pair of complex zeros at $\omega = 4000\ rad/sec, \zeta = 0.3$ is used to add additional gain to the open loop near the eighth natural frequency of the plate. A pole at $\omega = 7000\ rad/sec$ is used to aid in rolling off the gain. The resulting controller for the second loop is

$$G_{C_2}(s) = \frac{3[-s/6000+1]}{[s/7000+1][s^2/3300^2+2(0.15)s/3300+1]} \cdot \frac{[s^2/4000^2+2(0.3)s/4000+1]}{[s^2/4500^2+2(0.5)s/4500+1][s^2/5000^2+2(0.45)s/5000+1]}. \tag{5.52}$$

The controller is seventh order with a DC gain of 3 dB. The open loop is shown in Figure 5.26 as a heavy solid line. As all of the bounds have been satisfied, there is no requirement for additional control loops. A Bode plot of the controller $G_{C2}(s)$ is shown in Figure 5.27. As with $G_{C1}(s)$, the controller transfer function is smooth and does not include lightly damped dynamics.

5.4.2.2 MIMO Controller Results

As with the SISO controller, a 166 MHz Pentium computer running Matlab Real Time Workshop was used for implementation. The sample rate of the controller was 15 kHz. This was the maximum sample rate that could be achieved for the given controller order. A Wavetex 852 low-pass filter set at 5 kHz was used to prevent aliasing of the feedback signal. QSC type 1080 amplifiers were used to amplify the signal from the controller. B&K type 4810 shakers were utilized as the control actuators and two Kistler 5130 accelerometers and amplifier systems were used for feedback. B&K 4130 microphones with B&K 2810 amplifiers were used to measure the sound pressure

level performance. Data was acquired using a Tektronix 2630 FFT analyzer. The schematic of the configuration is shown in Figure 5.28.

Closed loop stability was achieved over the full range of operation of the wind tunnel. The uncontrolled and controlled sound pressure level responses for the first microphone location to be controlled are shown in Figure 5.29 for a flow velocity of 35.8 m/s (80 MPH). The uncontrolled sound pressure level is broadband in nature. However, there are large sound pressure levels at the frequencies of the first and fourth modes of the plate. The largest sound pressure level response is approximately 50 dB at 151 Hz and is associated with sound radiation of the first mode of the plate. The sound pressure level associated with the fourth mode (570 Hz) is approximately 28 dB. The sound pressure levels radiated as a result of the second, third and fifth modes are substantially smaller than those of the first and fourth modes. The sharp peaks near 250 Hz are noise created by the operation of the wind tunnel and cannot be controlled.

The desired sound pressure levels of 38 dB, 21 dB, 18 dB, and 15 dB at the first, second, fourth, and eighth resonance were achieved. The sound pressure level reductions are approximately 14 dB, 3 dB, 8 dB, and 1 dB at the first, second, fourth, and eighth resonance, respectively. Due to the location of the shaker/accelerometer pairs, control of the third or the fifth modes was not achievable. However, it was known *a priori* that the sound radiation associated with these modes was small at the location to be controlled. The overall sound pressure level reduction across the 100-1000 Hz band is 6 dB.

The uncontrolled and controlled sound pressure level responses for the second microphone location to be controlled are shown in Figure 5.30 for a flow velocity of 35.8 m/s (80 MPH). The uncontrolled sound pressure level is similar to that of the first microphone except that there are significant sound pressure levels near the frequency of the second mode. The second mode (310 Hz) is associated with approximately 32 dB of sound pressure level. The sound pressure levels radiated as a result of the third and fifth modes are substantially smaller than those of the first, second, and fourth

modes. The third mode of the plate is the (1,2) mode and has a natural frequency of approximately 450 Hz while the fifth mode of the plate is the (2,2) mode and has a natural frequency of approximately 610 Hz.

The desired sound pressure levels of 38 dB, 21 dB, 18 dB, and 15 dB at the first, second, fourth, and eighth modal resonance were achieved. The sound pressure level reductions are approximately 14 dB, 13 dB, 8 dB, and 3 dB at the first, second, fourth, and eighth resonance, respectively.

A substantial decrease in the plate acceleration was also achieved. The controlled and uncontrolled acceleration for the first loop is shown in Figure 5.31. The acceleration is reduced by approximately 16 and 10 dB at the first and fourth resonance. The total acceleration reduction at this location is 7.2 dB across the 100-1000 Hz region. The controlled and uncontrolled acceleration for the second loop is shown in Figure 5.32. The acceleration is reduced by approximately 16 and 14 dB at the first and second resonance, respectively. In addition, the acceleration is reduced by approximately 5 dB across the 880-950 Hz region. The total acceleration reduction across the 100-1000 Hz region is 6.9 dB.

Time histories of the control effort were also measured for each of the control channels. The control effort for the first loop is shown in Figure 5.33. The maximum control effort used was approximately 0.6 volts. The control effort for the second loop is shown in Figure 5.34. The maximum control effort used was approximately 0.5 volts.

The sound pressure level reductions using the same controller were measured for various flow velocities. The sound pressure levels of the second microphone are shown in Table 5.4. The controller achieved substantial sound pressure level reductions at all flow velocities. Larger sound pressure level reductions were achieved at the higher flow speeds. For the highest flow speed 51.4 m/s (115 MPH), sound pressure level reductions of 15 dB, 15 dB, and 9 dB at the first, second, and fourth modal resonance were achieved.

The uncontrolled and controlled sound pressure levels at other microphone locations were also measured. An array of microphones in a plane parallel to the plate were used. The microphone locations were symmetrical and are shown in Figure 5.35. All microphone locations achieved sound pressure level reductions over the 100-1000 Hz band. The sound pressure level reductions at each of the microphones for flow velocities from 35.8 m/s (80 MPH) to 51.4 m/s (115 MPH) are shown in Table 5.5. *The smallest sound pressure level reduction achieved was 4.6 dB while the largest was 6.0 dB across the 100-1000 Hz band.* As shown previously in Figure 5.30, the largest sound pressure level reductions were achieved at the frequencies associated with the first, second, fourth, and eighth modes of the plate.

5.4.3 Controller Robustness Investigation

For application to the wind noise problem it is expected that the degree of uncertainty exhibited by the plant will exceed that measured in this investigation. The frequency domain controller design method allows for additional uncertainty by utilizing an M circle constraint about the stability point. It is desirable to determine the degree of excess uncertainty that the controller design can withstand. The MIMO controller design presented previously was used in this investigation.

To investigate additional uncertainty, distributed masses were added to the panel. Four different sets of mass were added to the panel. The plant transfer functions were measured for each set of additional mass. Additionally, the controlled and uncontrolled sound pressure levels for the MIMO controller were measured for each mass configuration.

The different mass configurations are shown in Figure 5.36. The masses represented as circles correspond to approximately 7 g each. The masses represented as squares were approximately 62 g each. Each mass set includes the masses from the previous set. For example, set three includes all the masses from sets one, two, and

three. The total mass added was 84, 168, 413, and 731 g for tests 1, 2, 3, and 4 respectively. Mass set 4 represents an increase of 40 percent in the mass of the plate.

The plant transfer functions were measured for each mass set for flow speeds of 0, 35.8, 40.2, 44.8, 51.5 m/s (0, 80, 90, 100, and 115 MPH). Although these plant transfer functions were measured, only the original plant transfer functions with no additional mass were used in the design of the controller. The transfer functions associated with $G_{U_{11}}$, $G_{U_{22}}$, $G_{U_{12}}$, and $G_{U_{21}}$ are shown in Figures 5.37, 5.38, 5.39, and 5.40, respectively. The additional mass lowers the plate resonances frequencies. The first, second, and fourth resonances were shifted by 20, 14, and 14 percent, respectively. The phase of $G_{U_{12}}$ and $G_{U_{21}}$ for mass set 4 was significantly different than for the other mass sets over the frequency range 500-1000 Hz.

The closed loop was found to be stable under the full range of flow speeds for all four sets of additional mass. The uncontrolled and controlled sound pressure level at the second microphone (R=54.6 cm, $\phi = -40^o$, and $\theta = 33^o$) are shown for mass sets 1, 2, 3, and 4 in Figures 5.41, 5.42, 5.43, and 5.44, respectively. The additional mass for sets 1, 2, and 3 did not reduce the performance significantly. Sound pressure level reductions of approximately 14 and 13 dB were achieved at the first and second resonance respectively. These reductions are similar to those achieved for the case with no additional mass. The reduction associated with the fourth mode, however, were less than those achieved with no additional mass. Furthermore, the sound pressure level was increased by approximately 5 dB in the frequency region just below the fourth resonance. The additional mass of set 4 significantly impacted the closed loop performance. The sound pressure level reductions were approximately 8 dB at the first and second resonance. These reductions are significantly less than those achieved previously. Furthermore, the sound pressure level associated with the fourth mode was increased by 4 dB.

The Nichols plot of the open loop transfer functions for loop one with no additional mass, mass set 2, and mass set 4 is shown in Figure 5.45. The open loop transfer functions for loop two with no additional mass, mass set 2, and mass set 4 is shown in

Figure 5.46. Although the added mass significantly shifts the frequencies where the resonances occur, the open loop phase at the resonance does not change significantly. Since the system resonances are utilized in the controller design to achieve a majority of the required open loop gain, the gain remains high in the frequency regions of these resonance. Therefore, sensitivity is low at the frequencies requiring disturbance rejection and the the performance bounds continue to be achieved. However, the controller dynamics are adding the phase lag at frequencies appropriate for a system with higher natural frequencies. Thus the open loop phase is larger than desired and the transfer functions are shifted to the right on the Nichols chart. However, the controller does not use lightly damped poles and zeros to add the necessary phase lag. Thus, the fact that the controller gradually adds phase lag results in open loop phase shifts which are small compared to the large changes in the resonance frequencies.

Although the phase shifts on the Nichols plot are less than the phase shifts in the resonance frequencies, they do impact controller performance. For example, the phase shift is responsible for the increase in the sound pressure level near the fourth resonance for mass set 4. The open loop plot for mass set 4, shown in Figure 5.45, is significantly closer to the stability point at -180^0 than the open loop plot for the original system. Therefore, the frequencies near the fourth resonance have sensitivities greater than one which cause the sound pressure level of the controlled case to be larger than those of the uncontrolled case.

If the controller were attempting to eliminate the plant dynamics or to add significant gain, feedback could occur which would destabilized the controller. The observed robustness is a result of the fact that the plant dynamics are utilized in the controller. The controller design methodology will have robust stability characteristics against parameter variations that uniformly alter the plant dynamics.

A significant plant variation associated with the turbulent flow induced sound radiation in aircraft is a result of pressure loading. The difference in pressure between the pressurized cabin and the atmospheric pressure varies significantly with altitude.

As altitude changes are made, the prestress of the panel changes which results in different system transfer functions.

The effect of in-plane forces on the response of a panel is evaluated using the modal approach presented in Chapter 3. The structural response of a plate with in-plane forces is given by Leissa [76] as

$$D_o\nabla^4 u + c\frac{\partial u}{\partial t} + m\frac{\partial^2 u}{\partial t^2} = f(x,y,t) + N_x\frac{\partial u^2}{\partial x^2} + 2N_{xy}\frac{\partial u^2}{\partial x \partial y} + N_y\frac{\partial u^2}{\partial y^2} \tag{5.53}$$

where N_x and N_y, are the in-plane forces in the x and y directions respectively and N_{xy} is the in-plane shearing force. If the shearing force is negligible and the boundary conditions are simply supported, the modal analysis method can be used to calculate the natural frequencies. The natural frequency of the rth mode is

$$\omega_r = \sqrt{\frac{D_o}{m}\left[\left(\frac{p\pi}{a}\right)^2 + \left(\frac{q\pi}{b}\right)^2\right]^2 + N_x\left(\frac{p\pi}{a}\right)^2 + N_y\left(\frac{q\pi}{b}\right)^2}. \tag{5.54}$$

For a pressure difference, the plate will be under tension. Thus, the in-plane forces will always be positive and the natural frequencies will be higher than those with no prestress.

Using the model developed in Chapter 3, the system transfer function was calculated for a plate with in-plane forces. N_x and N_y were taken to be 5000 N/m. A Bode plot of the original system transfer function and the system transfer function for the plate with prestress are shown in Figure 5.47. The first resonance is increased by approximately 32% and the fourth resonance is increased by approximately 10%. The change in the plant transfer function is similar to what was measured when additional mass was added. Therefore, the controller design methodology utilized in this work be able to accommodate parameter variations associated with changing pressure differentials.

5.5 Conclusions

In this chapter, active feedback control of the flow induced structural radiation of sound has been experimentally demonstrated. A frequency domain controller design method was utilized which simultaneously ensures stability, provides sound pressure level reductions, and avoids actuator saturation. The controller design involved a loop shaping procedure where the plant transfer functions are augmented with controller dynamics such that frequency domain bounds are achieved. By meeting these bound, robust closed loop performance is guaranteed.

By representing the performance, stability, and control effort criteria as bounds on the Nichols chart, their impact on the controller design process is apparent. The relationship between the number of required control loops and controller performance is also illustrated using this design method. When it is impossible to design a controller for a given application, the information on the Nichols chart can be used to determine which bound causes limitations and display the corresponding compromises that must be made.

The controller design method was experimentally verified. The performance objectives were achieved at multiple microphone locations over a wide range of flow speeds. Sound pressure level reductions of approximately 14, 13, 8, and 3 dB were achieved at the first, second, fourth, and eighth resonances, respectively. Approximately 5.5 dB of sound pressure level reductions were achieved across the 100-1000 Hz frequency range at multiple microphone locations for flow speeds from 35.8 to 51.5 m/s. There have been no other experimental active control investigations of this problem to which these results can be compared.

The use of sound pressure feedback was shown to introduce system delay which severely limits broadband feedback control. To overcome this difficulty, acceleration feedback was utilized. However, a method whereby sound pressure level reductions

are achieved at various microphone locations was devised. In this method the uncontrolled sound pressure levels were utilized in the controller design process to appropriately weight the acceleration feedback such that specified sound pressure level reductions were achieved.

In the controller design methodology the plant dynamics were utilized to achieve the desired control. This was accomplished by using controller lag to appropriately phase the resonances of the plate. To avoid decreasing the natural gain of the plant transfer function, the lag was achieved using combinations of non-minimum phase zeros and poles. With this technique multiple crossover frequencies were used to increase the bandwidth where control was achieved. The small controller DC gain and low controller order was a direct consequence of the ability of the design method to utilize beneficial plant characteristics.

Since the natural dynamics of the system were utilized in the controller design, it was possible to optimize the locations of the control actuators and sensors. This was accomplished by finding the locations which resulted in high plant transfer function gain in the frequency regions where sound pressure level reductions are required. It was found that one sensor/actuator location should be located near the center of the plate. In this way, control over the strongly radiating first mode is best achieved.

Finally, the controller design methodology was shown to be robust to large system uncertainty for cases where there is a uniform shift in the system resonances. The plant dynamics were modified by the addition of discretized mass. The closed loop was found to be stable with respect to perturbations in the natural frequencies of 20 percent. The system uncertainty associated with pressure differentials across the plate was shown to produce similar changes in the system transfer function. Thus, it is expected that this controller design methodology would effectively handle plant variations associated with a change in the altitude of an aircraft. The robustness was a direct consequence of the use of the plant dynamics in the controller design. Because the plant dynamics were utilized to provide the system gain, the open loop phase

shifts at the resonances are small compared to the large changes in the resonance frequencies.

Table 5.1 Optimized Actuator/Sensor Locations

Pair #	mean($O(j\omega)$)	1st Actuator/sensor	2nd Actuator/sensor
		(x,y) m	(x,y) m
1	1.536e-06	(0.229,0.165)	(0.267,0.165)
2	1.555e-06	(0.229,0.138)	(0.267,0.165)
3	1.564e-06	(0.229,0.165)	(0.152,0.165)
4	1.574e-06	(0.229,0.165)	(0.191,0.193)
5	1.593e-06	(0.229,0.165)	(0.152,0.138)
6	1.599e-06	(0.152,0.165)	(0.229,0.193)
7	1.599e-06	(0.229,0.138)	(0.191,0.193)
8	1.599e-06	(0.191,0.138)	(0.229,0.138)
9	1.603e-06	(0.191,0.165)	(0.191,0.193)
10	1.603e-06	(0.191,0.138)	(0.267,0.165)

Table 5.2 SISO Controller SPL at Error Mics (100-1000 Hz, 35.8 m/s)

Mic	Location (R(cm),ϕ,θ)	Reduction, dB(re 20e-6 Pa)
1	$(54.6, -40^o, 33^o)$	3.7
2	$(50.0, -32^o, 15^o)$	3.9
3	$(18.8, 142^o, 46.2^o)$	4.1
4	$(34.5, 63.4^o, 26.9^o)$	0.2
5	$(66.8, 60.8^o, 33.1^0)$	5.8

Table 5.3 SISO Controller SPL at Mic $(54.6, -40^o, 33^o)$ for Various Flow Speeds, dB(re 20e-6 Pa)

Flow Velocity	Reduction (100-1000Hz)	Reduction at 1st Mode
26.8 m/s (60 MPH)	3.2	13.0
35.8 m/s (80 MPH)	3.7	14.8
40.2 m/s (90 MPH)	3.8	16.3

Table 5.4 MIMO Controller SPL at Mic $(54.6, -40^o, 33^o)$ for Various Air Speeds, dB(re 20e-6 Pa)

Flow Velocity	Reduction (100-1000Hz)	Reduction at 1st Mode	Reduction at 2nd Mode	Reduction at 4th Mode
35.8 m/s (80 MPH)	4.3	13.2	12.6	8.1
40.2 m/s (90 MPH)	4.5	14.4	13.4	8.8
44.7 m/s (100 MPH)	4.5	14.1	13.7	9.1
49.1 m/s (110 MPH)	4.5	14.2	13.6	9.2
51.4 m/s (115 MPH)	4.6	14.8	14.8	9.4

Table 5.5 MIMO Controller SPL Reductions at Error Mics, dB(re 20e-6 Pa) (100-1000 Hz)

Mic Number	35.8 m/s	40.2 m/s	44.8 m/s	51.5 m/s
1	5.7	5.5	5.4	5.4
2	5.1	4.9	4.8	4.6
3	6.0	5.8	5.8	5.7
4	5.0	5.0	4.9	4.8
5	5.8	5.8	5.6	5.2
6	5.2	5.3	5.2	4.9
7	5.7	5.7	5.5	5.6
8	6.0	5.9	5.6	5.4
9	5.9	5.8	5.4	5.4
10	5.6	5.6	5.1	5.1
11	6.0	5.9	5.6	5.6

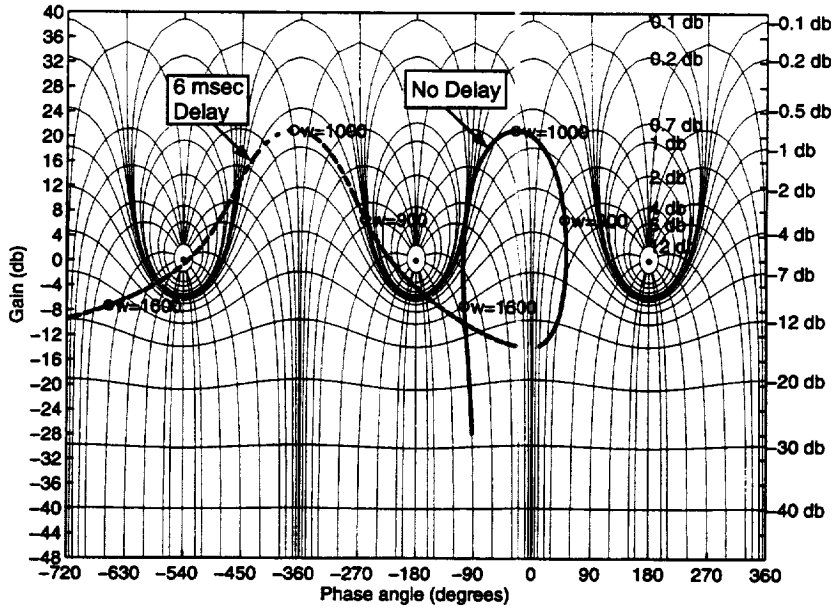

Figure 5.1 Nichols' Chart of Open Loop System with Delay

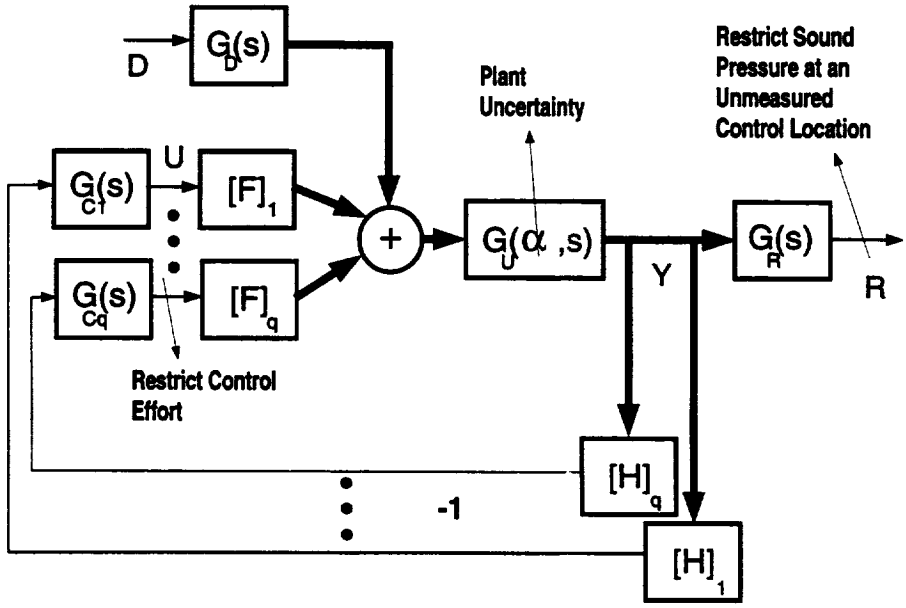

Figure 5.2 Turbulent Flow Induced Sound Radiation System Block Diagram

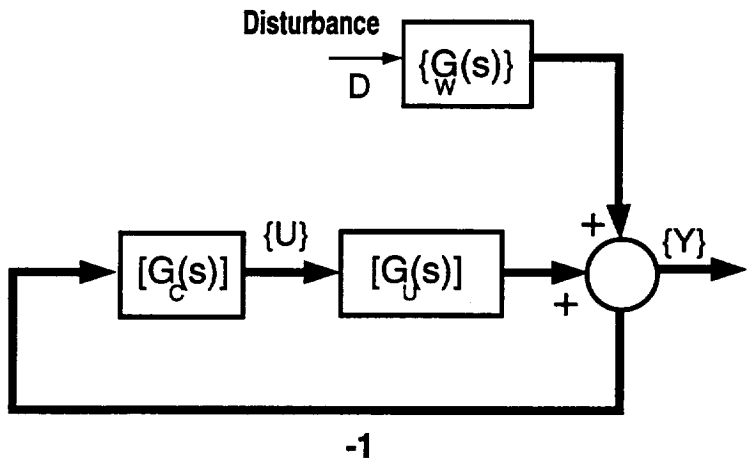

Figure 5.3 Standard Feedback Controller System Block Diagram

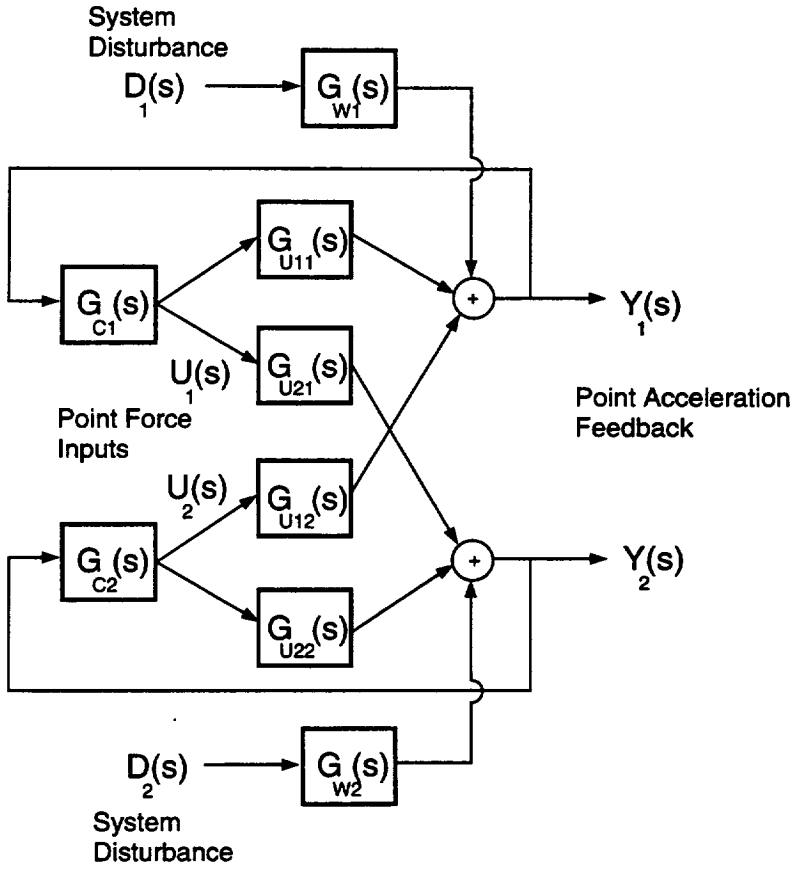

Figure 5.4 Two-Inputs-Two-Output Feedback Controller System Block Diagram

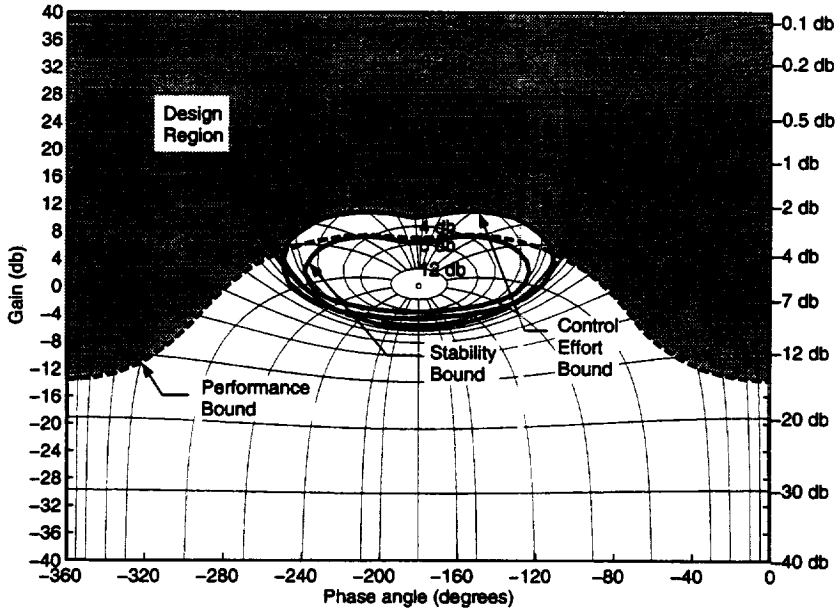

Figure 5.5 Composite Bound for a Specific Frequency

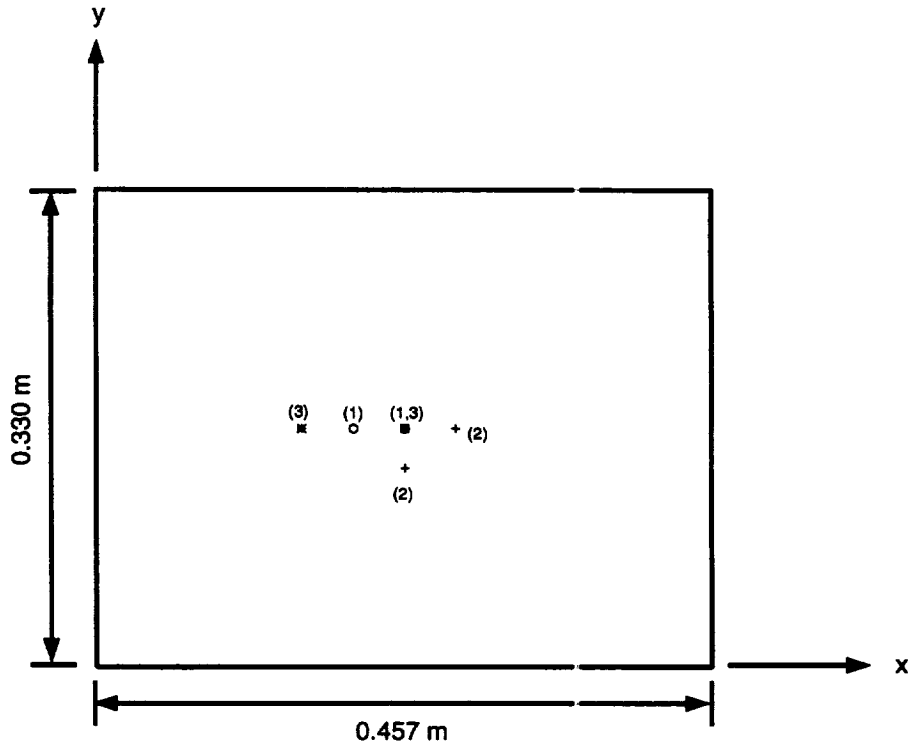

Figure 5.6 Optimized Actuator Locations; 1st o; 2nd +; 3d *

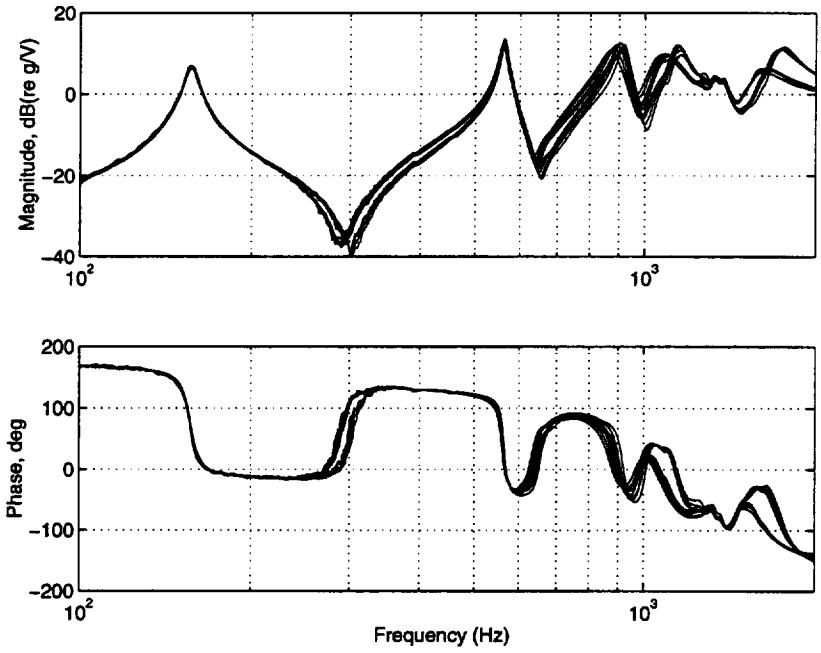

Figure 5.7 Bode Plot of Measured System Transfer Functions (SISO Controller)

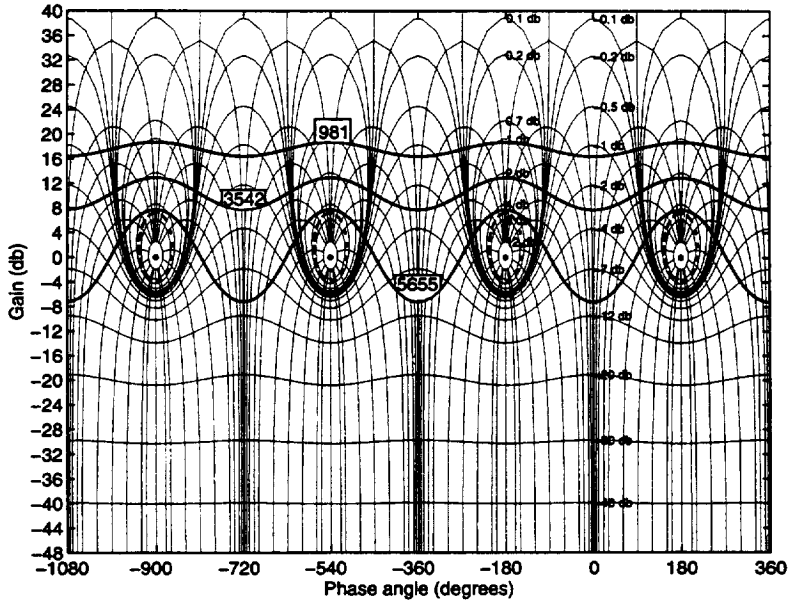

Figure 5.8 Nichols Chart of Bounds for the SISO Controller

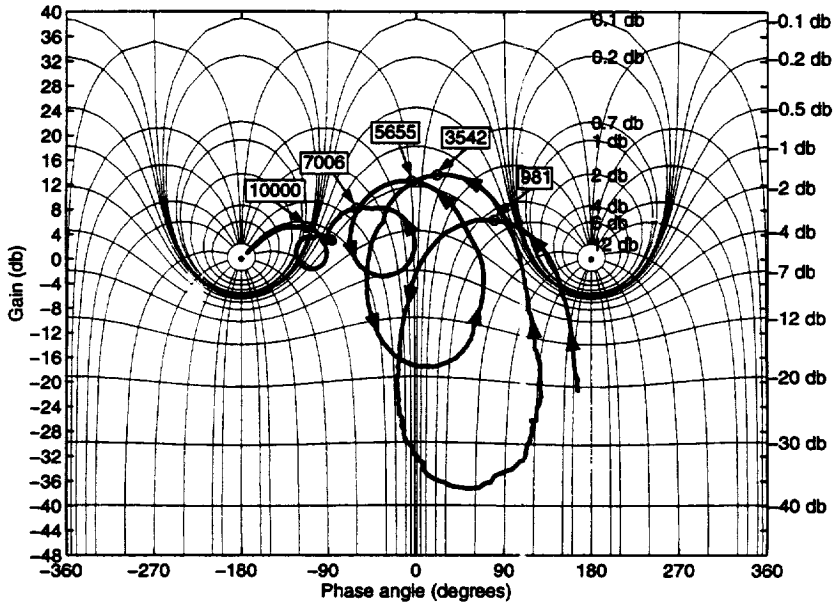

Figure 5.9 Nichols Chart of Open Loop with No Controller Dynamics (SISO Controller)

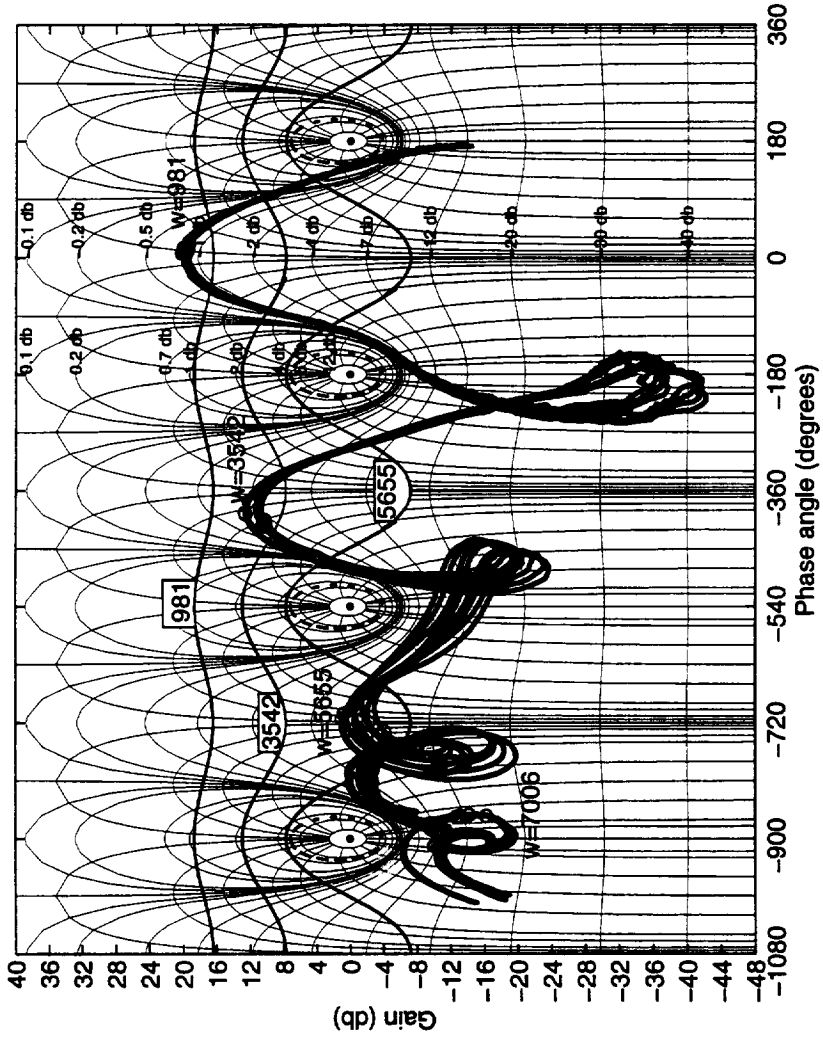

Figure 5.10 Nichols Chart of Open Loop with the Significant Bounds (SISO Controller)

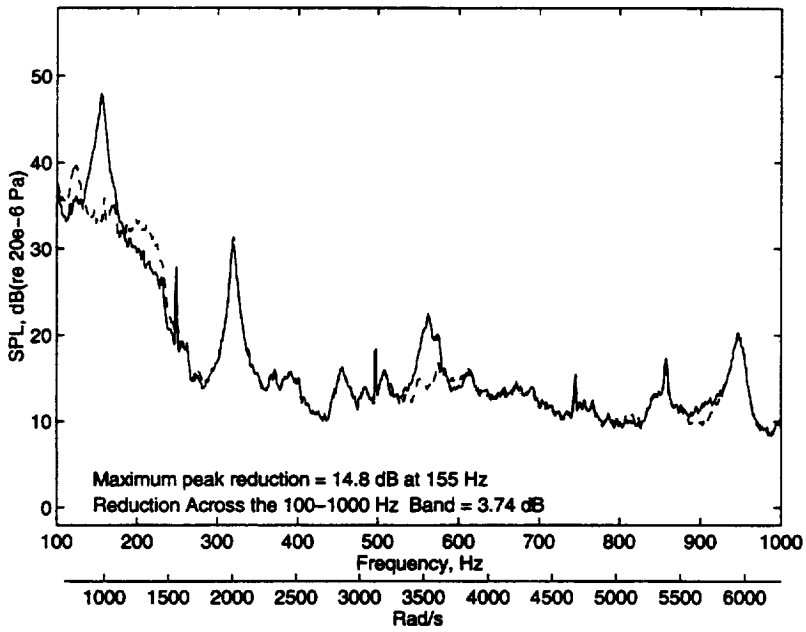

Figure 5.11 SPL for SISO Controller at Mic Location $(54.6, -40^o, 33^o)$; $(35.8\ m/s)$; Uncontrolled —; Controlled - -

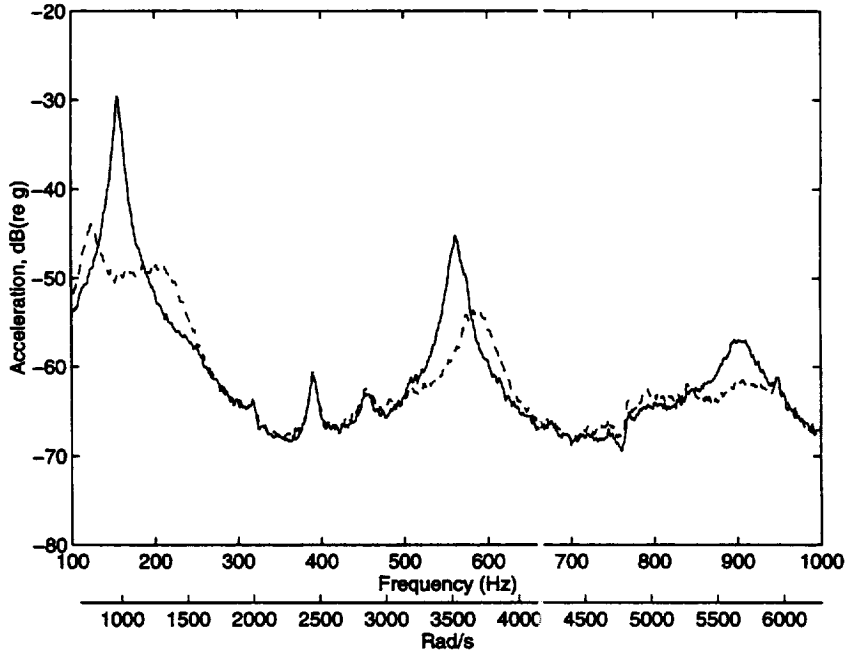

Figure 5.12 Sensor Acceleration for SISO Controller $(35.8\ m/s)$; Uncontrolled —; Controlled - -

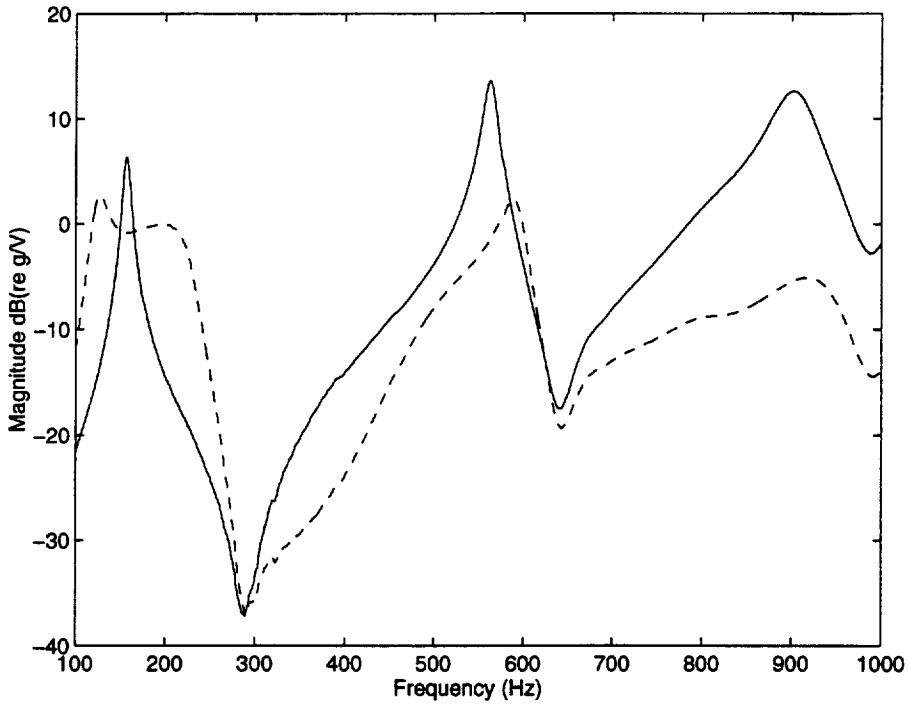

Figure 5.13 Open Loop and Closed Loop Transfer Function Magnitudes (SISO Controller); Open Loop —; Closed Loop - -

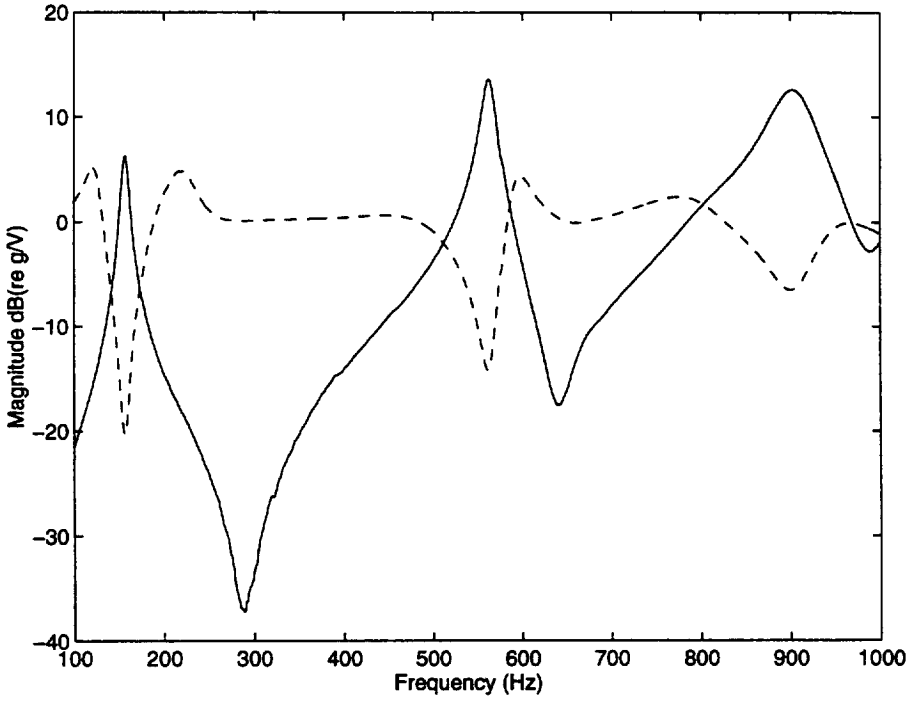

Figure 5.14 Sensitivity Magnitude (SISO Controller); Open Loop —; Sensitivity - -

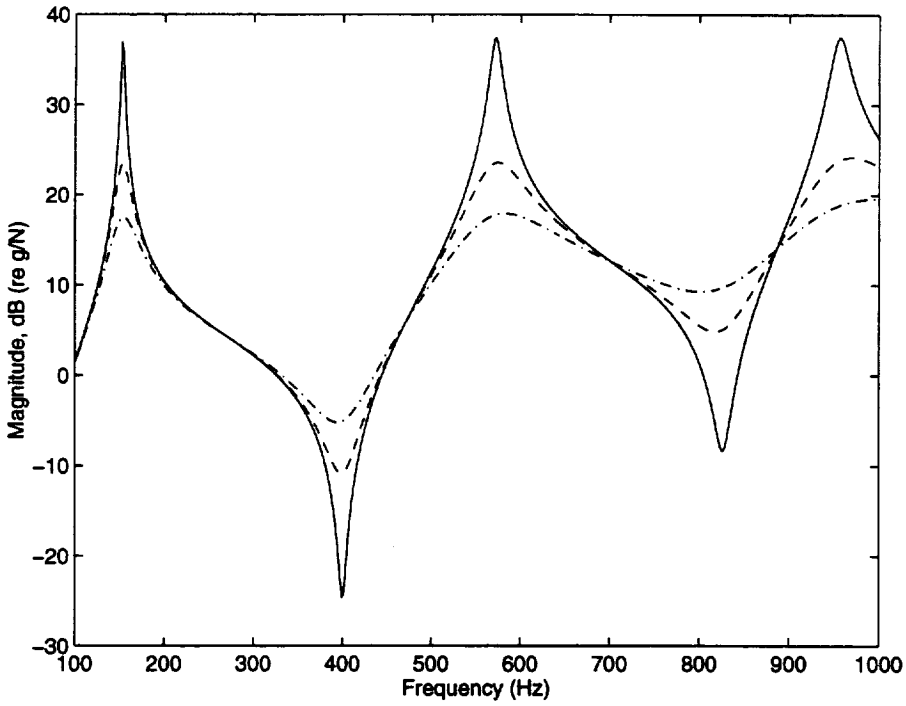

Figure 5.15 Plant Transfer Function for Different Damping Coefficients; $\zeta = 0.01$ —; $\zeta = 0.05$ - -; $\zeta = 0.1$ - ·

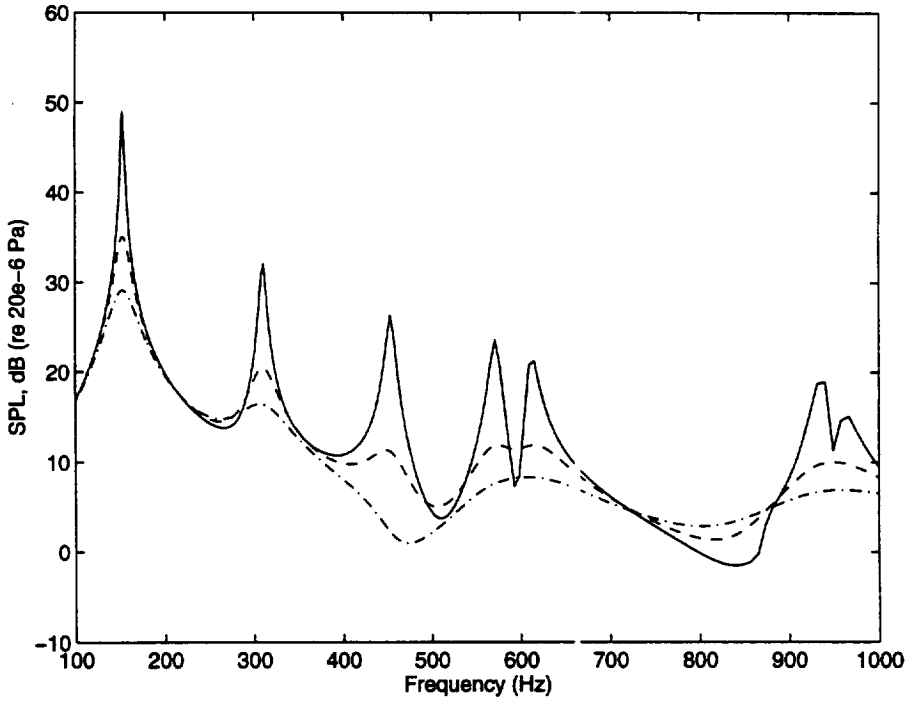

Figure 5.16 Sound Pressure Levels for Different Damping Coefficients; $\zeta = 0.01$ —; $\zeta = 0.05$ - -; $\zeta = 0.1$ - ·

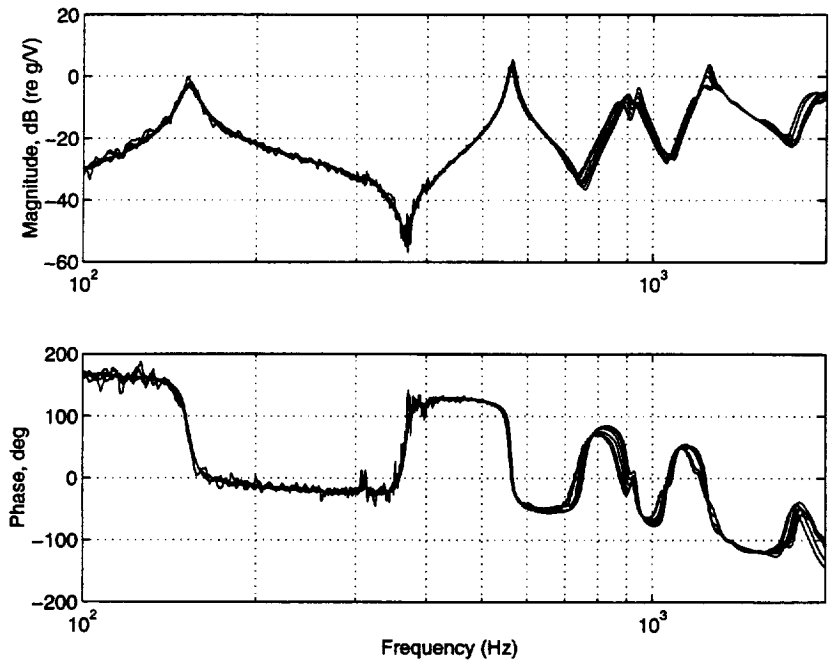

Figure 5.17 Bode Plot of Measured System Transfer Function $G_{U_{11}}$

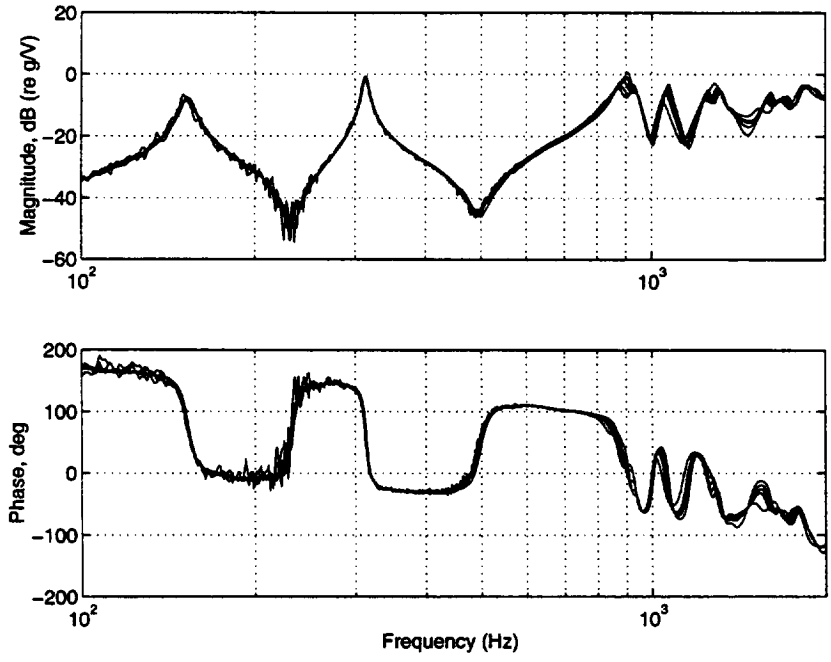

Figure 5.18 Bode Plot of Measured System Transfer Function $G_{U_{22}}$

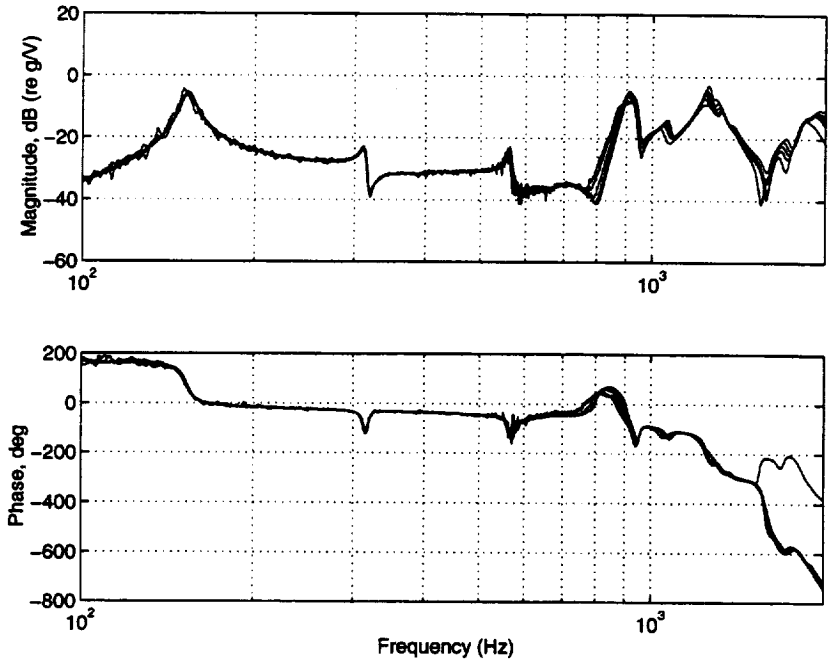

Figure 5.19 Bode Plot of Measured System Transfer Function $G_{U_{12}}$

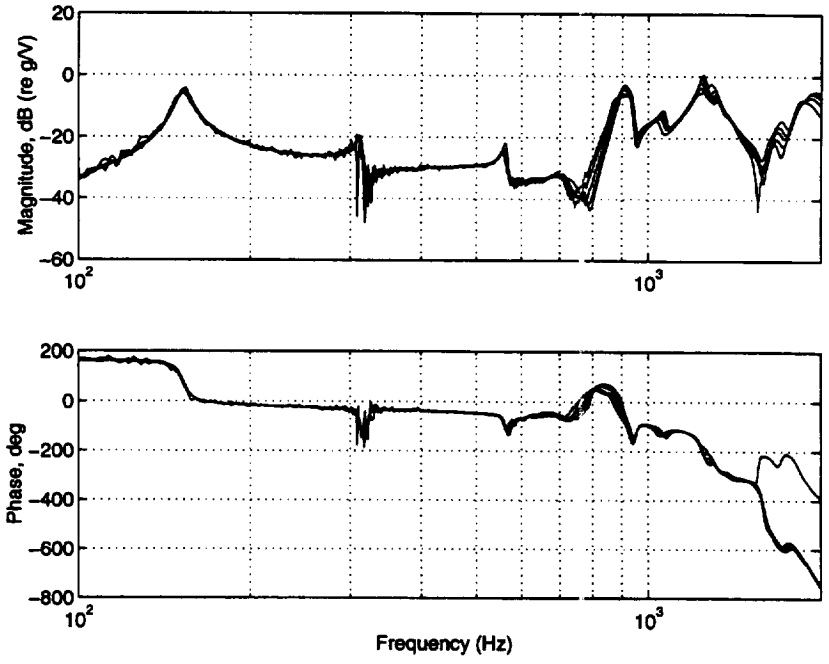

Figure 5.20 Bode Plot of Measured System Transfer Function $G_{U_{21}}$

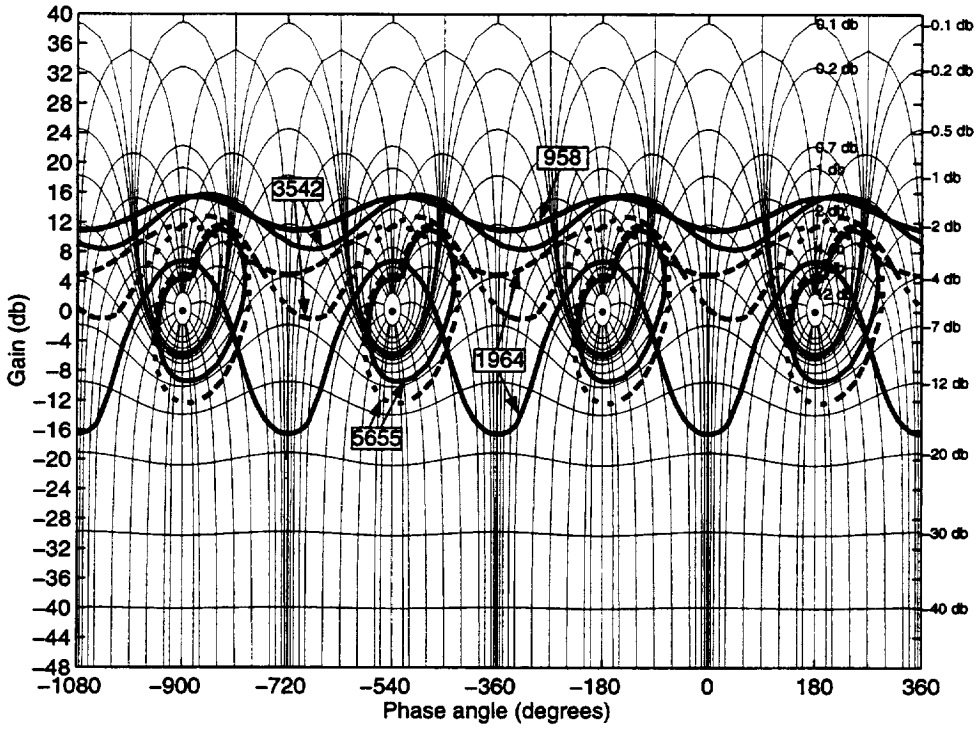

Figure 5.21 Performance Bounds for Microphones (MIMO Controller); Mic 1 (—);Mic 2 (- -)

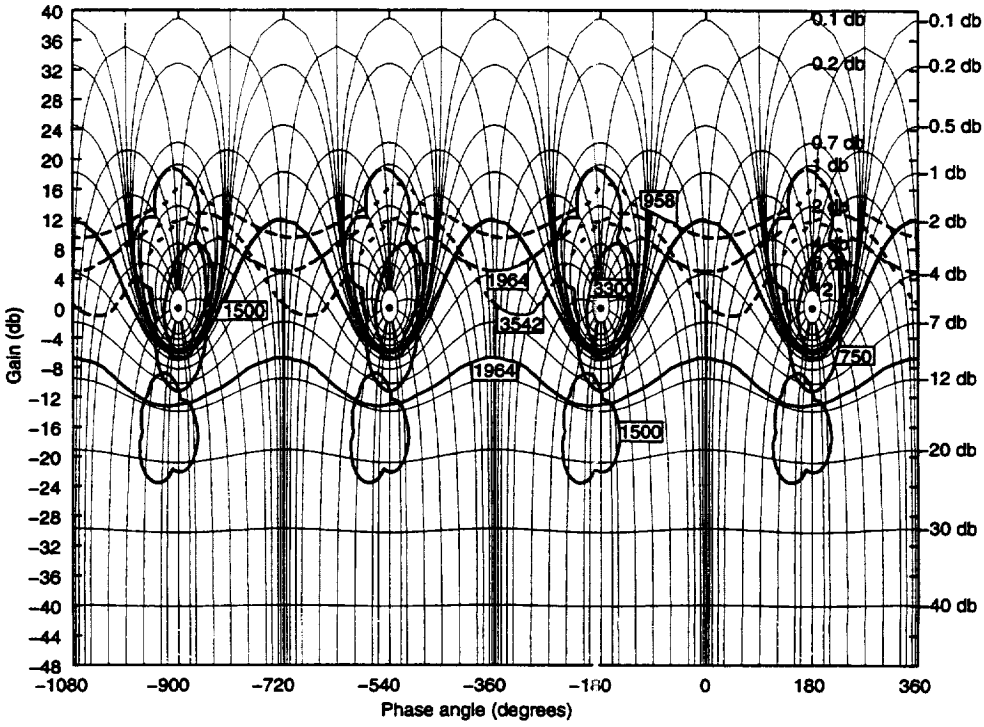

Figure 5.22 Nichols Chart of Bounds for Loop 1 (MIMO Controller)

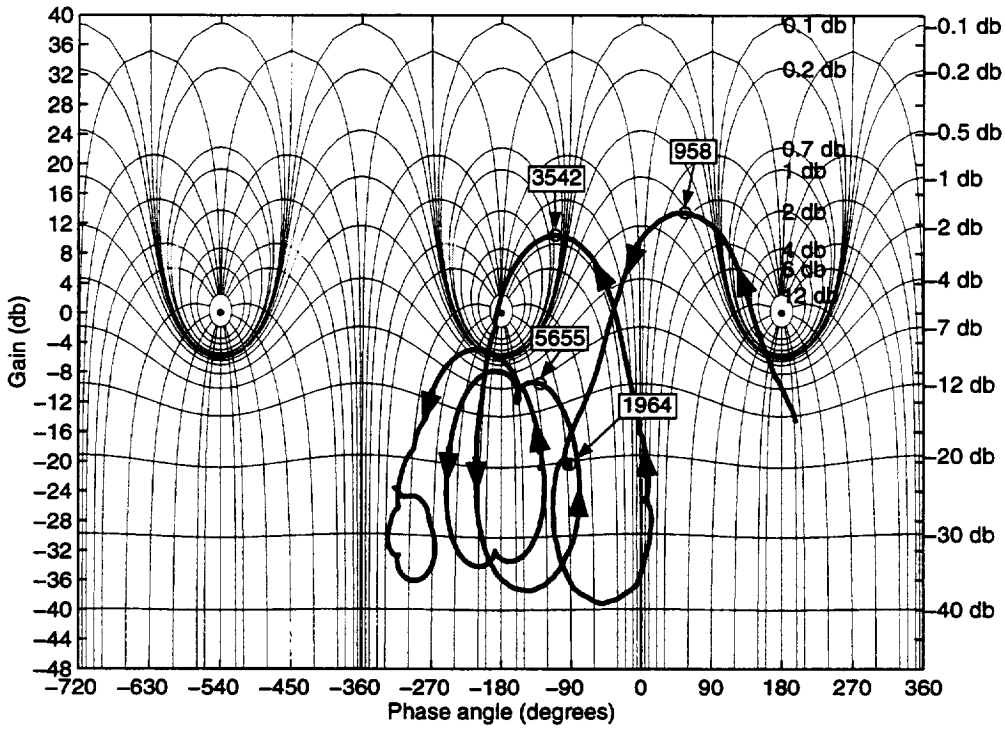

Figure 5.23 Nichols Chart of Open Loop 1 with No Controller (MIMO Controller)

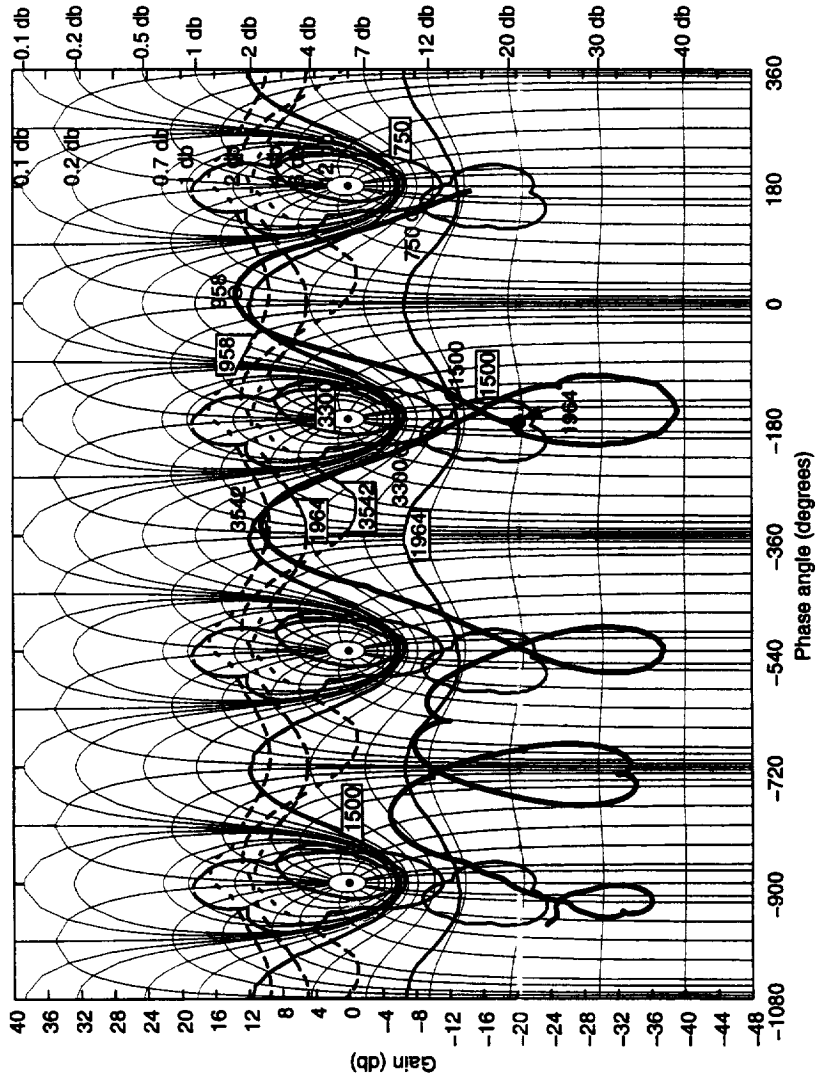

Figure 5.24 Nichols Chart of Open Loop Transfer Function and Bounds for Loop 1

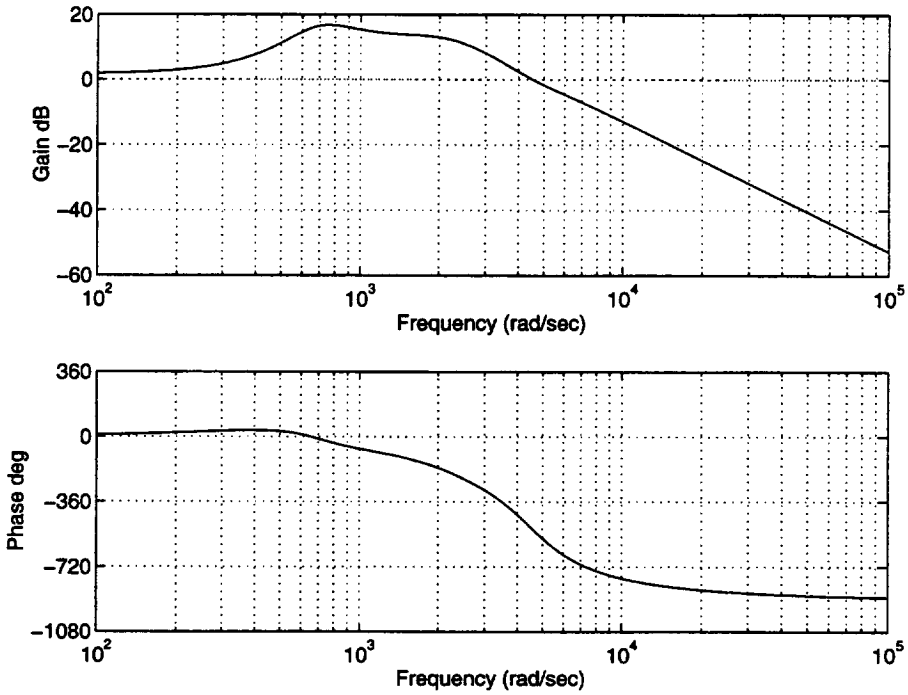

Figure 5.25 Bode Plot of Controller 1 (G_{C_1})

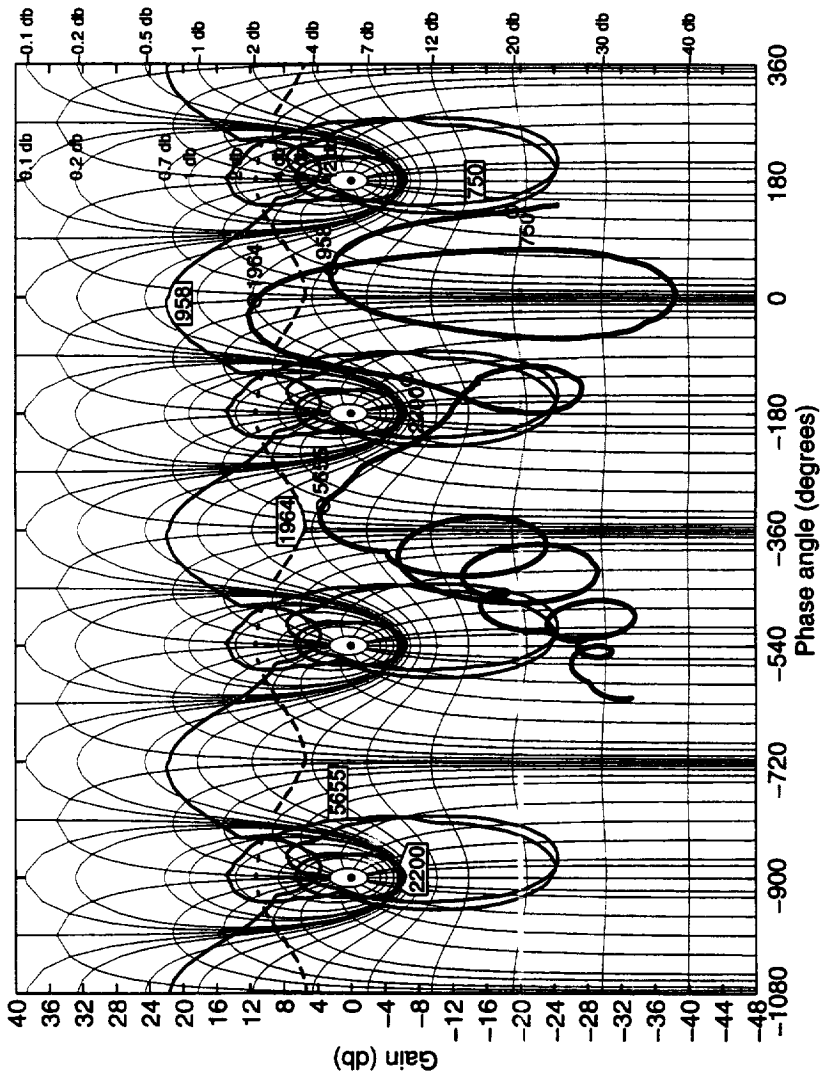

Figure 5.26 Nichols Chart of Open Loop Transfer Function and Bounds for Loop 2

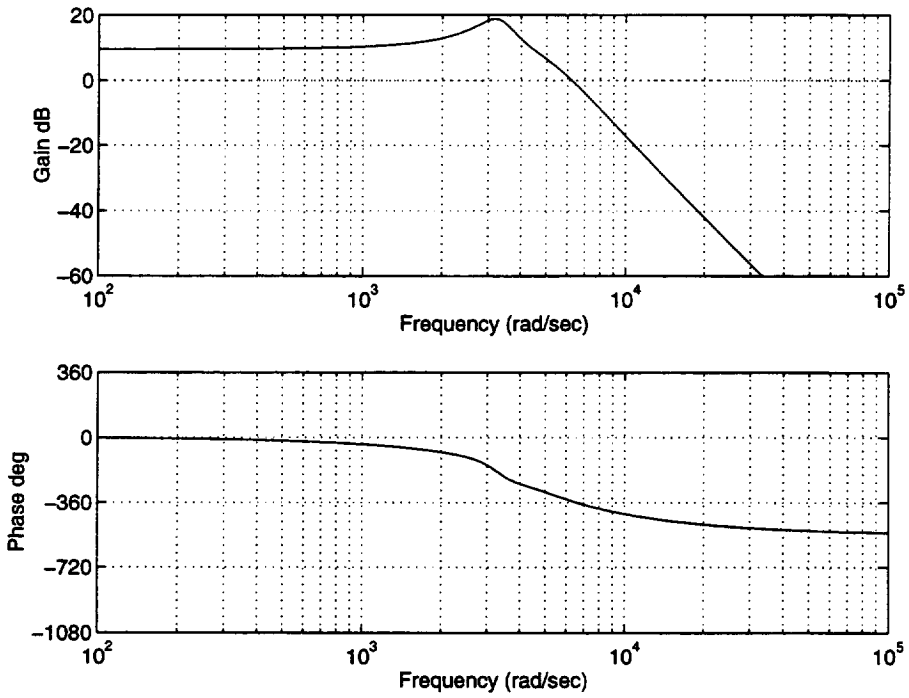

Figure 5.27 Bode Plot of Controller 2 (G_{C_2})

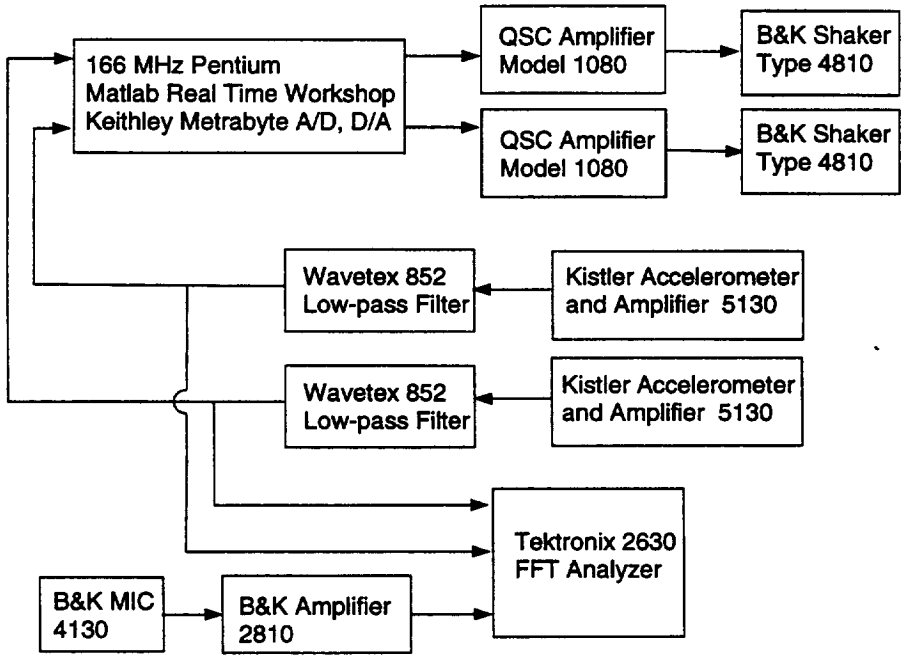

Figure 5.28 Schematic of Experimental System Configuration

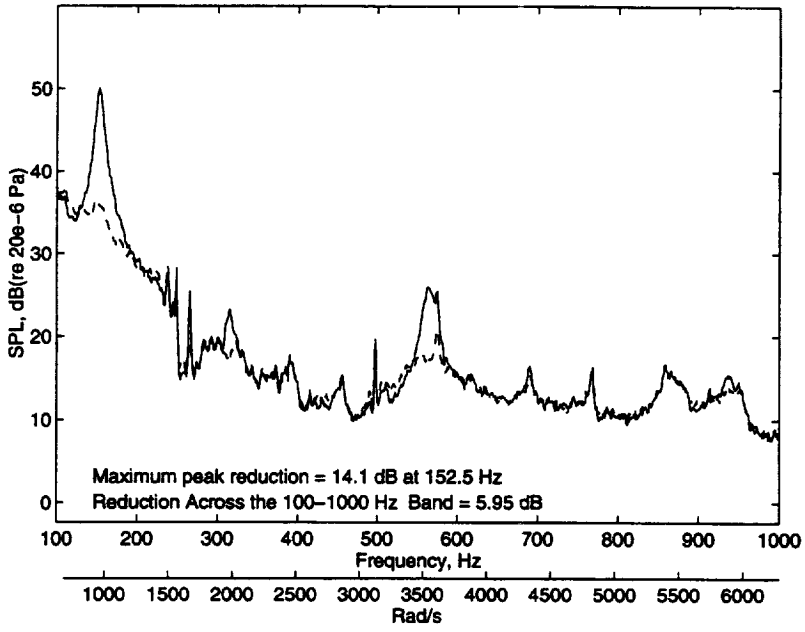

Figure 5.29 SPL at Mic 1 for MIMO Controller (35.8 m/s);
Uncontrolled (—);Controlled SPL (- -)

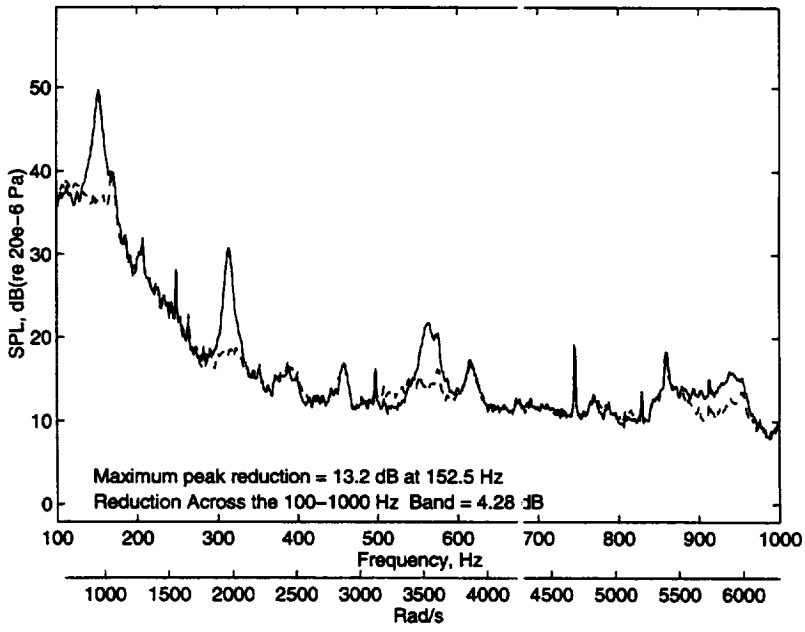

Figure 5.30 SPL at Mic 2 for MIMO Controller (35.8 m/s);
Uncontrolled (—);Controlled SPL (- -)

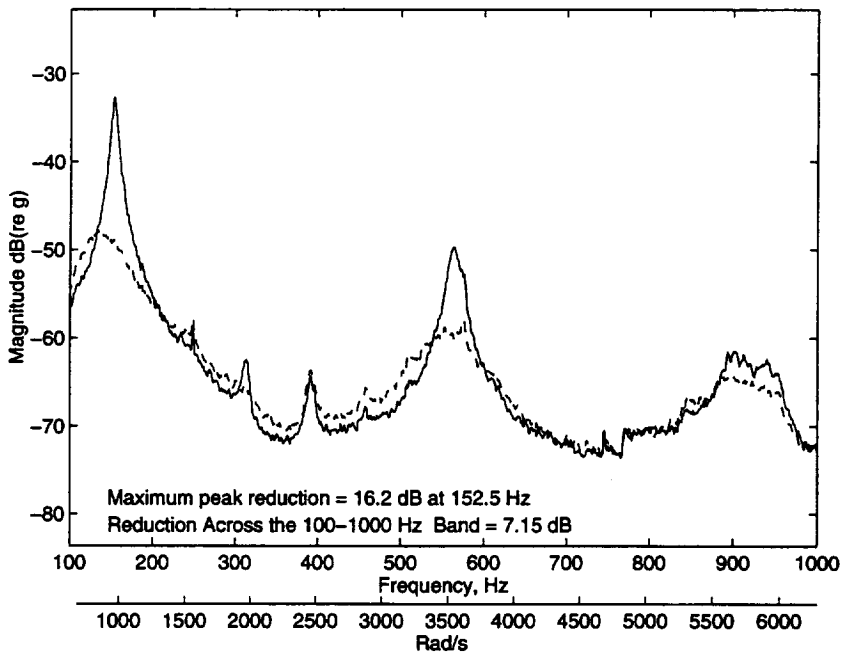

Figure 5.31 Acceleration at Accel. 1 for MIMO Controller (35.8 m/s); Uncontrolled (—);Controlled SPL (- -)

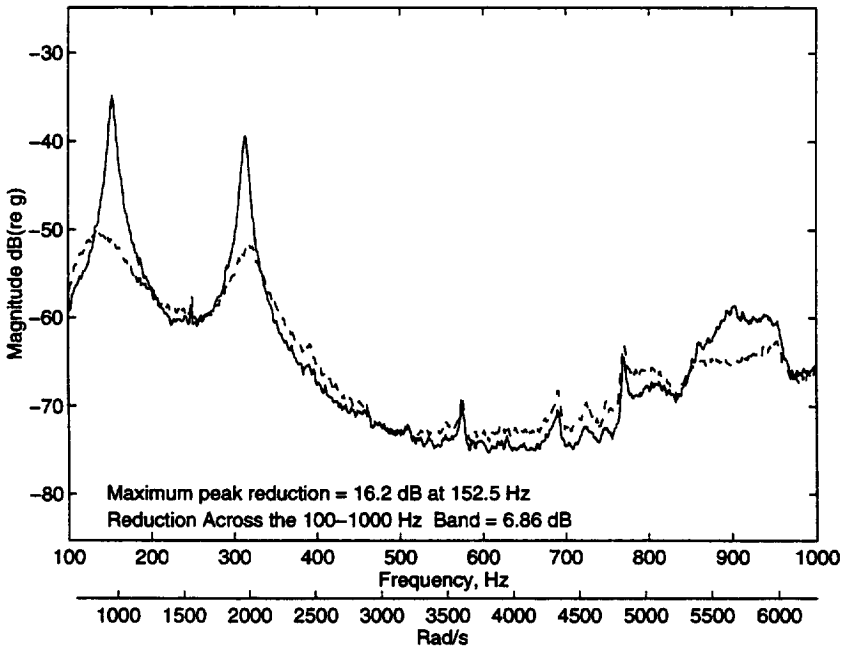

Figure 5.32 Acceleration at Accel. 2 for MIMO Controller (35.8 m/s); Uncontrolled (—);Controlled SPL (- -)

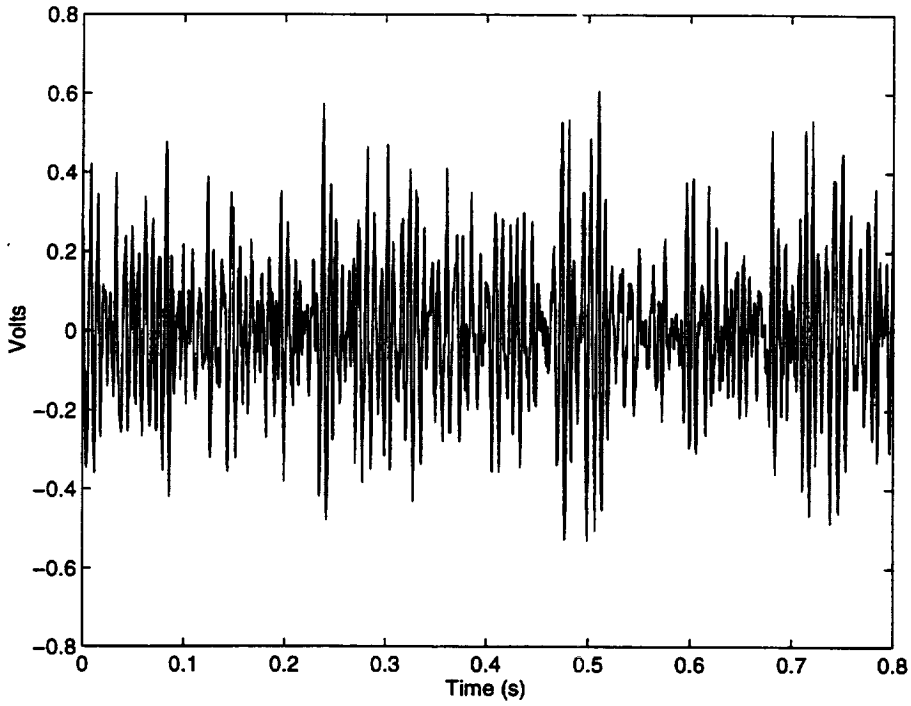

Figure 5.33 Time History of Control Effort for G_{C_1} (35.8 m/s)

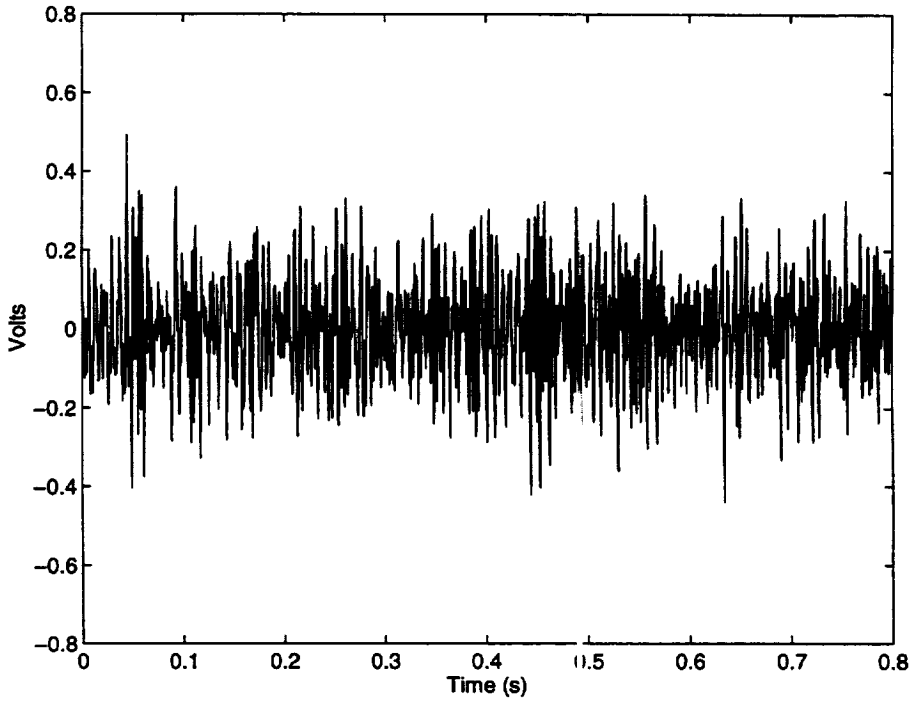

Figure 5.34 Time History of Control Effort for G_{C_2} (35.8 m/s)

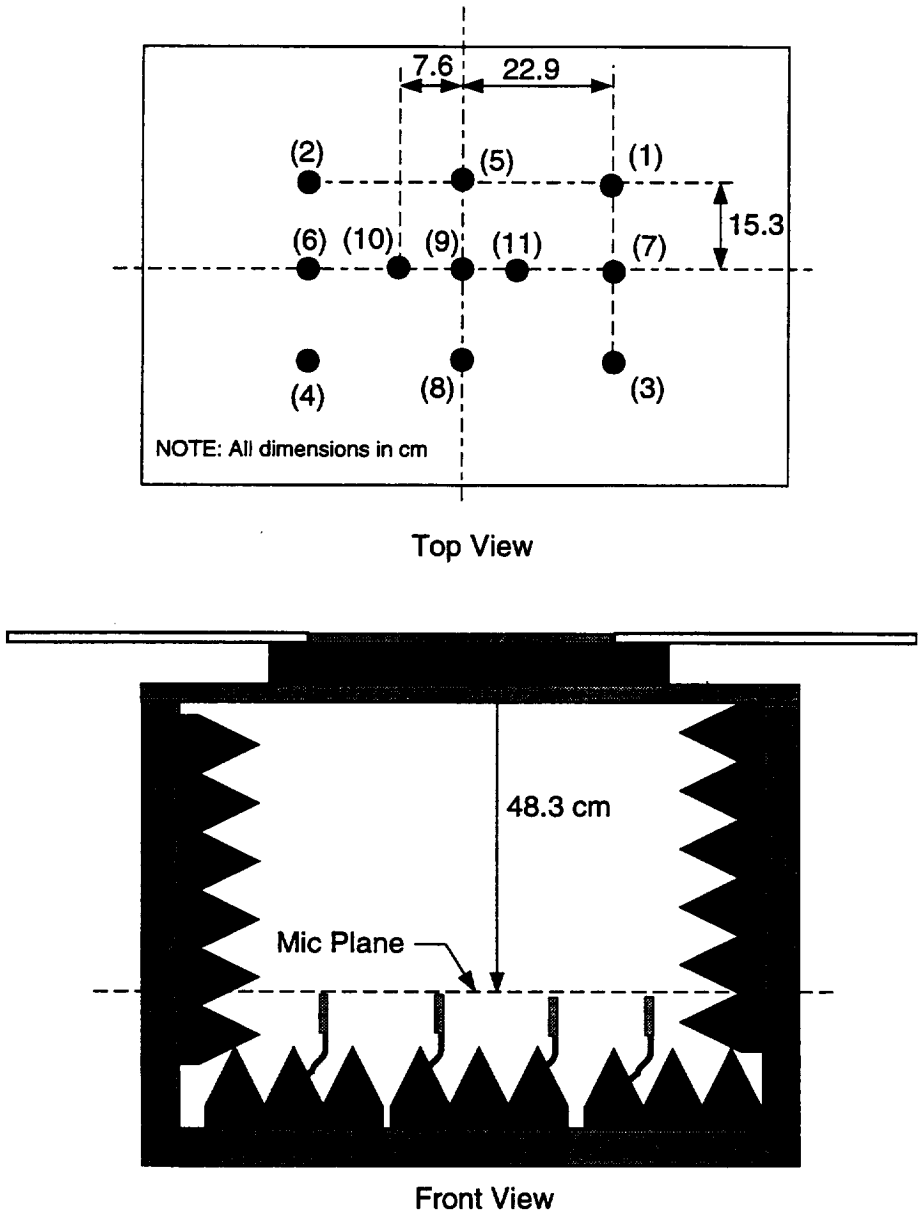

Figure 5.35 Location of Microphones for MIMO Investigation

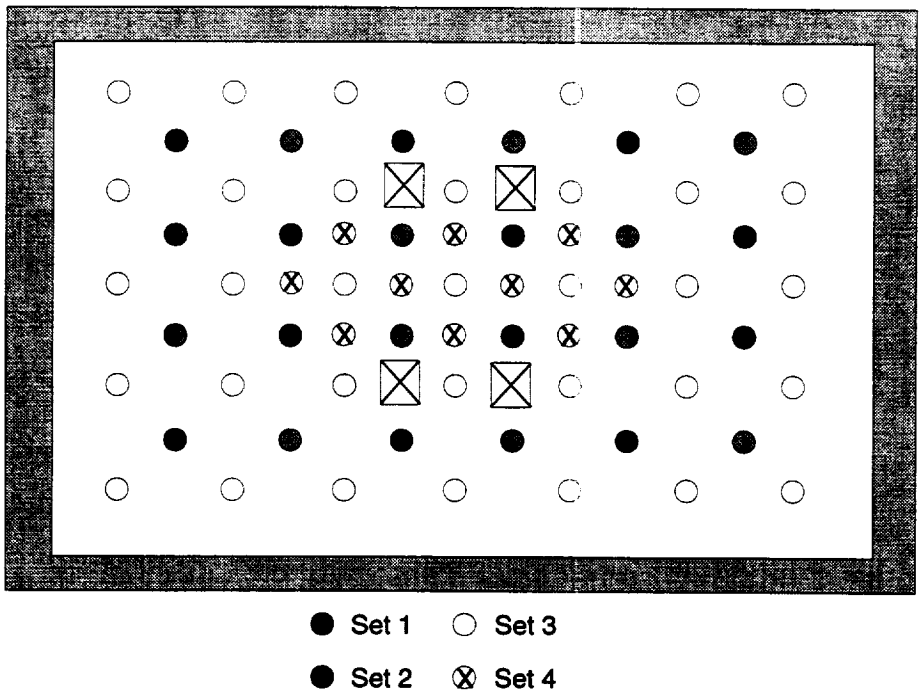

Figure 5.36 Location of Distributed Masses

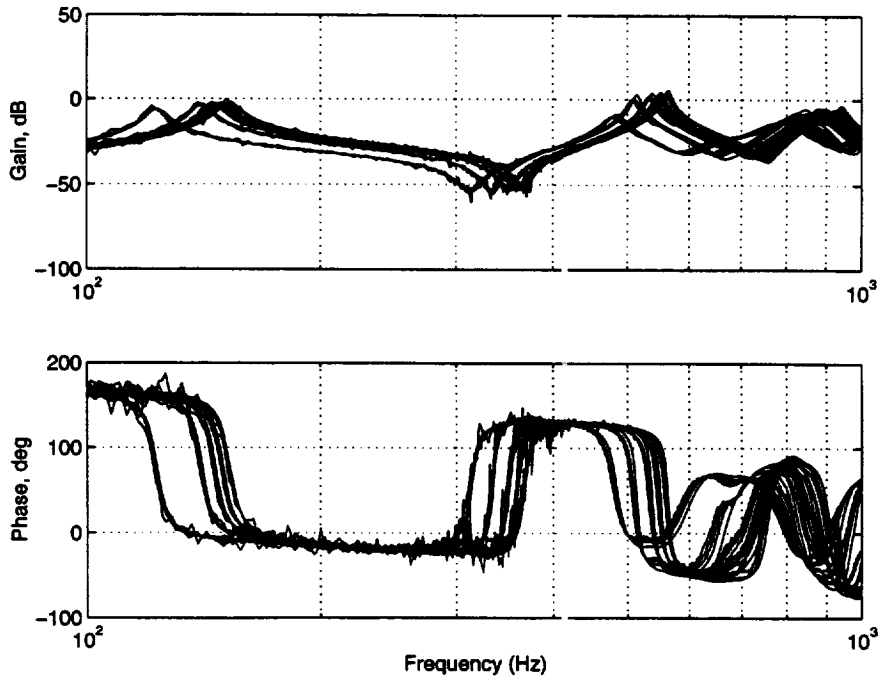

Figure 5.37 System Transfer Functions $G_{U_{11}}$ with Additional Mass

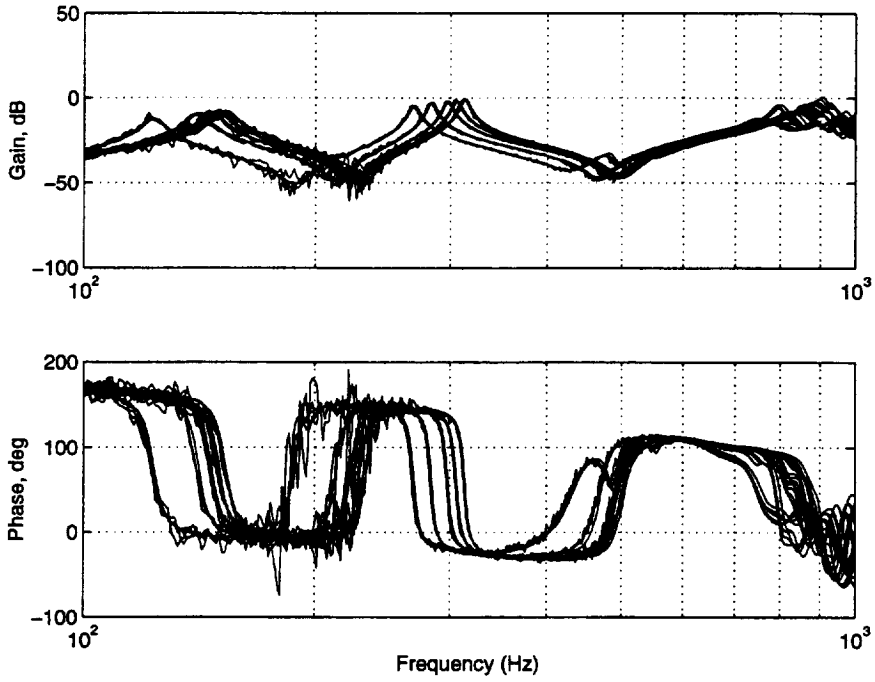

Figure 5.38 System Transfer Functions $G_{U_{22}}$ with Additional Mass

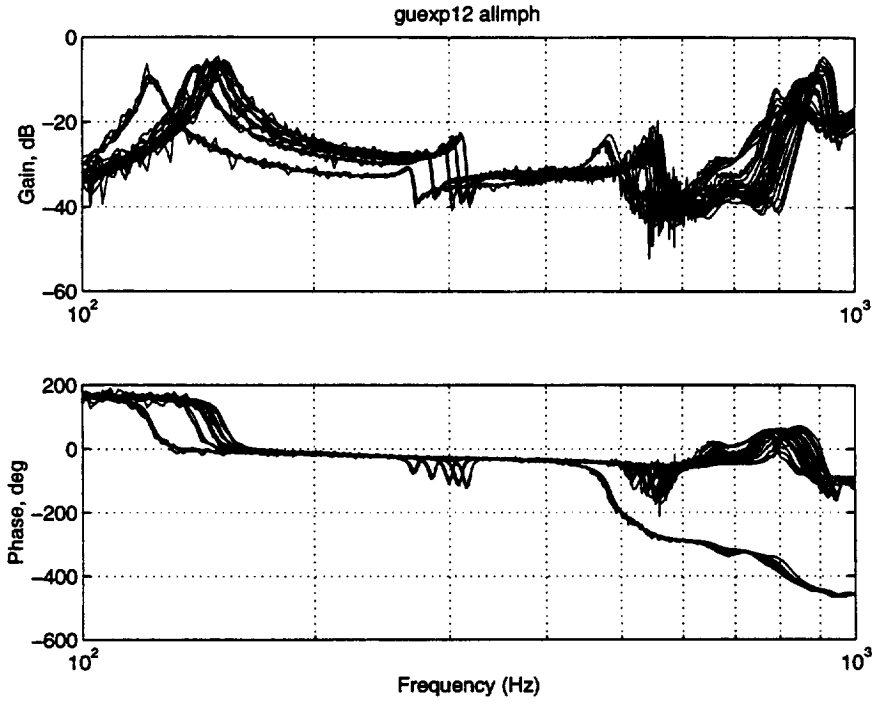

Figure 5.39 System Transfer Functions $G_{U_{12}}$ with Additional Mass

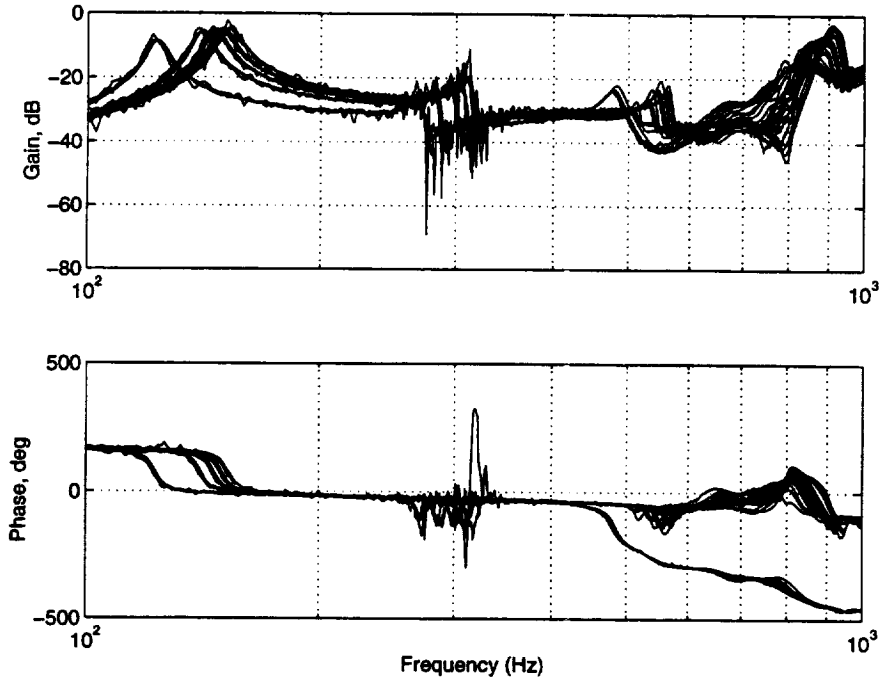

Figure 5.40 System Transfer Functions $G_{U_{21}}$ with Additional Mass

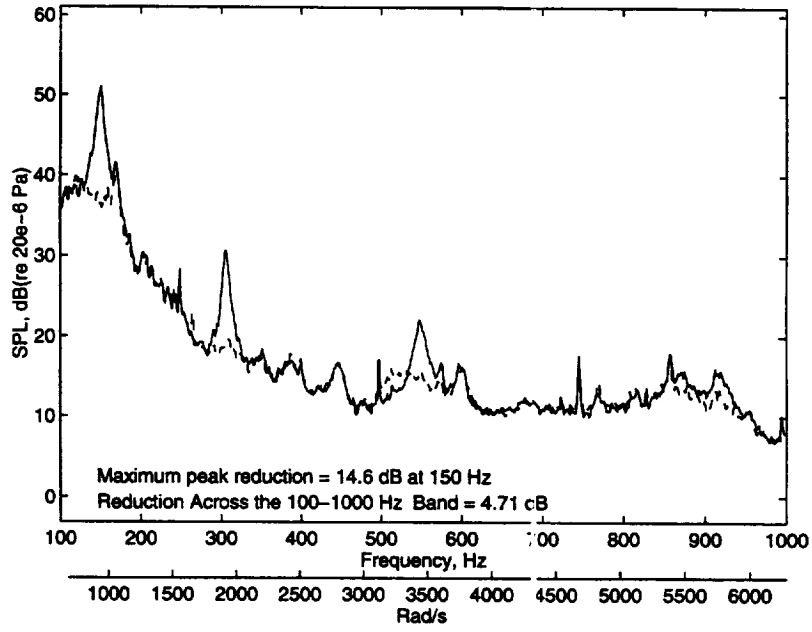

Figure 5.41 SPL at Mic 2 for Mass Set 1 (35.8 m/s);
Uncontrolled (—);Controlled SPL (- -)

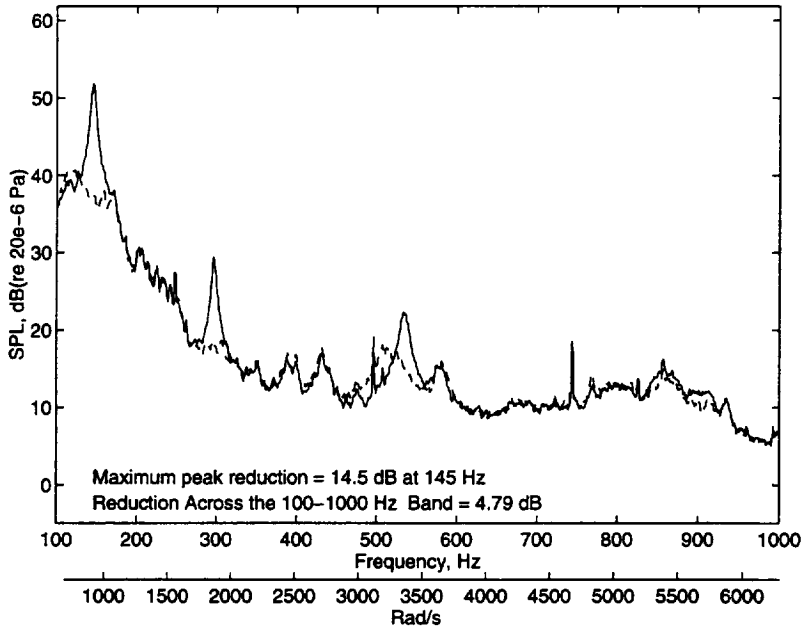

Figure 5.42 SPL at Mic 2 for Mass Set 2 (35.8 m/s);
Uncontrolled (—);Controlled SPL (- -)

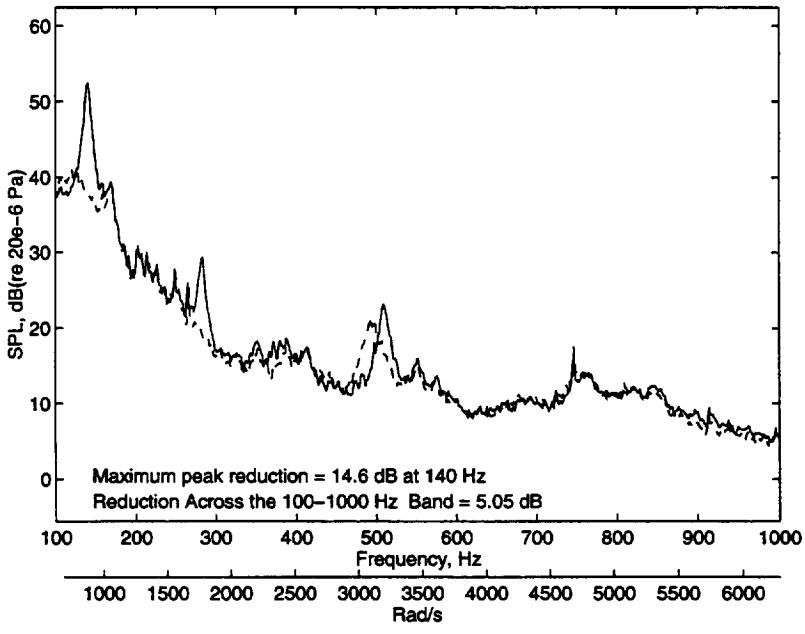

Figure 5.43 SPL at Mic 2 for Mass Set 3 (35.8 m/s);
Uncontrolled (—);Controlled SPL (- -)

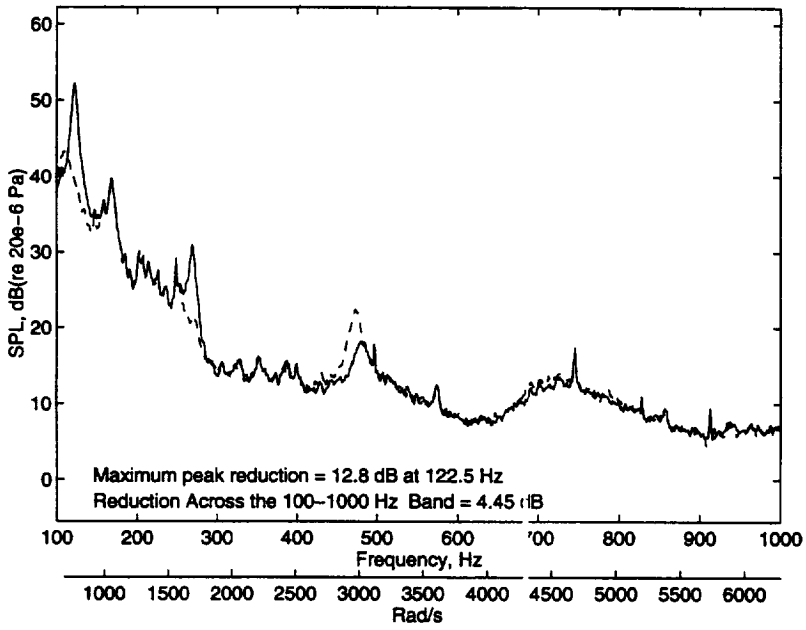

Figure 5.44 SPL at Mic 2 for Mass Set 4 (35.8 m/s);
Uncontrolled (—);Controlled SPL (- -)

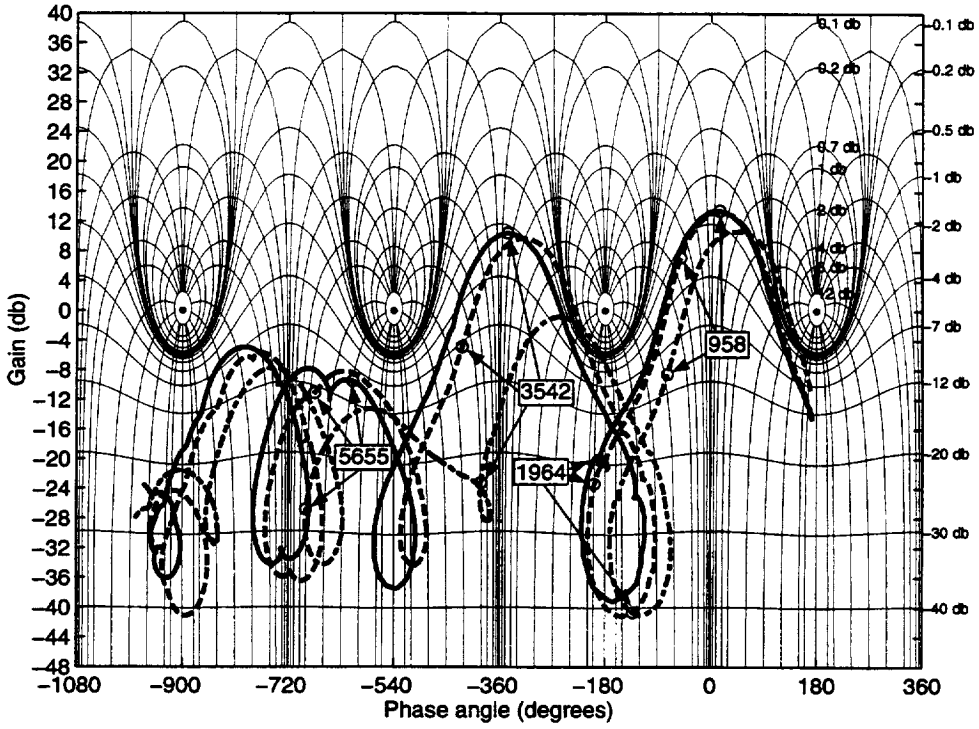

Figure 5.45 Nichols Chart for Loop 1 with Added Mass; Original System —; Mass Set 2 - -; Mass Set 4 – ·

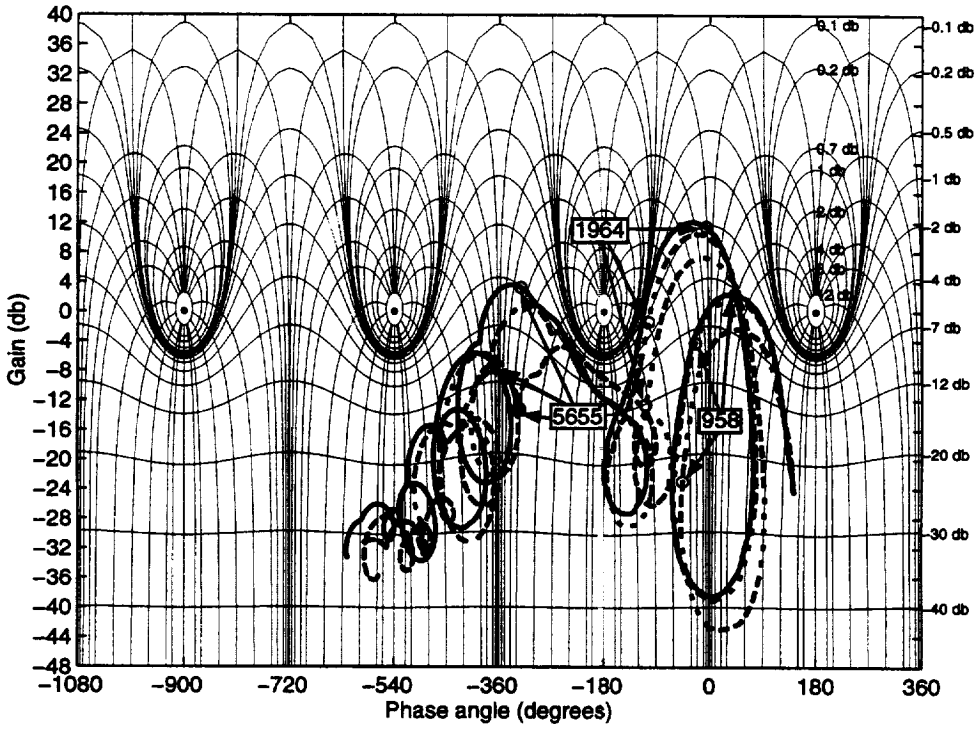

Figure 5.46 Nichols Chart for Loop 2 with Added Mass; Original System —; Mass Set 2 - -; Mass Set 4 – ·

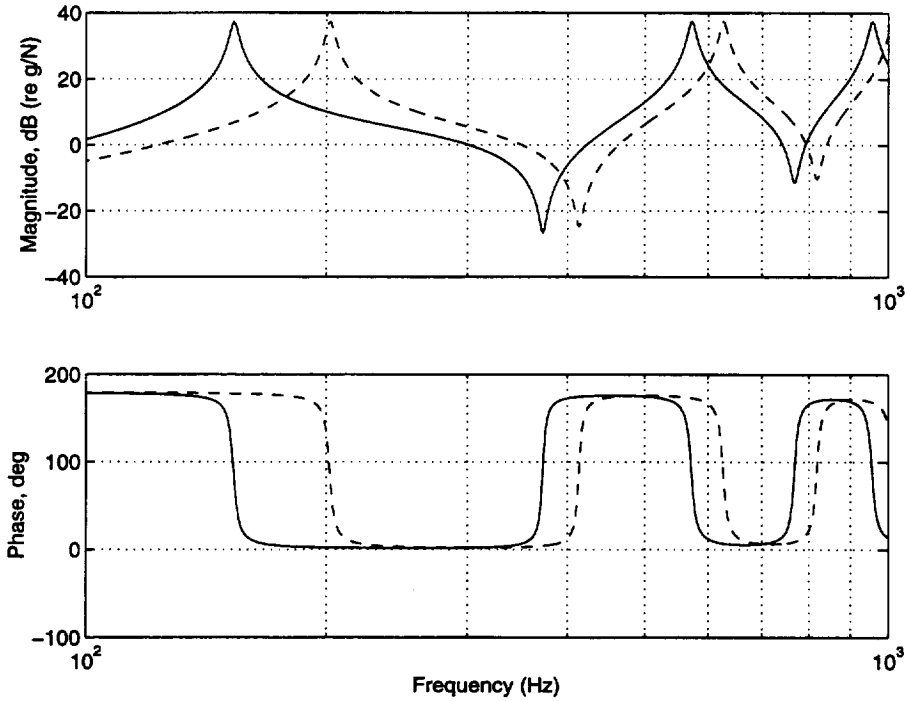

Figure 5.47 Bode Plot of System with Prestress; Original System —; System Prestress - -

CHAPTER 6. CONCLUSIONS AND RECOMMENDATIONS

This research was done to address the need for active control of flow induced structural radiation of sound. A successful control methodology for this problem is of primary interest to aircraft, automobile, and sonar design engineers. In this chapter the conclusions drawn from this project and the recommendations regarding the future direction of this work are presented.

6.1 Conclusions

Based upon the current state of the art in active control, it can be concluded that active control of flow induced structural radiation of sound has not been effectively addressed. Prior to this investigation, no experimental results involving active structural acoustic control for a turbulent flow excitation had been obtained. Furthermore, analytical investigations of this problem had considered only full state feedback control approaches. In this investigation an analytical model was developed and used to characterize the problem and evaluate various control methodologies. The controller design approach developed using this model was successfully applied in an experimental investigation. These results represent the first experimental implementation of an active structural acoustic controller for a turbulent flow excitation.

In this work, the limitations of existing control methodologies for the problem of flow induced structural sound radiation are identified. The lack of a viable reference transducer precludes the use of feedforward control. Optimal control is not practical for implementation as it is difficult or impossible to measure the state information required by the controller and the effects of delays, nonlinearities, unmodeled modes,

and other uncertainties associated with this problem cannot be included in the design technique. μ synthesis was shown to achieve robust performance only in the case of small parametric uncertainty and reduced sound pressure level reduction requirements. This was a direct consequence of the uncertainty required to account for errors in the system model and the parametric nature used to describe the system uncertainty. For adaptive feedback control, the closed loop stability was shown to rely on accurate plant models. Furthermore, in experimental investigations adaptive feedback control resulted in system instability for various flow conditions.

To overcome the limitations of existing control methodologies, a frequency domain feedback controller design method was developed for active structural acoustic control of lightly damped systems. The methodology was evaluated for the active control of the flow induced structural radiation of sound. This control methodology ensures stability, provides sound pressure level reductions, and avoids saturation of the control transducer. The controller design is based directly on measured system information such that additional uncertainty required by modeling errors is not necessary. The problem of the delay associated with sound pressure feedback was overcome with the use of acceleration feedback. By utilizing the uncontrolled sound pressure levels in the controller design process to appropriately weight the acceleration feedback, specified sound pressure level reductions were achieved at multiple microphone locations.

A unique characteristic of the controller is the use of the plant dynamics to achieve the desired control. This was accomplished by using controller lag, through non-minimum phase zeros, to appropriately phase the system resonances. It was shown that for the turbulent flow induced structural sound radiation problem this technique allows higher frequencies to be controlled with a low DC gain and controller order. Furthermore, the use of the natural dynamics of the system was shown to yield superior robustness to large changes in the plant transfer functions.

An experimental apparatus was designed and built to verify the control methodology for the problem of turbulent flow induced structural sound radiation. Using the robust frequency domain feedback controller approach, a MIMO controller was

designed and implemented. The desired sound pressure level reductions were achieved at multiple microphone locations over a wide range of flow speeds. The sound pressure level reductions were approximately 5.0 dB across the 100-1000 Hz band.

The successful development of a robust feedback control method for active structural acoustic control achieved the major goal of this research project. This control method represents a viable alternative to adaptive feedforward control for many problems. For the problem of flow induced structural sound radiation, this technique represents the approach which offers the most promise in solving practical problems.

6.2 Recommendations

For future work in this area it is recommended that the controller technique presented in this work be applied to an actual system. An investigation of the system uncertainty associated with the fuselage of an aircraft, for example, would determine the degree of robustness required in the controller. The influence of functions such as airspeed, pressure loading, and temperature should be evaluated. Additionally, the use of more easily integrated sensors and actuators, such as piezoelectric patches, should be evaluated.

The control method itself can be extended in a number of ways. Additional computational capabilities would allow the use of off-diagonal controllers. Off-diagonal control could reduce the control actuator requirements and improve system performance. Additionally, gain scheduled controllers should be evaluated. Gain scheduling allows the system uncertainty to be split between separate controllers such that greater control performance can be achieved while maintaining robust stability. Finally, the interaction of control between adjacent panels should be investigated. The controller design must account for this interaction in order to implement a full scale controller for this problem.

LIST OF REFERENCES

LIST OF REFERENCES

[1] M. J. Lighthill. On sound generated aerodynamically. *Proc. Roy. Soc.*, pages 564–587, 1952.

[2] J. E. Ffowcs Williams and D. L. Hawkings. Sound generation by turbulence and surfaces in arbitrary motion. *Philosophical Transactions of the Royal Society of London*, 264:321–342, 1969.

[3] S. K. Robinson. Coherent motions in the turbulent boundary layer. *Annu. Rev. Fluid Mech.*, 23:601–639, 1991.

[4] K. S. Breuer. Active control of wall pressure fluctuations in a turbulent boundary layer. *Flow Noise Modeling, Measurement, and Control, ASME Winter Annual Meeting*, pages 39–47, 1993.

[5] C. R. Smith. A synthesized model of the near-wall behavior in turbulent boundary layers. *Proc. Symp. Turbul., 8th,*, 1984.

[6] P. R. Bandyopadhyay and R. Balasubramanian. A vortex model for calculating wall pressure fluctuations in turbulent boundary layers. *Flow Noise Modeling, Measurement, and Control, ASME Winter Annual Meeting*, pages 13–24, 1993.

[7] W. W. Willmarth. Pressure fluctuations beneath turbulent boundary layers. *Annual Review of Fluid Mechanics*, pages 13–38, 1975.

[8] J. A. Astolfi and B. E. Forestier. Flow noise associated with near-wall turbulence structure. *Flow Noise Modeling, Measurement, and Control, ASME Winter Annual Meeting*, pages 1–11, 1993.

[9] G. Schewe. On the structure and resolution of wall-pressure fluctuations associated with turbulent boundary-layer flow. *J. Fluid Mech.*, 134:311–328, 1983.

[10] W. W. Willmarth and C. E. Wooldridge. Measurements of the fluctuating pressure at the wall beneath a thick turbulent boundary layer. *J. Fluid Mech.*, 1962.

[11] G. M. Corcos. Resolution of pressure in turbulence. *J. Acoust. Soc. Am.*, 35(2):192–199, 1963.

[12] W. A. Strawderman. Turbulence-induced plate vibrations: and evaluation of finite- and infinite-plate models. *J. Acoust. Soc. Am.*, 46(5):1294–1307, 1969.

[13] W. K. Blake. *Mechanics of Flow-Induced Sound and Vibration.* Academic Press, Inc., 1986.

[14] G. M. Corcos. The resolution of turbulent pressures at the wall of a boundary layer. *J. Sound Vib.*, 6(1):59–70, 1967.

[15] M. K. Bull. Properties of the fluctuating wall pressure field on a turbulent boundary layer. *AGARD Rept. 455*, 1963.

[16] J. T. Priestly. Correlation studies of pressure fluctuations on the ground beneath a turbulent boundary layer. *NBS Rep. 8942*, 1965.

[17] W. A. Strawderman and Brand R. S. Turbulent-flow-excited vibration of a simply supported, rectangular flat plate. *J. Acoust. Soc. Am.*, 45(1):177–192, 1968.

[18] W. V. Bhat. Flight test measurement of exterior turbulent boundary layer pressure fluctuations on Boeing model 737 airplane. *J. Sound Vib.*, 14(4):439–457, 1971.

[19] E. J. Skudrzyk and G. P. Haddle. Noise production in a turbulent boundary layer by smooth and rough surfaces. *J. Acoust. Soc. Am.*, 32:19–34, 1960.

[20] L. Maestrello. Radiation from and panel response to a supersonic turbulent boundary. *J. Sound Vib.*, 10(2):261–295, 1969.

[21] B. M. Efimtsov. Characteristics of the field of turbulent wall pressure fluctuations at large Reynolds numbers. *Sov. Phys. Acoust.*, 28(4):289–292, 1982.

[22] Y. Y. Tang, R. J. Silcox, and J. H. Robinson. Sound transmission through cylindrical shell structures excited by boundary layer pressure fluctuations. *2nd AIAA/CEAS Aeroacoustics Conference*, 1996. AIAA 96-1760.

[23] M. S. Kompella and R. J. Bernhard. Variation of structural-acoustic characteristics of automotive vehicles. *Noise Control Engineering Journal (To Appear).*

[24] A. C. Eringen. Response of beams and plates to random loads. *Journal of Applied Mechanics*, pages 46–52, 1957.

[25] I. Dyer. Response of plates to a decaying and convecting random pressure field. *J. Acoust. Soc. Am.*, 31(7):922–929, 1959.

[26] P. H. White. Transduction of boundary-layer noise by a rectangular panel. *J. Acoust. Soc. Am.*, 40(6):1354–1362, 1966.

[27] L. Maestrello. Use of turbulent model to calculate the vibration and radiation responses of a panel, with practical suggestions for reducing sound level. *J. Sound Vib.*, 5(3):407–448, 1967.

[28] C. Guigou and C. R. Fuller. Active control of sound radiation from a semi-infinite elastic beam with a clamped edge. *J. Sound Vib.*, 168(3):507–523, 1993.

[29] C. Guigou, C. R. Fuller, and K. D. Frampton. Experiments on active control of acoustic radiation due to a clamped edge on a semi-infinite beam. *J. Sound Vib.*, 169(4):503–526, 1994.

[30] R. L. Clark and C. R. Fuller. Control of sound radiation with adaptive structures. *J. of Intell. Mater. Syst. and Struct.*, 2(1):431–452, 1991.

[31] S. Akishita and Y. Mitani. Sound transmission control through rectangular plate by using piezoelectric ceramics as actuators and sensors. *J. of Intelligent Material Systems and Structures*, 5:371–378, 1994.

[32] S. Y. Hong, V. V. Varadan, and V. K. Varadan. Active control of sound radiation from vibrating structures. *Adaptive Structures and Material Systems*, pages 355–361, 1993. The 1993 ASME Winter Annual Meeting, AD-Vol. 35.

[33] E. T. Falangas, J. A. Dworak, and S. Koshigoe. Controlling plate vibrations using piezoelectric actuators. *IEEE Control Systems*, 14(4):34–41, 1994.

[34] J. C. Doyle. Guaranteed margins for LQG regulators. *IEEE Transactions on Automatic Control*, 23(4):756–757, 1978.

[35] L. Meirovitch and S. Thangjitham. Control of sound radiated from an orthotropic plate. *Active Noise and Vibration Control 1990*, pages 23–30, 1990. The Winter Annual Meeting of the ASME, NCA-Vol. 8.

[36] L. Meirovitch and S. Thangjitham. Active control of sound radiation pressure. *J. Vib. Acoust.*, 112:237–244, 1990. The Winter Annual Meeting of the ASME, NCA-Vol. 8.

[37] W. T. Baumann, W. R. Saunders, and H. H. Robertshaw. Active suppression of acoustic radiation from impulsively excited structures. *J. Acoust. Soc. Am*, 90(6):3202–3208, 1991.

[38] S. J. Elliott and M. E. Johnson. Radiation modes and the active control of sound power. *J. Acoust. Soc. Am.*, 4:94, 1993.

[39] W. T. Baumann, F. Ho, and H. H. Robertshaw. Active structural acoustic control of broadband disturbances. *J. Acoust. Soc. Am*, 92(4):1998–2005, 1992.

[40] B. E. Parker and H. V. Poor. Adaptive nonlinear polynomial neural networks for control of boundary layer /structural interaction. *Active Control of Noise and Vibration*, pages 33–46, 1992. The Winter Annual Meeting of the ASME, DSC-Vol. 38.

[41] Jr. B. E. Parker, R. L. Cellucci, D. W. Abbott, R. L. Barron, and P. R. Jordan III. Adaptive nonlinear polynomial neural networks for control of boundary layer /structural interaction. Technical report, NASA Contractor Report 189645, 1993.

[42] L. Maestrello. Design criterion of panel structure excited by turbulent boundary layer. *Journal of Aircraft*, 5(4):321–328, 1968.

[43] D. K. Peterson, G. Toth, B. N. Tran, G. P. Mathur, and M. A. Simpson. Active structural acoustic control of broadband sound transmission through a panel. Aiaa-96-1725, 1996.

[44] D. R. Thomas and P. A. Nelson. Feedback control of sound transmission through stiff lightweight partitions. *Proc. Inter-Noise 94*, pages 1283–1286, 1994.

[45] D. R. Thomas and P. A. Nelson. The application of an implicit self tuning lqg algorithm to the active control of sound transmission. *Proc.eedings of Active 95*, pages 299–310, 1995.

[46] D. R. Thomas and P. A. Nelson. Discrete time feedback control of sound radiation. *AIAA Paper No. AIAA96-1785*, 1996.

[47] D. R. Thomas and P. A. Nelson. Active control of turbulent boundary layer induced sound radiation. *Proc. Inter-Noise 93*, pages 803–806, 1993.

[48] D. R. Thomas and P. A. Nelson. Active control of turbulent boundary layer noise in aircraft. Aiaa-93-4423, 1993.

[49] D. R. Thomas and P. A. Nelson. On the use of feedback to control sound radiation from a plate excited by a turbulent boundary layer. Technical report, University of Southampton Institute of Sound and Vibration Research, 1994.

[50] D. R. Thomas and P. A. Nelson. On the use of feedback control of sound radiation from a plate excited by a turbulent boundary layer. *J. Acoust. Soc. Am.*, 98(5):2651–2662, 1995.

[51] H. T. Banks, M. A. Demetriou, and R. C. Smith. An h_∞ minmax periodic control in a two-dimensional structural acoustic model with piezoceramic actuators. *IEEE Transactions on Automatic Control*, 41(7):943–959, 1996.

[52] H. T. Banks, R. J. Silcox, and R. C. Smith. The modeling and control of acoustic/structure interaction problems via piezoceramic actuators: 2-d numerical examples. *ASME J. Vibration Acoust.*, 116:386–396, 1994.

[53] R. S. Smith. An experimental evaluation of uncertainty models for a flexible strucutre control problem. *Proceedings of the 30th IEEE Conference on Decision and Control*, pages 1658–1659, 1991.

[54] G. J. Balas and J. C. Doyle. Control of lightly damped, flexible modes in the controller crossover region. *Journal of Guidance, Control, and Dynamics*, 17(2):370–377, 1994.

[55] X. H. Yang, J. van Niekerk, K. S. Parwani, K. Hendrick, A. Packard, and B. Tongue. Acoustical response tailoring in reverberant enclosures using feedback control. *Active Control of Noise and Vibration, ASME, DSC-Vol. 38*, pages 7–14, 1992.

[56] X. H. Yang, J. van Niekerk, K. S. Parwani, A. Packard, and B. Tongue. Attenuation of structurally generated interior noise through active control. *Proceedings of the 1993 American Control Conference*, pages 1–7, 1993.

[57] Y. Chait, C. V. hollot, P. Mehta, and Y. Zheng. Active noise control in ducts using non-adaptive feedforward/feedback control. *Noise-Con 96*, pages 379–384, 1996.

[58] P. Mehta, Y. Zheng, C. V. Hollot, and Y. Chait. Active noise control in ducts: Feedforward/feedback design by blending h_∞ and qft methods. *IFAC'96 13th Triennial World Congress*, pages 291–296, 1996. San Francisco.

[59] O. Fluder and R. Kashani. Robust control of structure-borne noise using h_∞ methods. *ASME Active Control of Noise and Vibration*, pages 191–204, 1992.

[60] F. M White. *Fluid Mechanics.* McGraw-Hill Book Co., 1986.

[61] E. J. Richards and D. J. Mead, editors. *Noise and Acoustic Fatigue in Aeronautics.* John Wile & Sons Ltd, 1968.

[62] T. W. Parks and C. S. Burrus. *Digital Filter Design.* John Wiley & Sons, Inc., 1987.

[63] Y. Champoux, S. Brunet, and A. Berry. On the construction of a simply supported rectangular plate for noise and vibration studies. *Experimenal Techniques*, 20(1):24–26, 1996.

[64] Daniel Brown. The design, construction, and validation of a small, low-speed, quiet wind tunnel with application to noise from the flow over a cavity. Master's thesis, Purdue University, 1995.

[65] F. Han. Measurement of wall pressure fluctuations under a turbulent boundary layer. Aeroacoustics Project Report, 1996.

[66] F. Fahy. *Sound and Structural Vibration Radiation, Transmission and Response.* Academic Press Limited, 1985.

[67] M. Steinbunch, J. C. Terlouw, and O. H. Bosgra. Robustness analysis for real and complex perturbations applied to an electro-mechanical system. *Proceedings of the 1991 American Control Conference*, pages 556–561, 1991.

[68] J. C. Doyle. Structured uncertainty in control system design. *Proceedings of the 24th IEEE Conference on Decision & Control*, pages 260–265, 1985.

[69] A. Packard, J. Doyle, and G. Balas. Linear, multivariable robust control with a μ perspective. *Journal of Dynamic Systems, Measurement, and Control*, 115(2):426–438, 1993.

[70] M. G. Safonov. Stability margins of diagonally perturbed multivariable feedback systems. *IEE Proc. Pt. D*, 129(6):251–256, 1982.

[71] L. Eriksson. Development of the filtered-u algorithm for active noise control. *J. Acoust. Soc. Am*, 89(1):257–265, 1991.

[72] Christine Scheper. An investigation of the behavior of adaptive recursive algorithms applied to the control of modal systems Master's thesis, Purdue University, 1991.

[73] M. Franchek and S. Jayasuriya. Controller design for performance guarantees in uncertain regulating systems. *Int. J. Control*, 61(1):127–148, 1995.

[74] D. K. Cheng. *Analysis of Linear Systems.* Addison-Wesley Pub. Co., 1959.

[75] M. Franchek. Selecting the performance weights for the μ and h_∞ synthesis methods for siso regulating. *ASME Journal of Dynamic Systems, Measurement, and Control*, 118:126–131, 1996.

[76] A. Leissa. *Vibration of Plates.* Acoustical Society of America, 1993.